LIQUID METAL-BASED TERAHERTZ METAMATERIALS

by

Jinqi Wang

A dissertation submitted to the faculty of
The University of Utah
in partial fulfillment of the requirements for the degree of

Doctor of Philosophy

Department of Electrical and Computing Engineering

The University of Utah

August 2015

The University of Utah Graduate School

STATEMENT OF DISSERTATION APPROVAL

The dissertation of **Jinqi Wang**

has been approved by the following supervisory committee members:

Ajay Nahata	, Chair	**05/12/2015** Date Approved
Steven Blair	, Member	**05/12/2015** Date Approved
Hanseup Kim	, Member	**05/12/2015** Date Approved
Michael Bartl	, Member	**05/12/2015** Date Approved
Sivaraman Guruswamy	, Member	**05/12/2015** Date Approved

and by **Gianluca Lazzi** , Chair/Dean of

the Department/College/School of **Electrical and Computer Engineering**

and by David B. Kieda, Dean of The Graduate School.

ABSTRACT

Metamaterials have gained significant attention over the last decade because they can exhibit electromagnetic properties that are not readily available in naturally occurring materials. This dissertation describes our work on design, fabrication and characterization of liquid metal-based metamaterials with focus on their applications in the terahertz (THz) frequency range. In contrast to the more conventional approaches to fabricating these structures, which rely on vacuum deposited solid metal films, we used metals that are liquid at room temperature. This family of materials is especially attractive for such applications, since it enables large-scale reconfigurability in the overall geometry of the device. We demonstrate a number of unique plasmonic and metamaterial devices. Within the topic of plasmonics, we demonstrate a device that allows for mechanical stretching that is reversibly deformable. In an analogous structure, we can change the geometry dramatically by injecting or withdrawing liquid metals from specific area of the pattern. We also developed a liquid metal-based reconfigurable THz metamaterial device that is not only pressure driven, but also exhibits pressure memory. As an alternate approach to demonstrate reconfigurability, we developed a technique for creating dramatic configuration changes in a device via selective erasure and refilling of metamaterial unit cells that utilizes hydrochloric acid. While the approach is successful in changing the geometry, it does not allow for fine spatial control of the pattern. Thus, we have refined the approach by developing an electrolytic process to change the geometry of a liquid

metal-based structured device in a more localized and controlled manner. Since liquid metals can be solidified under certain conditions, we have demonstrated a novel technique for fabrication of free-standing two-dimensional and three-dimensional terahertz metamaterial devices using injection molding of gallium. Finally, we developed a technique of printing three-dimensional solid metal structures by pulling liquid gallium out of a reservoir via solid/liquid interface. Based on these results, we are currently extending our work towards development of metamaterials that can be used in real-world applications. Based on the significant progress made the THz field over the last two decades, the likelihood of THz systems level applications is much brighter.

TABLE OF CONTENTS

ACKNOWLEDGEMENTS

During the time of writing this dissertation, I realized that this is not only a summary of my PhD study, but also a perfect end to my student life. I would like to take this opportunity to gratefully acknowledge the contribution of everyone who has helped me in the past. I could not have obtained these successful accomplishments without any of them.

First, I would like to express my sincere gratitude and appreciation to my advisor, Dr. Ajay Nahata, for his selfless guidance. I have learned a lot from him since the first day I talked with him in the office. His availability for discussing interesting work made me be able to do my research very productively and successfully. One of his distinctive characteristics, also the one I like the most, is that he not only cares about students now or in the PhD study, but also helps us prepare well for future careers. I've been really glad to work with him for the last several years. Study at the University of Utah is an invaluable and memorable thing for me.

Second, I want to thank my colleagues for working with me, especially Ms. Shuchang Liu, Mr. Xiaojin Jiao, Mr. Andrew Paulsen, Mr. Kanagasundar Appusamy, and Prof. Sivaraman Guruswamy. Each of them taught me their strength and made collaboration enjoyable. I thank my supervisory committee members, Prof. Steve Blair, Prof. Hanseup Kim, Prof. Michael Bartl, and Prof. Sivaraman Guruswamy, for taking time to discuss and advise my work.

I would also like to thank my parents for their continuous advice and support of my study since elementary school. I would not have today's achievement without their love. They set an excellent example for me in career and home life. Their experiences taught me many things and made me know what I should do in my youth. They are the people I'm most proud of.

Lastly and most importantly, I want to thank my beloved wife, Lingyun Hu. I'm grateful to her support of my life and career. She always has a magic power to make me overcome any difficulty. Because of her, my life becomes more interesting, colorful and meaningful.

CHAPTER 1

INTRODUCTION

1.1 Terahertz Technology

Terahertz (THz) radiation, which lies in the frequency between microwaves and infrared from 0.1 THz to 10 THz, has been studied extensively since well over two decades ago. The THz frequency range is commonly referred to as the THz "gap" and research in this frequency range has been delayed for a long time because of limited availability of THz sources and detectors. As various sources, detectors and devices are being studied, the gap has begun to close.

There are a variety of techniques for generating THz radiation that have arisen from the development of ultrafast lasers, manufacturing of semi-insulating semiconductors and micromachining techniques [1]. The two most widely used techniques for generating broadband THz radiation are photoconductive switches and optical rectification, with both relying on femtosecond lasers [2]. Photoconductive switches were the first technique used to generate sub-single-cycle THz pulses with pulse energies at μJ-level [3]. Optical rectification is a second-order nonlinear process, which produces THz radiation via difference-frequency mixing between the spectral components of a femtosecond pump pulse [4,5]. Nonlinear processes in gas plasmas using high-intensity femtosecond pulses have been used also to generate single-cycle THz pulses with high field strengths [6,7].

While significant attention has been devoted to the application of broadband THz radiation, narrowband and single frequency THz radiation has also been shown to be important for high-resolution spectroscopy, sensors and communications. It should also be noted that narrowband THz generation is possible by using a photomixer [8], optical parametric conversion [9], quantum cascade laser [10] or diodes [11].

THz radiation has a low photon energy in the range of 1–10 meV. Using conventional room temperature detectors, the measured signal is dominated typically by ambient thermal background noise. Thus, such detectors typically have to be cooled to liquid nitrogen or liquid helium temperatures. Heterodyne semiconductor and superconductor detectors are commonly used to obtain high-resolution spectroscopy [12]. Schottky diodes [13], bolometers [14], superconducting tunnel junctions [15] and single-photon detectors [16] are also able to detect THz signal. In addition to these approaches, THz time-domain spectroscopy is a coherent detection system used for ultrashort THz detection and widely used in today's broadband terahertz detection. Signal-to-noise ratios greater than 10000:1 are possible because of the high performance of THz optics and optoelectronic gating [17].

THz technology has increasingly attracted interest because it can provide a number of unique properties in different areas, including information technology, biology, homeland security and agricultural products [1,12,18,19]. Because many spectral signatures lie in the millimeter and submillimeter spectral ranges, studies in the THz frequency range were first widely used by astronomers to study interstellar dust through spectra of molecular line emissions [20]. The THz spectrum also contains spectroscopic signatures for many physical phenomena, such as molecular rotational transitions; it is suitable to

directly identify dangerous materials rather than further inspecting after guessing their existence [21]. Therefore, THz imaging can be used in nondestructive evaluation and quality control [22]. With regard to communications applications, THz technology is a promising method for secure communications due to high directionality, low scattering, large channel bandwidth and hidden THz signals in the background noise [23]. Also, terahertz communication is important for increasing the capacity of wireless communication and is expected to become a reality soon according to the data rate increasing speed [24]. THz radiation can also be used for other applications such as manufacturing control, security, and biological and medical science [18].

There are several THz companies world-wide that can provide THz generators, detectors and imaging cameras. The THz market is expected to increase dramatically over the next ten years, based on market research, if more THz devices become available. THz devices have several requirements. First, they must be sensitive to THz radiation. Second, it will be advantageous if the devices could actively manipulate THz waves. Third, they should ideally adapt to system needs and therefore be reconfigurable. In general, there are several ways to manipulate and control THz radiation. Metamaterial and plasmonics are promising means for achieving this.

1.2 Metamaterials and Plasmonics

Metamaterials are artificially structured materials and have gained significant attention over the last decade. They have been used in a variety of applications that hold great promise for next-generation devices. The unique properties of metamaterials are achieved from the shape, geometry and size of the structure, not just from the

composition of the underlying material. By designing appropriate dimensions for these metal structures, we can engineer metamaterials to obtain the desired response. Metamaterial unit cells are usually arranged in an array to exhibit strong resonance.

The application of metamaterials was initially implemented at microwave frequencies due to well-established fabrication methods by assembling patterned circuit boards [25]. Extensive theoretical and experimental efforts have been used to study exotic functions, such as negative refractive index [25,26], memory [27], antenna [28] and cloaking [29–31]. Work on the topic of metamaterials has been extended to higher frequency ranges. In the optical frequency range, a variety of advanced techniques, including electron-beam lithography, focused ion beam lithography and membrane projection lithography, have been utilized to fabricate complex metamaterials at nm scales [32–38]. Due to the fact that the metamaterial response scales with frequency, the development of new device functionalities can benefit from a variety of well-developed microfabrication techniques. This creates the opportunity to study unique properties of THz metamaterials with greater functionality. Based on the metamaterial concept, a number of devices working at THz frequencies, including frequency-agile filters [39], absorbers [40], ultrahigh refractive index [41], negative refractive index [42], quarter-wave plate [43] and phase modulators [44], have been demonstrated recently. Among these, actively tuning the resonant response of THz metamaterials is of particular interest since dynamic tuning provides more flexible ways to manipulate electromagnetic radiation. Typical metamaterial devices are metallic elements fabricated on dielectric substrates. Because solid metal is used, the device does not allow for large-scale changes of the geometry after fabrication. This limits available functions of the device. Device performance can be improved if we

adopt flexible or reconfigurable metallic or dielectric materials.

In addition to metamaterials, plasmonics offers another means for controlling and manipulating electromagnetic radiation [45,46]. A surface plasmon polariton (SPP) is an oscillating surface charge density coupled to an electromagnetic field along a metal-dielectric interface. The dispersion property of SPPs is dramatically different from that of free-space radiation. We need to couple free-space radiation to SPPs by structuring the surface of metals or using a prism. After excitation, SPPs can propagate along metal-dielectric interfaces. This creates opportunities for new applications, including extraordinary transmission [47], plasmonic waveguides that can guide electromagnetic waves beyond the diffraction limit [48] and plasmonic circuits that merge electronics and photonics together [49]. Localized SPPs also provides unique capabilities for confining an electromagnetic field enabling high field enhancement [50]. Such approaches have been widely used for biosensors [51,52], surface enhanced Raman spectroscopy [53,54] and plasmonic photovoltaics that can improve absorption to reduce the material thickness [55,56]. Nobel metals and alloys are often used for plasmonics in the optical frequency range [57–59]. In THz spectral range, in addition to silver and gold, both conventional metals and conductive nonmetals such as semiconductors can support the propagation of SPPs since the conductivities are sufficiently high and exhibit corresponding low propagation losses [60,61]. The conductivity change in semiconductors can be used to create active THz devices. However, such changes typically alter the magnitude of resonance. In many cases, it is highly desirable to actively control and manipulate the device response to a large extent by changing the geometrical structure of the device.

1.3 Gallium-Based Liquid Metals

Liquid metals have attracted a lot of interest due to their unique properties, including high conductivity and liquid behavior. One common liquid metal is mercury. However, because of toxicity, mercury is highly restricted in use. In contrast, gallium and gallium-based alloys are nontoxic and can serve as alternative materials for mercury in some applications. Gallium has a relatively low melting temperature of 29.77 °C, high boiling temperature of 2205 °C and high conductivity of 7.7×10^6 S/m [62]. Thus, mild heating can melt it. Although gallium has a melting point of 29.8 °C, it exhibits a strong supercooling effect, which means it can remain liquid after melting and recooling to well below its melting temperature. By mixing other components with gallium to form eutectic alloys, it is possible to reduce the melting temperature further, allowing for metals that are liquid at room temperature. There are two common liquid gallium alloys: eutectic gallium indium (EGaIn) and gallium indium tin (Galinstan). EGaIn has a melting temperature of ~15.5 °C. While gallium indium tin has a melting point of -19 °C [62]. Liquid metals with different melting temperatures can be used for different purposes. For example, the phase transition of gallium near 30 °C can be used for manipulating surface plasmon polaritons that have different properties in solid and liquid phase [63].

Liquid metals have many potential applications in various areas. It can be used as electrodes for soft-matter diodes [64], electrical contacts in solar cells [65] or inherently aligned microfluidic electrodes [66]. Since it can flow, liquid metals can be applied to coat micropatterned structures along the direction of an applied current driven by liquid electromigration [67,68]. Because liquids can change their configuration in response to external stimuli, liquid metals can be used for sensing. Pressing liquid metals will change

their cross-section and correspondingly, their electrical resistance, and can be used to change the length of liquid metal lines or the interference of light. Therefore, they can be used for pressure sensors by measuring electrical resistance [69,70], wireless signals [71] or the reflected color of light [72]. In combination with elastomeric substrates, they can be used for stretchable and flexible devices including antennas [73–75], fibers [76] and self-healing circuits [77].

When gallium is exposed to oxygen with pressures as low as 10^{-7} Torr, it is easy to form an oxide layer [78]. The oxide layer that forms at the surface of liquid metals allows the mechanical behavior of the gallium-based alloy to be different from that of pure liquid metals, and also provides other unique properties of these materials [79]. It provides a large yield stress, increases the surface and improves wetting [80]. The wetting behavior of gallium-based alloy droplets with thin metal foils can be tuned by the surface roughness of metal foil [81], or reduction with acid vapor [82]. By controlling the oxygen level and flow channel dimensions, liquid metals can form microdroplets with different shapes and sizes [83,84]. By using molecular self-assembly monolayer-forming thiols and sonication, liquid-phase EGaIn alloy can form nanoparticles smaller than 100 nm, which has strong surface plasmon resonances in the ultraviolet spectral range [85]. Despite the high surface tension, gallium-based liquid metals can maintain their shape due to mechanical support from the oxide surface. It forms a conical structure when a drop of liquid metal is separated from the dispensing needle [86]. Within a microchannel, liquid metals flow only when a critical pressure is exceeded and the surface oxide layer is ruptured [87]. This can be used for pressure-responsive frequency shifting antennas [88] and reconfigurable circuits [89]. Due to mechanical support force from the surface oxide

skin, liquid metals can be used for 3D structures either by combining 3D printing of hollow channels [90] or by direct printing [91].

1.4 Outlines

In the following chapters, we integrate the above important topics to study liquid metal-based terahertz plasmonics and metamaterials. Specifically, we design, fabricate and characterize liquid metal-based metamaterial devices to realize various THz components. By controlling the structure of the metallic element itself, we can obtain various electromagnetic responses of metamaterial devices. Experimental efforts will include fabrication of EGaIn- or Ga-based metamaterial devices, manipulation of their devices geometries and characterization of the transmission properties of these devices.

In Chapter 2, we discuss the generic fabrication process and measurement techniques for most of devices used in the following chapters. We fabricate most of devices via standard soft lithography techniques using polydimethylsiloxane (PDMS), a transparent polymer. By designing different replica masters, we can obtain a variety of different PDMS molds and resulting liquid metal-based devices. To measure the terahertz transmission properties, we use terahertz time-domain spectrometer to measure the spectra. By transforming the time-domain data to the frequency domain, we are able to determine independently both the magnitude and phase of the transmission coefficient.

In Chapter 3, we first demonstrate experimentally that liquid metals support SPPs at THz frequencies. Specifically, we inject EGaIn into a PDMS mold fabricated using soft lithography techniques. We observe enhanced THz transmission through a periodic array of subwavelength apertures. While the DC conductivity of EGaIn is smaller than many

conventional metals, we clearly observe well-defined transmission resonances. Then we exploit the tuning capability by mechanically stretching PDMS elastomer. This represents a first step in developing reconfigurable and tunable plasmonic metamaterial devices that build upon well-developed microfluidic capabilities.

In Chapter 4, we experimentally demonstrate a reconfigurable plasmonic concept in which the geometry of a device can be changed dramatically. The specific demonstration we present utilizes EGaIn injected into or withdrawn from channels encapsulated by a PDMS mold fabricated on a Au-coated substrate. Using THz time-domain spectroscopy, we observe enhanced transmission properties through a single subwavelength aperture surrounded by different numbers of annular EGaIn rings. We then explain the results obtained from different device geometries using a simple time-domain model.

In Chapter 5, we demonstrate a technique for selectively erasing and refilling unit cells of THz metamaterials. The structures are formed by injecting EGaIn into microchannels within a PDMS mold fabricated using conventional soft lithography techniques. The thin oxide layer that forms on the surface of EGaIn can be locally dissolved via exposure to hydrochloric acid (HCl) introduced at the surface of the gas permeable PDMS mold. In the absence of the oxide skin, the liquid metal retracts to a position where a stable new oxide layer can be formed, effectively erasing the liquid metal structure in the presence of HCl. After erasing selected structures, EGaIn can be re-injected into microchannels to yield the initial structures. In the case of small unit cells, we show that mechanical pressure can be used to effectively erase individual elements. We use THz time-domain spectroscopy to characterize the distinct transmission properties for each of these different structures.

In Chapter 6, we demonstrate the ability to create artificially structured devices using liquid metals, in which the configuration can be altered via the electrolysis of saline solutions or deionized water. We accomplish this using an elastomeric mold with two different sets of embedded microfluidic channels that are patterned and injected with EGaIn and water, respectively. The electrochemical reaction is then used to etch the thin oxide layer that forms on EGaIn in a controlled reproducible manner. Once the oxide layer is dissolved locally, the underlying liquid metal retracts away from the original position to a position where a new stable oxide layer can reform, which is equivalent to erasing a section of the liquid metal. To allow for full reconfigurability, the entire device can be reset by refilling all of the microchannels with EGaIn.

In Chapter 7, we demonstrate a liquid metal-based reconfigurable THz metamaterial device that is not only pressure driven, but also exhibits pressure memory. The discrete THz response is obtained by injecting EGaIn into a microfluidic structure that is fabricated in PDMS using conventional soft lithography techniques. The shape of the injected EGaIn is mechanically stabilized by the formation of a thin oxide surface layer that allows the fluid to maintain its configuration within the microchannels despite its high intrinsic surface energy. Although the viscosity of EGaIn is twice that of water, the formation of the surface oxide layer prevents flow into a microchannel unless a critical pressure is exceeded. Using a structure in which the lateral channel dimensions vary, we progressively increase the applied pressure beyond the relevant critical pressure for each section of the device, enabling switching from one geometry to another. As the geometry changes, the transmission spectrum of the device changes dramatically. When the external applied pressure is removed between device geometry changes, the liquid metal

morphology remains unchanged, which can be regarded as a form of pressure memory. Once the device is fully filled with liquid metal, it can be erased through the use of mechanical pressure and exposure to acid vapors.

In Chapter 8, we demonstrate fabrication of free-standing two-dimensional (2D) and three-dimensional (3D) THz metamaterials via injection molding of gallium, a metal that melts at temperatures just slightly above room temperature. Molds are created by inscribing the desired microchannel geometries in one or two PDMS films using conventional soft lithography techniques and then reversibly bonding the two films together using van der Waals forces. After heating gallium above its melting point, the liquid metal is injected into the mold. The metal does not solidify even after cooling the filled mold at -16 °C for 24 hours. However, when the liquid metal comes into contact with solid gallium at room temperature, the entire device solidifies within the mold immediately. The PDMS films can then be peeled away, yielding a free-standing solid gallium structure. We fabricate a 2D split ring resonator-based metamaterial, and demonstrate three different approaches for creating 3D metamaterials: a multilayer stack, a manually folded structure that maintains its shape after folding and a directly injection molded 3D structure. The transmission properties of these devices are measured using THz time-domain spectroscopy and are shown to not suffer from limitations imposed by substrates.

In Chapter 9, we demonstrate gallium is a good candidate for 3D printing where relatively low temperatures are required for fabricating solid metallic structure. This method mainly uses solid gallium to pull liquid gallium outside of the print nozzle so that no pressure is required to the syringe reservoir. Liquid/solid phase transitions play an

important role in this method. By controlling the solidification process, we demonstrate that it can produce various 3D structures. Since the melting temperature of gallium is only ~30 °C, printed structures can be melted by the heat of a human hand into bulk liquid and reused. This 3D printing method can produce a minimum resolution that is smaller than the diameter of the printing needle by properly controlling the moving speed of substrate.

In Chapter 10, we discuss the future work that can be extended from current study, and present the conclusions drawn from previous chapters.

1.5 References

1. D. Dragoman, and M. Dragoman, "Terahertz fields and applications," Prog. Quant. Electron. **28**, 1–66 (2004).

2. M. C. Hoffmann, and J. A. Fulop, "Intense ultrashort terahertz pulses: generation and applications," J. Phys. D: Appl. Phys. **44**, 083001 (2011).

3. D. You, R. R. Jones, and P. H. Bucksbaum, "Generation of high-power sub-single-cycle 500-fs electromagnetic pulses," Opt. Lett. **18**, 290–292 (1993).

4. K. H. Yang, P. L. Richards, and Y. R. Shen, "Generation of far-infrared radiation by picosecond light pulses in LiNbO3," Appl. Phys. Lett. **19**, 320 (1971).

5. L. Xu, X.-C. Zhang, and D. H. Auston, "Terahertz beam generation by femtosecond optical pulses in electro-optic materials," Appl. Phys. Lett. **61**, 1784 (1992).

6. H. Hamster, A. Sullivan, S. Gordon, and R. W. Falcoone, "Short-pulse terahertz radiation from high-intensity-laser-produced plasmas," Phys. Rev. E **49**, 671–681 (1994).

7. M. D. Thomson, M. Kreb, T. Loffler, and H. G. Roskos, "Broadband THz emission from gas plasmas induced by femtosecond optical pulses" From fundamentals to applications," Laser & Photo. Rev. **1**, 349–368 (2007).

8. S. Preu, G. H. Dohler, S. Malzer, L. J. Wang, and A. C. Gossard, "Tunable, continuous-wave terahertz photomixer sources and applications," J. Appl. Phys. **109**, 061301 (2011).

9. Y.Takida, T. Ohira, Y. Tadokoro, H. Kumagai, and S. Nashima, "Tunable picosecond terahertz-wave parametric oscillators based on noncollinear pump-enhanced signal-resonant cavity," IEEE. J. Sel. Top. Quant. **19**, 8500307 (2013).

10. F. Capasso, R. Paiella, R. Martini, R. Colombelli, C. Gmachl, T. L. Myers, M. S. Taubman, R. M. Williams, C. G. Bethea, K. Unterrainer, H. Y. Hwang, D. L. Sivco, A. Y. Cho, A. M. Sergent, H. C. Liu, and E. A. Whittaker, "Quantum cascade lasers: ultrahigh-speed operation, optical wireless communication, narrow linewidth, and far-infrared emission," IEEE. J. Sel. Top. Quant. **38**, 511–532 (2002).

11. E. Rouvalis, C. C. Renaud, D. G. Moodie, M. J. Robertson, and A. J. Seeds, "Traveling-wave uni-traveling carrier photodiodes for continuous wave THz generation," Opt. Express **18**, 11105–11110 (2010).

12. P. H. Siegel, "Terahertz Technology," IEEE T. Microw. Theory **50**, 910–928 (2002).

13. T. Yasui, A. Nishimura, T. Suzuki, K. Nakayama, and S. Okajima, "Detection system operating at up to 7 THz using quasioptics and Schottky barrier diodes," Rev. Sci. Instrum. **77**, 066102 (2006).

14. D. P. Neikirk, W. W. Lam, and D. B. Rutledge, "Far-infrared microbolometer detectors," Int. J. Infrared Millim. Waves **5**, 245–278 (1984).

15. S. Ariyoshi, C. Otani, A. Dobroiu, H. Sato, K. Kawase, H. M. Shimizu, T. Taino, and H. Matsuo, "Terahertz imaging with a direct detector based on superconducting tunnel junctions," Appl. Phys. Lett. **88**, 203503 (2006).

16. S. Komiyama, O. Astafive, V. Antonov, T. Kutsuwa, and H. Hirai, "A single-photon detector in the far-infrared range," Nature **403**, 405–407 (2000).

17. M. V. Exter, and D. R. Grischkowsky, "Characterization of an optoelectronic terahertz beam system," IEEE T. Microw. Theory **38**, 1684–1691 (1990).

18. M. Tonouchi, "Cutting-edge terahertz technology," Nature Photon. **1**, 97–105 (2007).

19. B. Ferguson, and X.-C. Zhang, "Materials for terahertz science and technology," Nature Mater. **1**, 26–33 (2002).

20. T. G. Phillips, and J. Keene, "Submillimeter astronomy," Proc. IEEE **80**, 1662–1678 (1992).

21. M. C. Kemp, "Millimetre wave and terahertz technology for the detection of concealed threats-a review," Proc. Of SPIE **6402**, 64020D (2006).

22. Y. L. Hor, F. F. Federici, and R. L. Wample, "Nondestructive evaluation of cork enclosures using terahertz/millimeter wave spectroscopy and imaging," Appl. Opt. **47,** 72–78 (2008).

23. J. Federici, and L. Moeller, "Review of terahertz and subterahertz wireless communications," J. Appl. Phys. **107**, 111101 (2010).

24. I. F. Akyildiz, J. M. Jornet, and C. Han, "Terahertz band: Next frontier for wireless communications," Phys. Com. **12**, 16 (2014).

25. R. A. Shelby, D. R. Smith, and S. Schultz, "Experimental verification of a negative index of refraction," Science **292**, 77–79 (2001).

26. D. R. Smith, W. J. Padilla, D. C. Vier, S. C. Nemat-Nasser, and S. Schultz, Phys. Rev. Lett. **84**, 4184–4187 (2000).

27. T. Driscoll, H.-T. Kim, B.-G. Chae, B.-J. Kim, Y.-W. Lee, N. M. Jokerst, S. Palit, D. R. Smith, M. D. Ventra, and D. N. Basov, "Memory metamaterials," Science **325**, 1518–1521 (2009).

28. J. Zhu, and G. V. Eleftheriades, "A compact transmission-line metamaterial antenna with extended bandwidth," IEEE Antenn. Wirel. Pr. **8**, 295 (2009).

29. J. B. Pendry, D. Schurig, and D. R. Smith, "Controlling electromagnetic fields," Science **312**, 1780–1782 (2006).

30. D. Schurig, J. J. Mock, B. J. Justice, S. A. Cummer, J. B. Pendry, A. F. Starr, and D. R. Smith, "Metamaterial electromagnetic cloak at microwave frequencies," Science **314**, 977–980 (2006).

31. N. Landy, and D. R. Smith, "A full-parameter unidirectional metamaterial cloak for microwaves," Nature Mater. **12**, 25–28 (2013).

32. C. M. Soukoulis, and M. Wegener, "Past achievements and future challenges in the development of three-dimensional photonic metamaterials," Nature Photon. **5**, 524–530 (2011).

33. N. Liu, H. Guo, L. Fu, S. Kaiser, H. Schweizer, and H. Giessen, "Three-dimensional photonic metamaterials at optical frequencies," Nature **7**, 31–37 (2008).

34. V. M. Shalaev, W. Cai, U. K. Chettiar, H.-K. Yuan, A. K. Sarychev, V. P. Drachev, and A. V. Kildishev, "Negative index of refraction in optical metamaterials," Opt. Lett. **30**, 3356–3358 (2005).

35. J. Valentine, S. Zhang, T. Zentgraf, E. Ulin-Avila, D. A. Genov, G. Bartal, and X. Zhang, "Three-dimensional optical metamaterial with a negative refractive index," Nature **455**, 376–380 (2008).

36. J. Valentine, J. Li, T. Zentgraf, G. Bartal, and X. Zhang, "An optical cloak made of dielectrics," Nature Mater. **8**, 568–571 (2009).

37. P. Moitra, Y. Yang, Z. Anderson, I. I. Kravchenko, D. P. Briggs, and J. Valentine, "Realization of an all-dielectric zero-index optical metamaterial," Nature Photon. **7**, 791–795 (2013).

38. D. B. Burckel, J. R. Wendt, G. A. Ten Eyck, J. C. Ginn, A. R. Ellis, I. Brener, and M. B. Sinclair, "Micrometer-scale cubic unit cell 3D metamaterial layers," Adv. Mater. **22**, 5053–5057 (2010).

39. H.-T. Chen, J. F. O'Hara, A. K. Azad, A. J. Taylor, R. D. Averitt, D. B. Shrekenhamer, and W. J. Padilla, "Experimental demonstation of frequency-agile terahertz metamaterials," Nature **2**, 295–298 (2008).

40. N. I. Landy, S. Sajuyigbe, J. J. Mock, D. R. Smith, and W. J. Padilla, "Perfect metamaterial absorber," Phys. Rev. Lett. **100**, 207402 (2008).

41. M. Choi, S. H. Lee, Y. Kim, S. B. Kang, J. Shin, M. H. Kwak, K.-Y. Kang, Y.-H. Lee, N. Park, and B. Min, "A terahertz metamaterial with unnaturally high refractive index," Nature **470**, 369–374 (2011).

42. S. Zhang, Y.-S. Park, J. Li, X. Lu, W. Zhang, and X. Zhang, "Negative refractive index in chiral metamaterials," Phys. Rev. Lett. **102**, 023901 (2009).

43. L. Cong, N. Xu, J. Gu, R. Singh, J. Han, and W. zhang, "Highly flexible broadband terahertz metamaterial quarter-wave plate," Laser Photonics Rev. **8**, 626–632 (2014).

44. H.-T. Chen, W. J. Padilla, M. J. Cich, A. K. Azad, R. D. Averitt, and A. J. Taylor, "A metamaterial solid-state terahertz phase modulator," Nature Photon. **3**, 148–151 (2009).

45. M. Dragoman, and D. Dragoman, "Plasmonics: applications to nanoscale terahertz and optical devices," Prog. Quant. Electron. **32**, 1–41 (2008).

46. S. Hayashi, and T. Okamoto, "Plasmonics: visit the past to know the future," J. Phys. D: Appl. Phys. **45**, 433001 (2012).

47. T. W. Ebbesen, H. J. Lezec, H. F. Ghaemi, T. Thio, and P. A. Wolff, "Extraordinary optical transmission through sub-wavelength hole arrays," Nature **391**, 667–669 (1998).

48. D. K. Gramotnev, and S. I. Bozhevolnyi, "Plasmonics beyond the diffraction limit," Nature Photon. **4**, 83–91 (2010).

49. E. Ozbay, "Plasmonics: merging photonics and electronics at nanoscale dimensions," Science **311**, 189 (2006).

50. J. A. Schuller, E. S. Barnard, W. Cai, Y. C. Jun, J. S. White, and M. L. Brongersma, "Plasmonics for extreme light concentration and manipulation," Nature Mater. **9**, 193–204 (2010).

51. J. N. Anker, W. P. Hall, O. Lyandres, N. C. Shah, J. Zhao, and R. P. V. Duyne, "Biosensing with plasmonic nanosensors," Nature **7**, 442–453 (2008).

52. A. G. Brolo, "Plasmonics for future biosensors," Nature Photon. **6**, 709–713 (2012).

53. F. De Angelis, F. Gentile, F. Mecarini, G. Das, M. Moretti, P. Candeloro, M. L. Coluccio, G. Cojoc, A. Accardo, C. Liberale, R. P. Zaccaria, G. Perozziello, L. Tirinato, A. Toma, G. Cuda, R. Cingolani, and E. Di Fabrizio, "Breaking the diffusion limit with super-hydrophobic delivery of molecules to plasmonic nanofocusing SERS structures," Nature Photon. **5**, 682–687 (2011).

54. S. J. Lee, Z. Guan, H. Xu, and M. Moskovits, "Surface-enhanced raman spectroscopy and nanogeometry: the plasmonic origin of SERS," J. Phys. Chem. C **111**, 17985–17988 (2007).

55. H. A. Atwater, and A. Polman, "Plasmonics for improved photovoltaic devices," Nature Mater. **9**, 205–213 (2010).

56. M. A. Green, and S. Pillai, "Harnessing plasmonics for solar cells," Nature Photon. **6**, 130–132 (2012).

57. M. G. Blaber, M. D. Arnold, and M. J. Ford, "A review of the optical properties of alloys and intermetallics for plasmonics," J. Phys.: Condens. Matter **22**, 143201 (2010).

58. A. Boltasseva, and H. A. Atwater, "Low-loss plasmonic metamaterials," Science **331**, 290–291 (2011).

59. P. R. West, S. Ishii, G. V. Naik, N. K. Emani, V. M. Shalaev, and A. Boltasseva, "Searching for better plasmonic materials," Laser Photonics Rev. **4**, 795–808 (2010).

60. M. A. Ordal, L. L. Long, R. J. Bell, S. E. Bell, R. R. Bell, R. W. Alexander, Jr., and C. A. Ward, "Optical properties of the metals Al, Co, Cu, Au, Fe, Pb, Ni, Pd, Pt, Ag, Ti, and W in the infrared and far infrared," Appl. Opt. **22**, 1099–1120 (1983).

61. J. G. Rivas, C. Schotsch, P. H. Bolivar, and H. Kurz, "Enhanced transmission of THz radiation through subwavelength holes," Phys. Rev. B **68**, 201306 (2003).

62. P. Sen, and C.-J. Kim, "Microscale liquid-metal switches — a review," IEEE T Ind. Electron. **56**, 1314–1329 (2009).

63. S. R. C. Vivekchand, C. J. Engel, S. M. Lubin, M. G. Blaber, W. Zhou, J. Y. Suh, G. C. Schatz, and T. W. Odom, "Liquid plasmonics: manipulating surface plasmon polaritions via phase transitions," Nano Lett. **12**, 4324–4328 (2012).

64. J. H. So, H.-J. Koo, M. D. Dickey, and O. D. Velev, "Ionic current rectification in soft-matter diodes with liquid-metal electrodes," Adv. Funct. Mater. **22**, 625–631 (2012).

65. D. J. Lipomi, B. C.-K. Tee, M. Vosgueritchian, and Z. Bao, "Stretchable organic solar cells," Adv. Mater. **23**, 1771–1775 (2011).

66. H.-H. So, and M. D. Dickey, "Inherently aligned microfluidic electrodes composed of liquid metal," Lab Chip **11**, 905–911 (2011).

67. I. Dutta, and P. Kumar, "Electric current induced liquid metal flow: application to coating of micropatterned structures," Appl. Phys. Lett. **94**, 184104 (2009).

68. S. Talukder, N. Somaiah, and P. Kumar, "Effect of substrate surface roughness on electric current induced flow of liquid metals," Appl. Phys. Lett. **102**, 054101 (2013).

69. Y.-L. Park, C. Majidi, R. Kramer, P. Berard, and R. J. Wood, "Hyperelastic pressure sensing with a liquid-embedded elastomer," J. Micromech. Microeng. **20**, 125029 (2010).

70. D. M. Vogt, Y.-L. Park, R. J. Wood, "Design and characterization of a soft multi-axis force sensor using embedded microfluidic channels," IEEE Sens. J. **13**, 4056–4064 (2013).

71. S. Cheng, and Z. Wu, "A microfluidic, reversibly stretchable, large-area wireless strain sensor," Adv. Funct. Mater. **21**, 2282–2290 (2011).

72. M. G. Mohammed, M. D. Dickey, "Strain-controlled diffraction of light from stretchable liquid metal micro-components," Sensor Actuat. A.: Phys **193**, 246–250 (2013).

73. S. Cheng, A. Rydberg, K. Hjort, and Z. Wu, "Liquid metal stretchable unbalanced loop antenna," Appl. Phys. Lett. **94**, 144103 (2009).

74. J.-H. So, J. Thelen, A. Qusba, G. J. Hayes, G. Lazzi, and M. D. Dickey, "Reversibly deformable and mechanically tunable fluidic antennas," Adv. Funct. Mater. **19**, 3632–3637 (2009).

75. M. Kubo, X. Li, C. Kim, M. Hashimoto, B. J. Wiley, D. Ham, and G. M. Whitesides, "Stretchable microfluidic radiofrequency antennas,"Adv. Mater. **22**, 2749–2752 (2010).

76. S. Zhu, J.-H. So, R. Mays, S. Desai, W. R. Barnes, B. Pourdeyhimi, and M. D. Dickey, "Ultrastretchable fibers with metallic conductivity using a liquid metal alloy core," Adv. Funct. Mater. **23**, 2308–2314 (2013).

77. E. Palleau, S. Reece, S. C. Desai, M. E. Smith, and M. D. Dickey, "Self-healing stretchable wires for reconfigurable circuit wiring and 3D microfluidics," Adv. Mater. **25**, 1589–1592 (2013).

78. M. J. Regan, H. Tostmann, P. S. Pershan, O. M. Magnussen, E. DiMasi, B. M. Ocko, and M. Deutsch, "X-ray study of the oxidation of liquid-gallium surfaces," Phys. Rev. B **55**, 10786–10790 (1997).

79. R. J. Larsen, M. D. Dickey, and G. M. Whitesides, "Viscoelastic properties of oxide-coated liquid metals," J. Rheol. **53**, 1305–1326 (2009).

80. Q. Xu, N. Oudalov, Q. Guo, H. M. Jaeger, and E. Brown, "Effect of oxidation on the mechanical properties of liquid gallium and eutectic gallium-indium," Phys. Fluids **24**, 063101 (2012).

81. R. K. Kramer, J. W. Boley, H. A. Stone, J. C. Weaver, and R. J. Wood, "Effect of microtextured surface topography on the wetting behavior of eutectic gallium-indium alloys," Langmuir **30**, 533–539 (2014).

82. G. Li, M. Parmar, D. Kim, J.-B. Lee, and D.-W. Lee, "PDMS based coplanar microfluidic channels for the surface reduction of oxidized Galinstan," Lab Chip **14**, 200–209 (2014).

83. T. Hutter, W.-A. C. Bauer, S. R. Elliott, and W. T. S. Huck, "Formation of spherical and non-spherical eutectic gallium-indium liquid-metal microdroplets in microfluidic channels at room temperature," Adv. Funct. Mater. **22**, 2624–2631 (2012).

84. J. Thelen, M. D. Dickey, and T. Ward, "A study of the production and reversible stability of EGaIn liquid metal microspheres using flow focusing," Lab Chip **12**, 3961–3967 (2012).

85. J. N. Hohman, M. Kim, G. A. Wadsworth, H. R. Bednar, J. Jiang, M. A. LeThai, and P. S. Weiss, "Directing substrate morphology via self-assembly: ligand-mediated scission of gallium-indium microspheres to the nanoscale," Nano Lett. **11**, 5104–5110 (2011).

86. R. C. Chiechi, E. A. Weiss, M. D. Dickey, and G. M. Whitesides, "Eutectic gallium–indium (EGaIn): a moldable liquid metal for electrical characterization of self-assembled monolayers," Angew. Chem. **120,** 148–150 (2008).

87. M. D. Dickey, R. C. Chiechi, R. J. Larsen, E. A. Weiss, D. A. Weitz, and G. M. Whitesides, "Eutectic gallium-indium (EGaIn): a liquid metal alloy for the formation of stable structures in microchannels at room temperature," Adv. Funct. Mater. **18**, 1097–1104 (2008).

88. M. R. Khan, G. J. Hayes, J.-H. So, G. Lazzi, and M. D. Dickey, "A frequency shifting liquid metal antenna with pressure responsiveness," Appl. Phys. Lett. **99**, 013501 (2011).

89. B. L. Cumby, G. J. Hayes, M. D. Dickey, R. S. Justice, C. E. Tabor, and J. C. Heikenfeld, "Reconfigurable liquid metal circuits by Laplace pressure shaping," Appl. Phys. Lett. **101**, 174102 (2012).

90. C. Yang, S.-Y. Wu, C. Glick, Y. S. Choi, W. Hsu, and L. Lin, Micro Electro Mechanical Systems (MEMS), 2015, 28th IEEE International Conference on, 261, 18–22 Jan. 2015.

91. C. Ladd, J.-H. So, J. Muth, and M. D. Dickey, "3D printing of free standing liquid metal microstructures," Adv. Mater. **25**, 5081–5085 (2013).

CHAPTER 2

DEVICE FABRICATION AND MEASUREMENT

2.1 Device Fabrication of Liquid Metal Structures

2.1.1 Solid Template

We fabricated liquid metal-based metamaterial devices using standard soft lithography techniques. We started from a solid template that served as a master for PDMS replication. The solid template was either a patterned stainless steel on a glass substrate or a patterned SU-8 photoresist on a silicon substrate. Stainless steel was used when the feature size was hundreds of micrometers. We used an epoxy glue to adhere steel with the glass substrate. Photoresist was used when the feature size was several micrometers to tens of micrometers. Between patterned photoresist and silicon substrate, we used blank photoresist as a buffer layer so that PDMS did not stick to silicon in the following process. To do so, we first coated a silicon wafer with SU-8 photoresist and spun it to several micrometers. This film was exposed to UV light using a blank mask to form a flat layer without any pattern, which was used to improve the adhesion between the silicon wafer and the upper SU-8 patterned layer. Then a second layer of SU-8 photoresist was spun cast. UV lithography using a mask with a designed pattern yielded an upper photoresist layer, which served as the template for soft lithography.

2.1.2 Soft Lithography

Figure 2.1 shows the schematic diagram for the basic process flow of fabricating liquid metal-based devices. After obtaining the template, we put several solid spacers on the top of the substrate but outside of the pattern areas. The spacer determined the thickness of the replicated PDMS film. A PDMS prepolymer was then mixed with a curing agent using a volume ratio between 7:1 and 11:1, degassed, poured onto the SU-8 template, covered with a flat solid plastic and cured for 2 hours at 60 °C. Different ratios of prepolymer and curing agent lead to different stiffness of the cured PDMS. Larger ratios corresponded to softer PDMS. The solid cover was used to obtain a flat surface of cured PDMS film, which was necessary for normally incident terahertz transmission measurement. We used a plastic Petri dish for this because it was easy to separate after curing. Once cured, the inverse PDMS replicas were peeled off the master. Based on the need, these PDMS replicas were bonded with another PDMS film, glass or metal film. The bonding could be reversible by just touching them together or irreversible by using high voltage corona or chemicals. A metamaterial structure was formed by injecting

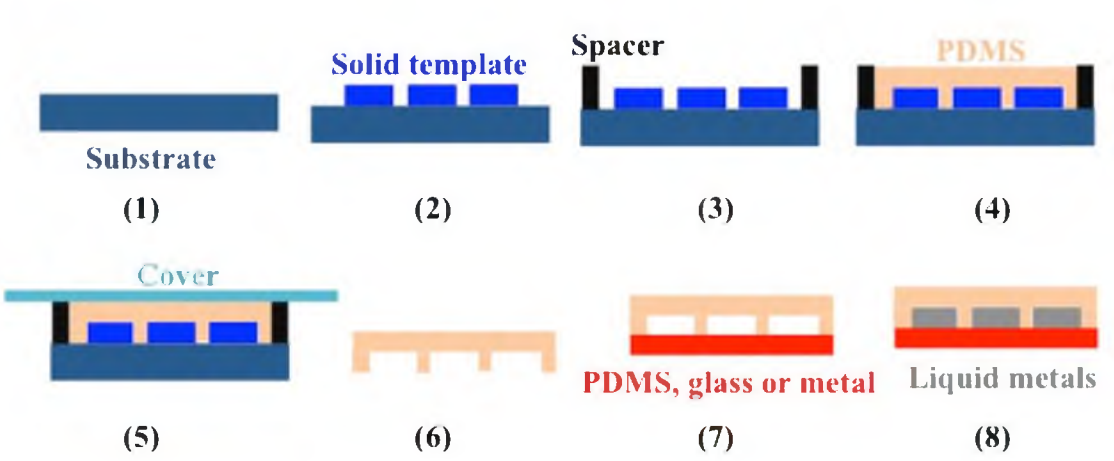

Figure 2.1. Process flow for fabrication of liquid metal-based metamaterial devices.

EGaIn into the microchannels.

2.2 3D Printing Technique

The process of 3D printing solid gallium structures is different from that for fabricating liquid metal-based metamaterials. We started with a solid seed layer of gallium. To make the printed gallium adhere to the glass substrate, we deposited a thin layer of liquid gallium from a pair of tweezers to the top of the substrate. We then solidified this layer by contacting it with a piece of solid gallium. We found the solidification was necessary because the printed liquid gallium did not necessarily solidify when cooled well below its freezing point if the seed was a liquid. We then filled a syringe with liquid gallium. When the syringe was pressed to push liquid gallium out of the needle, it quickly formed a spherical ball with a diameter much larger than the diameter of the needle. We removed the spherical ball of gallium by moving the substrate downward. This pulled a line of liquid gallium out of the needle. The line of liquid gallium broke at a point because it was liquid. The resultant conical protrusion of liquid gallium at the needle side was used as the contact point for the next step.

In the third step, we contacted the gallium seed on the substrate with the liquid gallium conical protrusion at the needle tip, and cooled the substrate with a Peltier cooler. The substrate and cooler were amounted on a 3-axis microstage. Once the gallium seed and gallium from the needle contacted, we slowly moved the substrate down. The solid gallium at the solid/liquid interface pulled the liquid gallium out of the needle so no pressure was required from the syringe. This is different from most 3D printers where the filament is often pushed out of the nozzle. By controlling the position of this interface,

we were able to obtain different 3D structures.

2.3 Terahertz Time-Domain Spectroscopy

We used terahertz time-domain spectroscopy (THz-TDS) for all of the transmission measurements in this dissertation. A schematic diagram for the THz time-domain spectrometer is shown in Figure 2.2(a). THz-TDS is a coherent detection system where an ultrafast femtosecond pulse beam is split into two beams. The pump beam is used to generate THz radiation, while the probe beam is used to detect THz signal and acts as an optical gate. We used photoconductive antennas as both THz emitter and detector in our experiments. Figure 2.2(b) shows a schematic diagram of the emitter, which consists of a patterned metallic transmission line with a dipole geometry on a GaAs substrate. When a femtosecond laser with photon energy larger than the band gap of GaAs is incident on the gap area of the dipole, electron-hole pairs are created. The carrier density changes rapidly in response to the femtosecond pulse. Generated carriers under a biased electrical field will form a transient current. Both the acceleration of carriers under the electrical field and the change of carrier density due to femtosecond pulse excitation contribute to the final photocurrent change, although the carrier density change plays a more important role [1]. According to Maxwell's equation, this time-varying current generates electromagnetic radiation. When the current modulation occurs in the sub-picosecond regime, a radiated THz electric field is obtained [2]. For photoconductive antenna detectors, the THz radiation serves as bias electrical field to accelerate the carriers generated by probe femtosecond beam. The output current is proportional to THz electrical field and carrier density [1, 3].

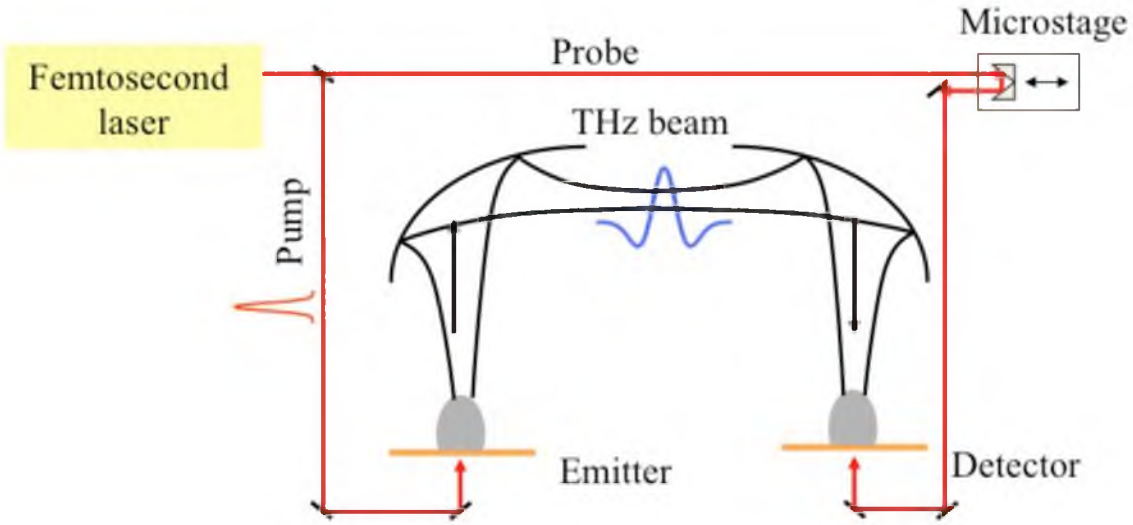

(a)

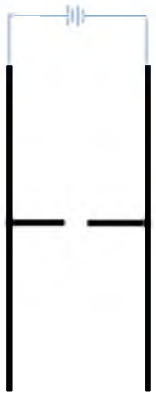

(b)

Figure 2.2 Terahertz time-domain spectroscopy. (a) Schematic diagram of terahertz time-domain spectrometer. (b) Photoconductive antenna for the emitter.

During measurement, we mounted samples on a metal frame that had an opening size that matched the sample size. Samples were placed in the path of the collimated THz beam. For a large array, we used a pair of off-axis paraboloidal mirrors to collect, collimate and refocus the THz radiation from the emitter to the detector. For small samples, we used one paraboloidal mirror to collect and collimate the THz radiation and placed the detector close to the sample. Two separate reference transmission spectra were taken: one with a blank metal frame (air reference) for absolute transmission and one with the same thick dielectric substrates in the frame (dielectric reference) for normalized transmission. The latter reference eliminates the effect of THz absorption in dielectric films.

In contrast to conventional optical measurements, THz-TDS allows for the direct measurement of the THz electric field, yielding both amplitude and phase information. By Fourier transform, we can obtain transmission coefficient, t(ν), using the relation

$$t(\nu) = |t(\nu)|\exp[i\varphi(\nu)] = \frac{E_{sample}(\nu)}{E_{reference}(\nu)} \qquad (2.1)$$

E_{sample} and $E_{reference}$ are the measured THz electric fields with either the sample or reference in the beam path, respectively, and $|t(\nu)|$ and $\varphi(\nu)$ are the magnitude and phase of the transmission coefficient, respectively.

2.4 References

1. Z. Piao, M. Tani, and K. Sakai, "Carrier dynamics and terahertz radiation in photoconductive antennas," Jpn. J. Appl. Phys. **39**, 96–100 (2000).

2. P. U. Jepsen, R. H. Jacobsen, and S. R. Keiding, "Generation and detection of terahertz pulses from biased semiconductor antennas," J. Opt. Soc. Am. B **13**, 2424–2436 (1996).

3. J. Zhang, Y. Hong, S. L. Braunstein, K. A. Shore, "Terahertz pulse generation and detection with LT-GaAs photoconductive antenna," IEE Proc.-Optoelectron. **151**, 98–101 (2004).

CHAPTER 3

LIQUID METAL-BASED PLASMONICS

3.1 Introduction

The field of plasmonics has grown dramatically over the last decade, because surface plasmon polaritons (SPPs) offer a number of unique capabilities for manipulating and guiding electromagnetic radiation [1]. Much of the current research effort in this field is focused on studies at visible frequencies, where gold and silver are the primary metals used. Most other metals exhibit unreasonably high propagation losses. However, as one moves to longer wavelengths, such as the terahertz (THz) and microwave spectral ranges, conventional metals, including stainless steel and aluminum, exhibit high conductivities, and correspondingly low propagation losses [2]. Moreover, numerous non-metals that are highly conducting have been shown to support SPP propagation, including doped semiconductors [3], conducting polymers [4], and graphene [5]. In this latter class of materials, it is possible to alter the conductivity of the medium through electrical, optical, thermal, and chemical means. A change in the conductivity can alter the propagation losses associated with SPPs, which, in turn, can be used to create active THz device capabilities. However, such changes typically alter only the resonance quality [6]. It would be highly desirable to use a plasmonic medium that allows for tunable and reconfigurable device architectures.

A metallic medium that is highly flexible and can flow at room temperature, such as a liquid metal, satisfies such desires. In this approach, a liquid metal would be injected into microfluidic channels formed within a flexible mold. Such structures are commonly fabricated using soft lithography techniques with polydimethylsiloxane (PDMS) for a variety of microfluidic applications [7,8]. An obvious liquid metal that flows readily at room temperature is mercury, Hg. However, mercury is highly toxic, and acts to

minimize interfacial free energy. This latter effect can create unstable structures within microfluidic channels. Recently, Dickey and co-workers have shown that eutectic gallium indium (EGaIn) is an attractive alternative to Hg [9,10]. EGaIn is composed of 78.6% Ga and 21.4% In by weight, has a melting temperature of ~15.5° C, and forms a thin oxide skin within elastomeric channels to provide mechanical stability to the fluid. In addition, EGaIn has a DC conductivity of 3.4×10^4 S/cm [9]. This value is an order of magnitude smaller than that of aluminum [2], for example, but is greater than that of some of the non-metals mentioned above [4].

In this work, we demonstrate the utility of liquid metals for plasmonics applications. Specifically, we demonstrate enhanced THz transmission through periodic aperture arrays [11,12] fabricated by injection of EGaIn into an elastomeric PDMS mold. In order to explain the observations, we separately measure the complex THz refractive index of PDMS and the complex dielectric constant of EGaIn. An important aspect of the constituent materials is that they are amenable to stretching and flexing. We exploit this characteristic by measuring the transmission properties of the structures while being stretched. This represents a simple demonstration of mechanically tuning the plasmonic resonance properties of the device.

3.2 Experimental Details

We fabricated periodic aperture arrays using PDMS, a silicone elastomer (Sylgard 184 kit, Dow Corning), and EGaIn, a liquid metal. PDMS is a commercially available elastomer that is commonly used for microfluidic applications, and allows for fabrication using standard soft lithography processes [7,8]. In order to create the microfluidic mold,

we first fabricated 15x15 arrays of periodically spaced subwavelength apertures in free-standing 75μm thick stainless steel metal foils. The apertures had a diameter of 357 μm with a periodicity of 714 μm on a square lattice.

The perforated foils were then adhered to glass substrates using a thin (<10 μm) layer of epoxy. A PDMS pre-polymer was mixed with a curing agent using a weight ratio of 11:1, degassed, poured onto the stainless steel molds, and cured for 2 hours at 60 °C. After curing, the inverse PDMS replicas were peeled off the molds and sealed with a planar section of PDMS using a high voltage corona, yielding an overall device thickness of 1 mm. Finally, we injected EGaIn into the air voids of the PDMS structures, yielding periodic arrays of subwavelength apertures based on an encapsulated liquid metal. In Figure 3.1, we show a schematic diagram of the final structure with the relevant dimensions along with a micrograph of a section of an array. For reference purposes, we also fabricated a 1 mm thick planar PDMS film.

We used THz time-domain spectroscopy (THz-TDS) to measure the optical transmission spectra, t(ν), of the electric field through the liquid metal arrays, where ν is the THz frequency [13]. In contrast to conventional optical measurements, THz-TDS allows for the direct measurement of the THz electric field, yielding both amplitude and phase information. By transforming the time-domain data to the frequency domain, we are able to determine independently both the magnitude and phase of the amplitude transmission coefficient, t(ν), using the relation

$$t(\nu) = |t(\nu)|\exp[i\varphi(\nu)] = \frac{E_{sample}(\nu)}{E_{reference}(\nu)} \tag{3.1}$$

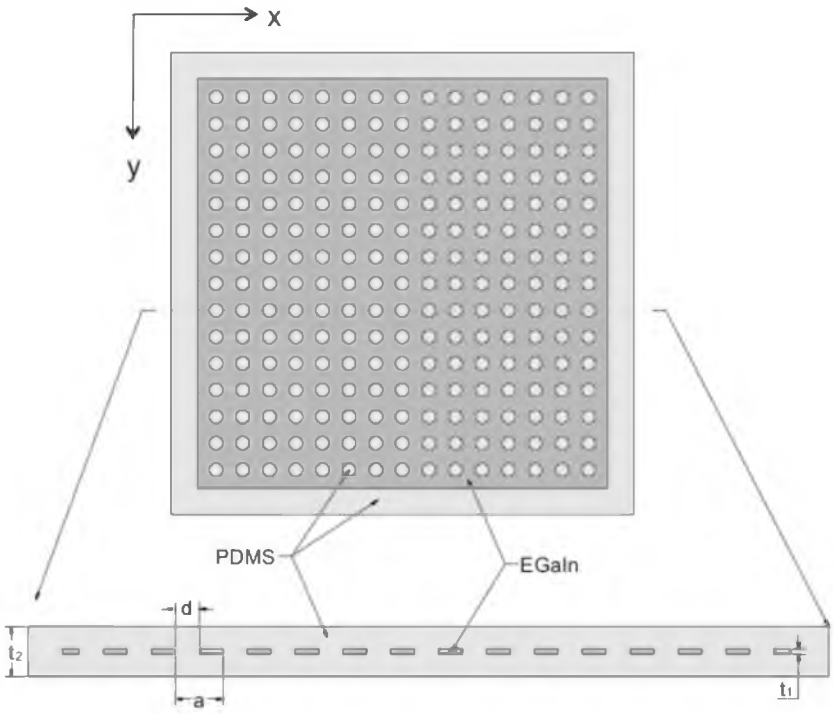

(a)

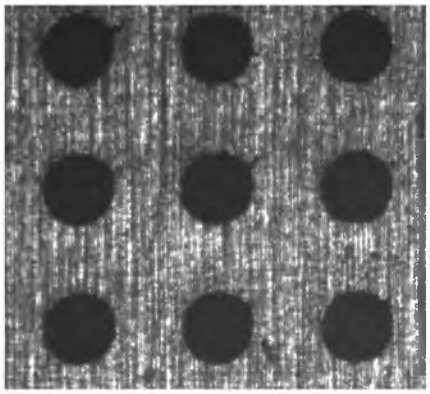

(b)

Figure 3.1. A periodic liquid metal aperture array. (a) Schematic diagram of the top view (above) and cross-section (below) of the liquid metal aperture array encapsulated in PDMS. The aperture diameter d = 357 μm, the periodic aperture spacing a = 714 μm, the liquid metal thickness t_1 = 80 μm, and total device thickness t_2 = 1 mm. (b) Photograph showing an expanded view of a portion of the array.

In this expression, E_{sample} and $E_{reference}$ are the measured THz electric fields with either the sample or reference in the beam path, respectively, and $|t(\nu)|$ and $\varphi(\nu)$ are the magnitude and phase of the amplitude transmission coefficient, respectively.

Each array was mounted on a metal frame in which the opening size exposed only the metallic portion of the liquid metal array. The framed sample was placed in the path of the collimated THz beam, between a pair of off-axis paraboloidal mirrors that were used to collect, collimate, and refocus the THz radiation from the emitter to the detector. The 1/e THz beam diameter was slightly larger than the aperture opening in the metal frame, thus edge effects due to the finite size of the array sample may play a role in the resulting transmission spectra [14]. In each case, the incident THz radiation was polarized parallel to a major axis of the array. Two separate reference transmission spectra were taken: one with a blank metal frame (air reference) and one with the 1 mm thick planar PDMS film in the frame (PDMS reference). The latter reference eliminates the effect of THz absorption in PDMS.

Finally, we also measured the THz dielectric properties of EGaIn. The liquid metal is completely opaque and highly reflective at visible frequencies using a thin film that is ~ 2 μm thick. For this thickness, there is also no THz transmission through the liquid metal film. While it is possible to create thinner films using evaporation or sputtering techniques, the resulting film may not have the same composition as the starting metal and the composition is sensitive to the deposition conditions. Therefore, we performed THz TDS using s-polarized THz radiation in a reflection geometry to examine the properties of the liquid metal. To do so, we deposited a 2 μm thick Au film on half of a smooth metallic substrate and spread a 2 μm thick EGaIn layer on the other half. Based

on the DC conductivity of EGaIn, this thickness is greater than 2 skin depths above 50 GHz. Identical results were obtained using thicker EGaIn thicknesses.

3.3 Experimental Results and Discussion

We begin by characterizing the complex dielectric properties of EGaIn, since this is necessary to demonstrate that it is capable of supporting SPPs. As noted above, we measured the reflected THz spectra from both the Au surface, which was used as the reference, and the EGaIn surface. Experimentally, we found that the amplitude reflectivity from EGaIn was ~85% that of Au over the measured spectral range. In extracting the properties of EGaIn, we used measured dielectric properties of Au [15,16], rather than simply assuming that it behaves as a perfect reflector. In Figure 3.2, we show the measured values of the real and imaginary components of the dielectric constant of EGaIn between 0.1 – 0.5 THz, clearly demonstrating that it is metallic over the measured spectral range. Given the relatively small variation in the dielectric properties, however, it is not possible to find a unique fit for the data to a Drude type function. As mentioned earlier, the reflective nature of EGaIn at visible frequencies suggests that it may exhibit metallic properties over a broader spectral range.

Next, we measured the refractive index properties of PDMS, since this parameter is important in understanding the transmission spectra of the aperture arrays. In Figure 3.3, we show the measured values of the real and imaginary components of the refractive index. The real component of the THz refractive index in the range of 0.1 – 0.5 THz is relatively constant and has a value of ~1.57. The corresponding imaginary component is also largely frequency independent over that frequency range and has a value of ~0.04.

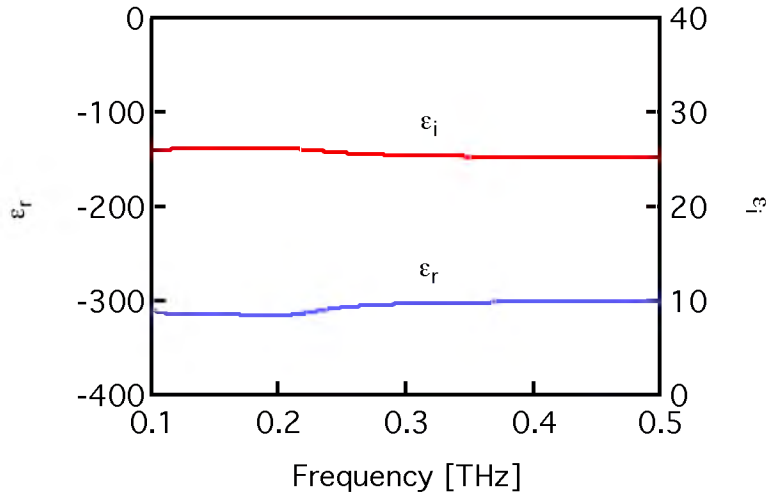

Figure 3.2. Measured complex dielectric constant of EGaIn.

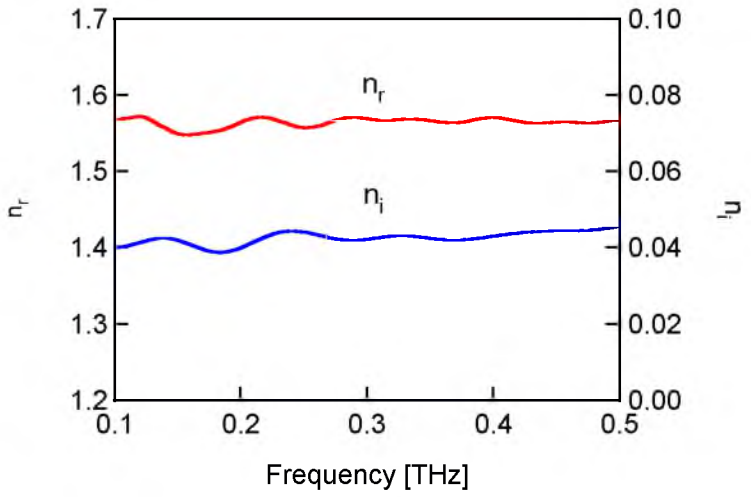

Figure 3.3. Measured complex refractive index of the PDMS used in the experiment. The PDMS pre-polymer and curing agents were mixed using a weight of ratio of 11:1.

Using this value of n_i, we can readily compute the frequency-dependent absorption coefficient, $\alpha(\nu) = 2\pi\nu n_i/c$, for the THz electric field, where the electric field decay is given by $\exp[-\alpha(\nu)d]$) and c is the speed of light in vacuum. Across the frequency range of interest, $\alpha \approx 0.25$ mm^{-1}, which corresponds to ~77% transmission through a 1 mm thick PDMS film. It is worth noting that the refractive index values that we find for PDMS differs significantly from published values across this same frequency range [17]. The source of this discrepancy is not clear at present, but may arise from a difference in the measured PDMS constituent mixture. As we demonstrate below, the refractive index values found here, both real and imaginary, are consistent with our aperture array transmission measurements.

We now move to the liquid metal aperture array transmission properties. In Figure 3.4(a), we show the measured transmission amplitude spectra for the liquid metal array using both air and a 1 mm thick PDMS film as references. Associated with each of the resonant peaks in the figure, there is an anti-resonance (AR) dip on the high frequency side of the resonance. It is this AR frequency that is important in understanding the experimental data. As we have shown previously, only the AR frequencies (rather than the resonance frequencies) remain fixed when the aperture diameter is varied [18]. Therefore, it is the AR frequencies that are the relevant and fundamental parameters rather than the frequencies of the resonance peaks. From the transmission spectrum we obtained the two AR frequencies at $\nu_{AR1} = 0.27$ THz and $\nu_{AR2} = 0.38$ THz.

We have previously demonstrated that the AR frequencies can be found directly from the spatial Fourier transform of the real space aperture geometry [19]. In the case of a periodic array, these AR frequencies are given analytically by [11]

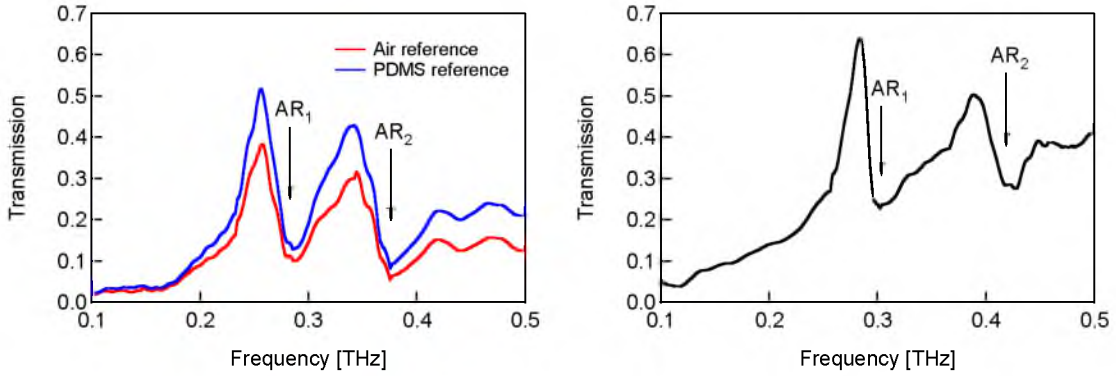

Figure 3.4. THz electric field transmission spectra, t(ν), of (a) 15x15 liquid metal array with 357 μm diameter apertures periodically spaced by 714 μm. Air and a 1 mm thick PDMS film are used as references. (b) 15x15 array with 400 μm diameter apertures periodically spaced by 1 mm in a 75 μm thick free-standing stainless steel foil with air as the reference.

$$\nu_{AR} = \frac{c}{P\, n_{SPP}} \sqrt{i^2 + j^2}\,, \tag{3.2}$$

where

$$n_{SPP} = \left[\frac{\varepsilon_m \varepsilon_d}{\varepsilon_m + \varepsilon_d} \right]^{1/2}. \tag{3.3}$$

In these equations, n_{SPP} is the effective refractive index for the propagating SPP, ε_m and ε_d are the complex dielectric constants of the metal and adjacent dielectric medium, P is the aperture periodicity, c is the speed of light in vacuum, and i and j are integers that index the resonance order. Since the magnitudes of the real and imaginary components of the complex dielectric constant of metals are much larger than those of dielectrics, n_{SPP}

typically takes a value very close to the refractive index of the dielectric medium (in this case, $n_{SPP} \cong n_{PDMS} \approx 1.57$). From Equation (3.2) the two lowest order AR frequencies occur for $i = \pm 1$, $j = 0$ (AR_1) and $i = \pm 1$, $j = \pm 1$ (AR_2).

Using Equations (3.1) and (3.2), the two lowest order AR frequencies are expected to occur at $\nu_{AR1} = 0.27$ THz and $\nu_{AR2} = 0.38$ THz, in excellent agreement with the experimental data. As expected, the transmission spectra using air as the reference is smaller in magnitude than that when PDMS is used as the reference. In fact, the 'air reference' transmission is only ~76% that of the 'PDMS reference.' This agrees well with expectations based on the measured imaginary component of the refractive index (Figure 3.3).

At this point, it is reasonable to compare the SPP enhanced transmission properties from the liquid metal hole arrays with those obtained using a more conventional metal hole array. In order to make a fair comparison, it should be noted that since the apertures in the liquid metal array are filled with the same medium that encapsulates the liquid metal on all sides (i.e., PDMS), the ratio of the effective aperture size to the effective aperture spacing remains constant and the dielectric refractive index serves to scale the effective periodicity [20]. Therefore, we also fabricated a 15×15 array of 400 μm diameter apertures on a square grid with an aperture spacing of 1 mm on a free-standing 75 μm thick stainless steel foil, since this geometry yields similar AR frequencies. In this case, only air was used as the reference. While the absolute transmission magnitude and the quality factor associated with the lowest order resonance for the stainless steel sample shown in Figure 3.4(b) is somewhat greater than that for the liquid metal sample, it is worth reiterating that the DC conductivity of the liquid metal is smaller than that of

stainless steel [2]. This is generally consistent with earlier observations of enhanced THz transmission through a periodic array of subwavelength apertures fabricated in heavily doped conducting polymers [4].

In contrast to rigid substrates, such as conventional metals typically used for plasmonics applications, PDMS and liquid metals lend themselves to the idea of creating mechanically tunable and reversibly stretchable plasmonic devices. In order to demonstrate this, we measured the THz transmission properties of the 15×15 liquid metal array as a function of elongation along the x-axis. In Figure 3.5(a), we show the measured transmission spectra of the array, with air as the reference, for three different degrees of stretching, corresponding to three different effective periodicities along the x-axis. It is apparent that ν_{AR1} does not shift in a linear manner. We therefore show the measured AR wavelength, λ_{AR1}, as a function of the fractional elongation along the x-axis in Figure 3.5(b), where the unstretched film with P=714 μm corresponds to 0% elongation and P = 806 μm corresponds to ~13% elongation. When the incident THz radiation was polarized parallel to the x-axis, we observed a linear increase in the AR wavelength with stretching. Such a variation is apparent when Equation (3.2) is rewritten as

$$\lambda_{AR} = \frac{P}{\sqrt{i^2 + j^2}} n_{SPP}. \tag{3.4}$$

However, when the incident THz radiation is polarized perpendicular to the stretch axis (i.e., along the y-axis), we observe a slight decrease in λ_{AR1} as the structure is stretched. The observed blue shift arises from the fact that stretching along the x-axis causes a small degree of compression along the y-axis. Over the stretching range used here, the array

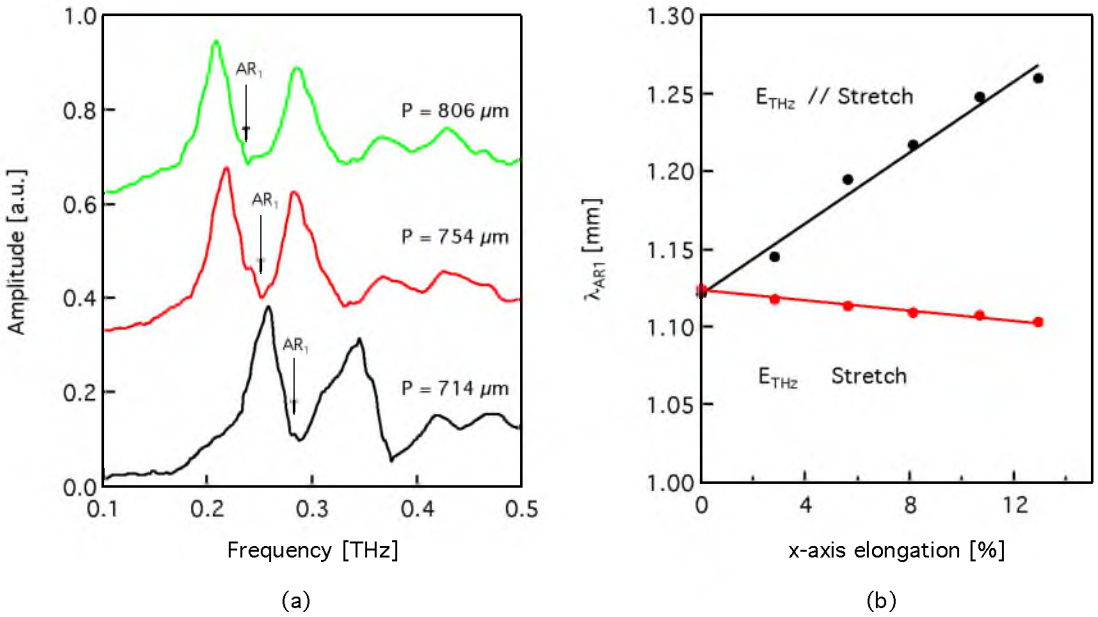

Figure 3.5. Transmission properties of the 15x15 liquid metal array as a function of stretching the device along the x-axis. (a) Measured transmission spectra for three different degrees of stretching (corresponding to different periodicities along the x-axis) with THz radiation polarized along the x-axis. The corresponding lowest order AR frequencies are marked. (b) Measured AR wavelength as a function of stretching for THz radiation polarized parallel (filled black circles) and perpendicular (filled red circles) to the stretch axis. In the absence of stretching (0% elongation), the periodicity is 714 μm along both array axes. The maximum stretched period along the x-axis of 806 μm corresponds to a ~13% elongation of the device along the stretch axis. The lines represent linear least-squares fits to the data.

was reversibly deformable and the same AR wavelengths were measured upon stretching and subsequent contraction back to the original position. Further stretching caused a nonlinear change in the measured AR wavelength. We note that analogous tuning has been demonstrated using gold-based split ring resonators fabricated on a thick PDMS substrate [21].

3.4 Conclusion

In conclusion, we have presented the first experimental demonstration of plasmonics using liquid metals. To do so, we fabricated periodic arrays of subwavelength aperture arrays with EGaIn injected into an elastomeric PDMS mold, and measured the enhanced THz transmission properties of static arrays as well as arrays that were mechanically stretched. The latter measurements show the capability for mechanically tuned plasmonic devices and may allow for more complex three-dimensional plasmonic architectures. Since EGaIn flows at room temperature, we expect many of the sophisticated technologies developed for microfluidics and optofluidics [22] can be used to develop a broad range of active plasmonics capabilities. While the specific demonstration here relates to plasmonics, this approach can also be extended to develop active metamaterial devices. Although the measurements here were performed at THz frequencies, further studies of the dielectric properties of EGaIn may show that it can be used for plasmonic and metamaterial applications over a much broader spectral range.

3.5 References

1. W. L. Barnes, A. Dereux, and T. W. Ebbesen, "Surface plasmon subwavelength optics," Nature **424**, 824–830 (2003).

2. M. A. Ordal, L. L. Long, R. J. Bell, S. E. Bell, R. R. Bell, R. W. Alexander, Jr., and C. A. Ward, "Optical properties of the metals Al, Co, Cu, Au, Fe, Pb, Ni, Pd, Pt, Ag, Ti, and W in the infrared and far infrared," Appl. Opt. **22**, 1099–1119 (1983).

3. J. Gomez Rivas, C. Schotsch, P. Haring Bolivar, and H. Kurz, "Enhanced transmission of THz radiation through subwavelength holes," Phys. Rev. B **68**, 201306 (2003).

4. T. Matsui, Z. V. Vardeny, A. Agrawal, A. Nahata, and R. Menon, "Resonantly-enhanced transmission through a periodic array of subwavelength apertures in heavily-doped conducting polymer films," Appl. Phys. Lett. **88**, 071101 (2006).

5. L. Ju, B. Geng, J. Horng, C. Girit, M.C. Martin, Z. Hao, H.A. Bechtel, X. Liang, A. Zettl, Y.R. Shen, and F. Wang, "Graphene plasmonics for tunable terahertz metamaterials," Nature Nanotech. **6**, 630–634 (2011).

6. J. Gómez Rivas, P. H. Bolivar, and H. Kurz, "Thermal switching of the enhanced transmission of terahertz radiation through subwavelength apertures," Opt. Lett. **29**, 1680–1682 (2004).

7. D. C. Duffy, J. Cooper McDonald, O. J. A. Schueller, G. M. Whitesides, "Rapid prototyping of microfluidic systems in poly(dimethylsiloxane)," Anal. Chem. **70**, 4974–4984 (1998).

8. B. -H. Jo, L. M. Van Lerberghe, K. M. Motsegood, D. J. Beebe, "Three-dimensional micro-channel fabrication in polydimethylsiloxane(PDMS) elastomer," J. Microelectromechanical Systems **9**, 76–81 (2000).

9. M.D. Dickey, R.C. Chiechi, R.J. Larsen, E.A. Weiss, D.A. Weitz, G.M. Whitesides, "Eutectic Gallium-Indium (EGaIn): A liquid metal alloy for the formation of stable structures in microchannels at room temperature," Adv. Funct. Mater. **18**, 1097–1104 (2008).

10. J. –H. So, J. Thelen, A. Qusba, G. J. Hayes, G. Lazzi, M. D. Dickey, "Reversibly deformable and mechanically tunable fluidic antennas," Adv. Funct. Mater. **19**, 3632–3637 (2009).

11. T.W. Ebbesen, H.J. Lezec, H.F. Ghaemi, T. Thio and P. Wolff, "Extraordinary optical transmission through sub-wavelength hole arrays" Nature **391**, 667–669 (1998).

12. H. Cao and A. Nahata, "Resonantly enhanced transmission of terahertz radiation through a periodic array of subwavelength apertures," Opt. Express **12**, 1004–1010 (2004).

13. D. Grischkowsky, S. Keiding, M. van Exter and Ch. Fattinger, "Far-infrared time-domain spectroscopy with terahertz beams of dielectrics and semiconductors," J. Opt. Soc. Am. B **7**, 2006–2015 (1990).

14. F. Miyamaru and M. Hangyo, "Finite size effect of transmission property for metal hole arrays in subterahertz region," Appl. Phys. Lett. **84**, 2742–2744 (2004).

15. H. Yasuda and I. Hosako, "Measurement of terahertz refractive index of metal with terahertz time-domain spectroscopy," Jpn. J. Appl. Phys. **47**, 1632–1634 (2008).

16. M. A. Ordal, R. J. Bell, R. W. Alexander, Jr., L. L. Long, and M. R. Querry, "Optical properties of Au, Ni, and Pb at submillimeter wavelengths," Appl. Opt. **26**, 744–752 (1987).

17. A. Podzorov and G. Gallot, "Low-loss polymers for terahertz applications," Appl. Opt. **47**, 3254–3257 (2008)

18. A. Agrawal, Z. V. Vardeny, and A. Nahata, "Engineering the dielectric function of plasmonic lattices," Opt. Express **16**, 9601–9613 (2008).

19. T. Matsui, A. Agrawal, A. Nahata, and Z. V. Vardeny, "Transmission resonances through aperiodic arrays of subwavelength apertures," Nature **446**, 517–521 (2007).

20. A. Krishnan, T. Thio, T.J. Kim, H.J. Lezec, T.W. Ebbesen, P.A. Wolff, J. Pendry, L. Martin-Moreno, F.J. Garcia-Vidal, "Evanescently coupled resonance in surface plasmon enhanced transmission," Opt. Comm. **200**, 1–7 (2001).

22. I. M. Pryce, K. Aydin, Y. A. Kelaita, R. M. Briggs, and H. A. Atwater, "Highly stained compliant optical metamaerials with large frequency tenability," Nano Lett. **10**, 4222–4227 (2010).

23. Y. Fainman, L. Lee, D. Psaltis and C. Yang, *Optofluidics: Fundamentals, Devices, and Applications* (McGraw-Hill, 2010).

CHAPTER 4

RECONFIGURABLE PLASMONIC DEVICES USING LIQUID METALS

4.1 Introduction

The field of plasmonics offers unique capabilities for manipulating and controlling the propagation properties of electromagnetic radiation [1]. When metal films are appropriately structured, surface plasmon-polaritons (SPPs) can be excited from free-space radiation and propagate along metal-dielectric interfaces. A unique property of these excitations is that they exhibit dispersion properties that differ dramatically from that of free-space radiation, thereby enabling a broad range of new capabilities including subwavelength concentration of radiation [2,3], guided-wave propagation [4], enhanced extraction of light from photovoltaic devices [5], and optical filtering [6,7]. At present, much of this work has focused on passive demonstrations. However, there is great need for the development of active devices that can fulfill the required needs across the electromagnetic spectrum. In the THz spectral range, such needs are particularly acute, since workable device technologies are largely absent.

In recent years, there have been a number of studies describing active control of the propagation properties of SPPs using a variety of different techniques. The most common approach involves coupling SPPs into optically active materials, such as photochromic molecules [8], semiconductor device structures [9], and liquid crystals [10]. However, other approaches have been developed that involve the use of transient optical nonlinearities [11,12], application of an external magnetic field [13], and pre-defining the phase properties of the incident optical radiation [14]. Recently, we showed that by injecting eutectic gallium indium (EGaIn), a liquid metal at room temperature, into a polydimethylsiloxane (PDMS) mold, we could create a periodic array of subwavelength aperture that was mechanically flexible and reversibly deformable [15]. Thus, the

resonant frequencies could be tuned by mechanically stretching the device. In these demonstrations, the amplitude or frequency properties are typically tuned away from an equilibrium point via an external stimulus. However, it is not at all clear how the devices geometries in any of these implementations could be made reconfigurable.

In this submission, we demonstrate a technique that allows for reconfigurable changes in the geometry of a plasmonic device, corresponding to large-scale changes in the optical response. We used conventional microfluidic technology to create channels in an elastomeric mold, where EGaIn can be injected into or withdrawn from. As a specific example, we have fabricated a bullseye structure [16,17] in PDMS that is adhered to a gold (Au) coated metal foil that has a single subwavelength aperture. We measured the THz transmission properties as a function of the bullseye geometry, based upon which channels are filled with EGaIn. It should be noted that the present demonstration differs significantly from our earlier work with bullseye structures that were fabricated in free-standing stainless steel foils [18,19]. In those cases, the geometries were fixed. Based on the present measurements, we develop a simple model that accounts for the temporal properties of the observed waveforms. This model differs from what we have previously observed with bullseye devices fabricated in metal foils [18,19]. All of the measured data was performed using a single device in which different channels were filled with or emptied of EGaIn to obtain different geometries, demonstrating true reconfigurability. Results from different devices exhibited nearly identical results.

4.2 Experimental Detail

The basic component of a reconfigurable bullseye structure is a replica fabricated in PDMS. In order to create this replica, we first fabricated a bullseye structure in a 150 μm thick free-standing stainless steel foil using a simple chemical etching process. The structure consisted of a series of concentric rectangular cross-section annular grooves that were 600 μm wide and 100 μm deep with a periodic spacing of 1 mm. We then prepared a PDMS pre-polymer that was mixed with a curing agent using a weight ratio of 11:1. This pre-polymer was degassed, poured onto the stainless steel bullseye structure, and cured for 2 hours at 60 °C yielding a 500 μm thick film. Since PDMS does not adhere well to untreated metal surfaces, which results from the low surface energy of the elastomer, the replica could be peeled off the metal master easily. Cured PDMS films can be adhered to select materials after being treated with a high voltage corona. Unfortunately, this process does not work with most metals. Since the goal here is to use a metal substrate, an alternate procedure had to be used. In order to prepare the planar metal substrate, we initially used a free-standing planar 75 μm thick stainless steel foil with a single 490 μm diameter circular hole milled using a tripled Nd:YAG laser. This foil was then coated with a 10 nm thick Ti film, as an adhesion layer, and a 200 nm thick Au film. We then treated the Au layer with a monolayer of 3-mercaptopropyl trimethoxysilane (MPT). MPT creates a Au-Si bond on the metal surface that allows for preferential binding with PDMS. However, this approach still does not work well for cured PDMS surfaces. Therefore, we applied a thin layer of uncured PDMS (<10 μm) to the bottom layer (not within the channels) of the cured, corona treated PDMS replica. After curing the entire device for 2 hours at 60 °C, good adhesion between the

elastomeric bullseye structure and the Au coated metal foil was obtained.

As noted above, PDMS has a relatively low surface free energy (19.8 mN/m [20]). Therefore, when EGaIn is injected into a channel, the liquid metal does not adhere well to the PDMS sidewalls. However, it does adhere to the silanized Au surface. In order to minimize any liquid metal/Au or liquid metal/PDMS adhesion issues, which is necessary to reproducibly inject and withdraw EGaIn from a channel, we injected a fluorosilane solution (PFC504A-FS, Cytonix) into all of the channels and baked the device at 60 °C for an additional 2 hours. This reduced the surface free energy to ~6 mN/m on all four channel walls. In Figure 4.1(a), we show a schematic diagram of a final structure, where one channel is filled with EGaIn. The accompanying photograph in Figure 4.1(b) shows an actual device in which EGaIn has been injected into the third annular channel. A syringe with a 33 gauge needle (200 μm outer diameter, 89 μm inner diameter) was used to manually inject and withdraw the liquid metal.

We used conventional time-domain THz spectroscopy to characterize the bullseye structures and bare apertures. In this approach, the time-domain properties of a single cycle electromagnetic transient transmitted through a structure can be measured using coherent detection with subpicosecond temporal resolution. Photoconductive devices were used for both emission and coherent detection. An off-axis paraboloidal mirror was used to collect and collimate the THz radiation from the emitter to the devices. The THz beam, with a 1/e beam diameter of ~ 15 mm, was normally incident on the corrugated surface of the bullseye structures. It is important to note that the frequency content of the THz beam varies spatially, thus the temporal properties of the incident THz pulse are also spatially dependent.

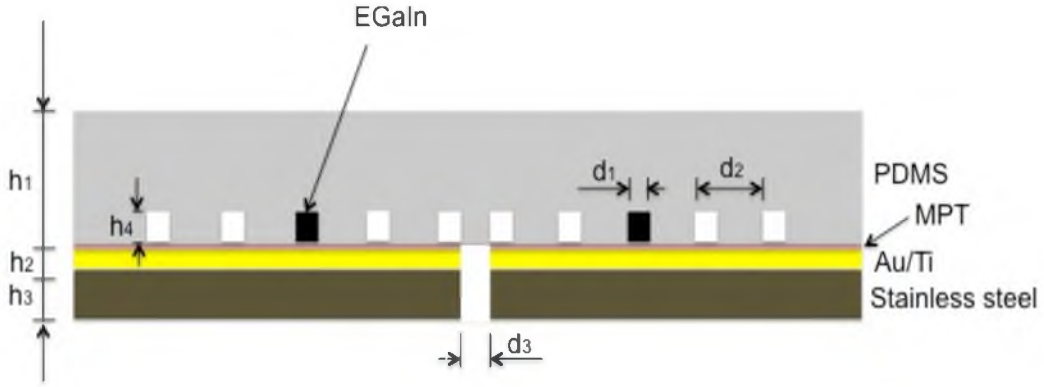

(a)

(b)

Figure 4.1. A bullseye device. (a) Schematic cross-section of the final bullseye device. The parameters for the device are d_1 =400 μm, d_2 = 1 mm and d_3 =490 μm. h_1 = 500 μm, h_2 = 250 nm, and h_3 = 75 μm, respectively. MPT is a silane that increases the adhesion between PDMS and the metal substrate. (b) Photograph of a bullseye pattern, in which EGaIn was injected into third annular channel.

4.3 Experimental Results and Discussion

In order to properly characterize the reconfigurable bullseye structures, we first measured the temporal properties of several different device structures to clarify the role of each component within the bullseye structure: (1) a single aperture in the metal foil without an attached PDMS mold, (2) a single aperture with an attached PDMS mold but without EGaIn, and (3) a single aperture with an attached PDMS mold and EGaIn injected into the second annular channel. The three corresponding waveforms are shown in Figure 4.2. The transmitted waveform for the single aperture without the PDMS replica is characterized by a single bipolar THz waveform. This waveform is similar to, though slightly narrower than, the incident THz waveform (not shown). The slight temporal narrowing arises from the fact that low frequency components within the incident THz beam that lie below the cutoff frequency of the circular aperture experience greater loss than higher frequencies. For a 490 μm diameter circular aperture, the corresponding cutoff frequency occurs at $\nu = 0.36$ THz. ($\lambda = 833$ μm). Since the metal foil is only 75 μm thick, the electric field is only slightly attenuated at frequencies below cutoff. This is consistent with earlier observations with single subwavelength apertures [18, 21]. It should be noted that in the absence of the aperture, there was no transmitted THz radiation.

For the single aperture with an attached PDMS mold and no EGaIn in any channel, there are two notable observations. First, we do not observe any apparent oscillations after the initial bipolar waveform. This demonstrates that the structured PDMS mold does not appreciably couple freely propagating THz pulses to SPPs by itself. Second, the observed bipolar waveform exhibits a smaller peak-to-peak amplitude and is broadened

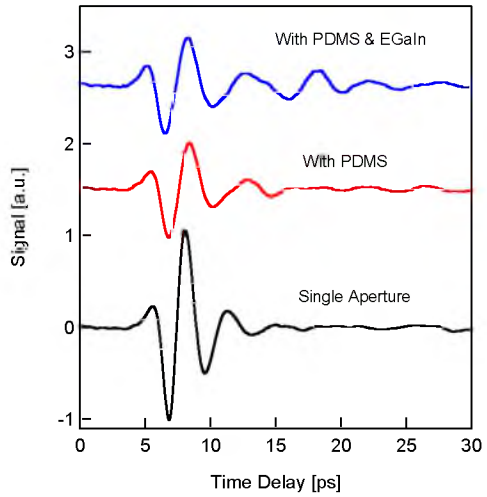

Figure 4.2. Measured time-domain waveforms for the single aperture without PDMS (black), single aperture with only the PDMS bullseye replica (red), and single aperture with EGaIn injected into the second annular channel of the PDMS bullseye structure (blue). The waveforms are vertically offset for clarity.

slightly in time relative to the waveform associated with the single aperture. This can be explained by considering the absorption properties of PDMS in the THz spectral range. We define a frequency dependent absorption coefficient, $\alpha(\nu) = 2\pi\nu n_i/c$ for the THz electric field, where the electric field decay is given by $\exp[-\alpha(\nu)d]$. Here, n_i is the imaginary component of the refractive index, c is the speed of light in vacuum, and ν is the THz frequency. We have previously found that the complex refractive index of PDMS in this spectral range is given approximately by $n = 1.57 + 0.04i$ and is relatively constant over the frequency range spanning 0.1 - 0.5 THz [15]. Therefore, in contrast to the aperture, which preferentially suppresses low frequencies, the PDMS layer preferentially suppresses high frequencies. Both the amplitude reduction and pulse broadening can be properly accounted for, if we consider absorption within the PDMS layer. In the discussion that follows, we will refer to this waveform as the 'reference.'

For the bullseye pattern with one annular channel filled with EGaIn, we observe the initial bipolar waveform followed by a single time-delayed oscillation. This waveform is similar in nature to that observed for a single subwavelength aperture surrounded by a single concentric groove [18]. This is reasonable given theoretical analyses showing that metallic protrusions on top of the surface of a metal film scatter (couple) SPPs with efficiencies similar to that of grooves [22]. In contrast to earlier time-domain measurements on bullseye structures [18,19], there are important differences dictating the temporal properties of the time-delayed oscillations here.

In order to elucidate these properties, we successively inject EGaIn into only one channel at a time, ensuring that all of the EGaIn has been withdrawn from the other channels. We then subtract the time-domain waveform associated with each resulting structure from that obtained the reference aperture. In Figure 4.3(a), we show the temporal waveform associated with the reference aperture, along with each of the subtracted waveforms. It is clear that as the distance between the filled annular channel and the central aperture increases linearly, the time delay between the initial bipolar waveform and the time-delayed oscillation also increases linearly. This is consistent with our earlier finding that there are two independent, yet phase-coherent, transmission processes that contribute to the transmitted time-domain waveform [18]: one component related to transmission directly through the subwavelength aperture and a time-delayed component associated with coupling of the free-space THz radiation to SPPs by the EGaIn annular ring. These coupled surface waves propagate towards and are sampled by the aperture. The extent of the sampling, corresponding in part to the magnitude of the observed time-delayed oscillation, is determined by the overlap between the spatial extent

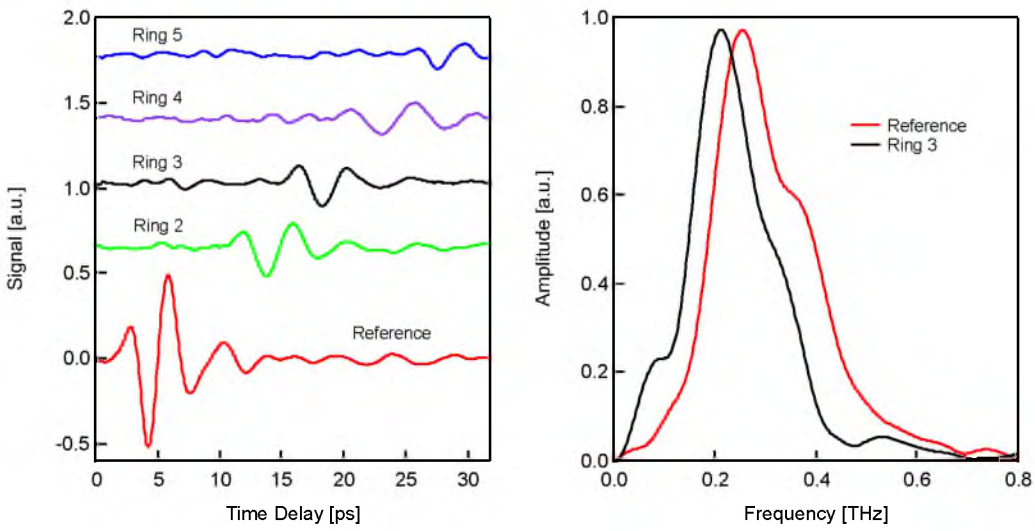

Figure 4.3. (a) Measured time-domain waveforms for reference aperture and contribution from each individual EGaIn filled channel (Ring 2 through Ring 5). The time-delayed oscillations were obtained by subtracting time-domain waveform of the reference aperture from the waveforms associated with structures in which successive single annular channels were filled. The waveforms are vertically offset for clarity. (b) The corresponding normalized amplitude spectra of the reference aperture (red) and the time-delayed oscillation from the Ring 3 structure (black).

of the SPP wave and the subwavelength aperture.

The measured time interval between successive oscillations (between Ring i and Ring i+1, for i=2-4 in Figure 4.3(a)) is ~4.5 ps. Analytically, we find that this time delay, Δt, is given by

$$\Delta t = \frac{n_{SPP1} d_1 + n_{SPP2}(d_2 - d_1)}{c}, \qquad (4.1)$$

where $n_{SPP1} \approx n_{air}=1$ in the unfilled channel, $n_{SPP2} \approx n_{PDMS}=1.57$ in the filled channel [15] and c is the speed of light in vacuum. Using Equation (4.1), we find that Δt=4.47 ps,

which agrees well with experimental results. It is worth noting that the fact that Equation (4.1) fit the experimental observations well is somewhat surprising. As we have previously shown, for the frequency range examined here, the out-of-plane 1/e spatial extent of SPPs is typically on the order of several mm [23]. Thus, for the unfilled channels, which are only ~100 μm high, it is not at all clear that we should be able to use a value of $n_{SPP1} \approx n_{air}=1$.

As with grooves fabricated into a metal foil, the EGaIn protrusions appear to also couple most of the incident THz to SPPs. To demonstrate this, in Figure 4.3(b) we show the amplitude spectra for initial bipolar pulse (reference aperture) and the oscillation associated with Ring 3. While the spectra differ slightly, it is important to note that the frequency content of THz beam varies spatially; therefore, the temporal properties of the incident THz pulse are also spatially dependent. In general, the THz beam has a frequency dependent beam diameter, with higher frequencies more closely concentrated near the beam axis.

Based on this insight, we are now in a position to fully exploit this capability to create reconfigurable bullseye devices of greater complexity by selectively injecting and withdrawing EGaIn into different channels to obtain the desired temporal response. In Figure 4.4, we show two sets of time-domain waveforms for three different bullseye geometries: (i) Rings 3 and 5 filled (ii) Rings 3-5 filled and (iii) Rings 2-5 filled. In each case, we show the experimentally measured waveform (blue) and the waveform (red) that has been reconstructed from the data in Figure 4.3(a). The waveform reconstruction was performed by taking a superposition of the time-domain waveform associated with the reference waveform and that of the relevant filled rings. However, in contrast to what we

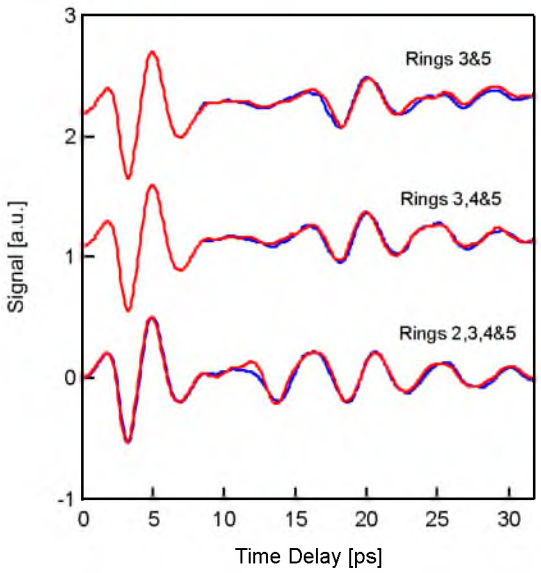

Figure 4.4. Measured and reconstructed time-domain waveforms for bullseye structures with multiple filled annular channels. The blue waveforms corresponds to experimentally measured time-domain waveforms, while the red waveforms are reconstructed by taking a superposition of the relevant components in Figure 4.3(a), with minor modifications, as described in the text. (top) Bullseye with Rings 3 and 5 filled with EGaIn (middle) Bullseye with Rings 3, 4, and 5 filled with EGaIn (bottom) Bullseye with Rings 2, 3, 4, and 5 filled with EGaIn. The waveforms are vertically offset for clarity.

have observed with stainless steel bullseye devices [18], the oscillations associated with a specific ring clearly change in timing and, to a lesser extent, amplitude depending upon which other rings are filled.

In order to explain why this happens, consider a bullseye structure in which only Ring 5 was filled with EGaIn. The resulting time-domain waveform can be reconstructed from the data in Figure 4.3(a) using the reference aperture and Ring 5 waveforms. Now, suppose that we also fill Ring 3 with EGaIn. In this case, the resulting time-domain waveform cannot simply be reconstructed from the waveforms corresponding to the reference aperture, Ring 3 and Ring 5. By virtue of filling Ring 3, the temporal properties of the oscillation corresponding to Ring 5 will change. The reason for this timing change

is because instead of having 4 sections of length d_1 with a refractive index of $n_{SPP1} \approx n_{air}=1$ and 4 sections of length (d_2-d_1) with a refractive index of $n_{SPP2} \approx n_{PDMS}=1.57$, by filling Ring 3, the oscillation arising from Ring 5 will now see 3 sections of length d_1 with a refractive index of $n_{SPP1} \approx n_{air}=1$, 1 section of length d_1 with a refractive index of $n_{SPP2} \approx n_{PDMS}=1.57$, and 4 sections of length (d_2-d_2) with a refractive index of $n_{SPP2} \approx n_{PDMS}=1.57$. Thus, the inclusion of a single filled annular channel closer to the aperture will push the temporal contribution from an outer filled channel to a larger time delay, $\Delta\tau = d_1 (n_{SPP1}-n_{SPP1}) / c = 0.76$ ps. As additional inner rings are filled with EGaIn, oscillations associated with outer filled rings will be pushed to slightly larger time delay values. These expected differences in timing match the experimental data well.

In addition to shifts in timing caused by filling empty inner channels, it is reasonable to assume that there would also be changes in the spectral content of the individual oscillations associated with the outer rings. Such changes would arise because of differences in the loss properties between SPP propagation along a metal-air interface and a metal-PDMS interface. However, changes in the temporal properties of outer ring generated oscillations are smaller than expected from the additional d_1 traversals through metal-PDMS sections as inner channels are filled.

4.4 Conclusion

In conclusion, we have demonstrated a means for creating reconfigurable plasmonic devices using liquid metals. As a specific example of this capability, we fabricated an elastomeric bullseye pattern using soft lithography and bonded it to a metal substrate after appropriate surface treatment of the metal. By injecting and withdrawing a liquid

metal, eutectic gallium indium, into or from individual channels, we are able to dramatically alter the geometry. We note that EGaIn can only be withdrawn from a channel when all four interior channels walls are coated with a fluorosilane, which dramatically reduces the free surface energy and inhibits EGaIn from sticking to the PDMS and metal surfaces. We developed a very simple description that accounts for the timing of all of the relevant time-domain oscillations. . While the present device requires manual operation to inject and withdraw the liquid metal, well-developed micro-electromechanical systems (MEMS) technology can be used to fabricated micro-actuators and micro-pumps directly on the same substrate to enable significantly higher speed reconfigurability [24]. As an example, a silicon-based magnetohydrodynamic pump has been shown to effectively actuate liquid metals [25]. Plasmonic devices, such as the one described here, could be fabricated on the same substrate, allowing for reconfigurability using appropriate electrical signals to drive the micro-pumps. Thus, this approach offers significant promise for developing active devices. Finally, we note that this general idea may be extended to develop active device that can operate in other regions of the electromagnetic spectrum. However, new challenges may arise. For example, as one moves to much shorter wavelengths, which requires smaller channel dimensions, use of syringes or micro-pump technology may not be viable to inject liquid metals, because significantly higher pressures may be needed to inject and withdraw liquid metals [26]. Thus, alternate approaches may need to be explored.

4.5 References

1. E. Ozbay, "Plasmoncis: merging photonics and electronics at nanoscale dimensions," Science **311**, 189–193 (2006).

2. A.J. Babadjanyan, N.L. Margaryan and K.V. Nerkararyan, "Superfocusing of surface polaritons in the conical structure," J. Appl. Phys. **87**, 3785–3788 (2000).

3. M. I. Stockman, "Nanofocusing of optical energy in tapered plasmonic waveguides," Phys. Rev. Lett. **93**, 137404 (2004).

4. T. W. Ebbesen, C. Genet and S. I. Bozhevolnyi, "Surface plasmon circuitry," Phys. Today **61**, 44–50 (2008).

5. H. A. Atwater and A. Polman, "Plasmonics for improved photovoltaics," Nature Mater. **9**, 205–213 (2010).

6. T. W. Ebbesen, H. J. Lezec, H.F. Ghaemi, T. Thio, and P. A. Wolff, "Extraordinary optical transmission through sub-wavelength hole arrays," Nature **391**, 667–669 (1998).

7. T. Matsui, A. Agrawal, A. Nahata, and Z. V. Vardeny, "Transmission resonances through aperiodic arrays of subwavelength apertures," Nature **446**, 517–521 (2007).

8. R. A. Pala, K. T. Shimizu, N. A. Melosh, and M. L. Brongersma, "A nonvolatile plasmonic switch employing photochromic molecules," Nano Lett. **8**, 1506–1510 (2008).

9. J. A. Dionne, K. Diest, L. A. Sweatlock, and H. A. Atwater, "PlasMOStor: A metal-oxide-Si field effect plasmonic modulator," Nano Lett. **9**, 897–902 (2009).

10. Y. J. Liu, Q. Hao, J. S. T. Smalley, J. Liou, I. C. Khoo, and T. J. Huang, "A frequency-addressed plasmonic switch based on dual-frequency liquid crystals," Appl. Phys. Lett. **97**, 091101 (2010).

11. K. F. McDonald, Z. L. Samson, M. I. Stockman and N. I. Zheludev, "Ultrafast active plasmonics," Nature Photon. **3**, 55–58 (2009).

12. G. A. Wurtz, R. Pollard, W. Hendren, G. P. Wiederrecht, D. J. Gosztola, V. A. Podolskiy and A. V. Zayats, "Designed ultrafast optical nonlinearity in a plasmonic nanorod metamaterial enhanced by nonlocality," Nat. Nanotech. **6**, 107–111(2011).

13. V. V. Temnov, G. Armelles, U. Woggon, D. Guzatov, A. Cebollada, A. Garcia-Martin, J.-M. Garcia-Martin, T. Thomay, A. Leitenstorfer, and R. Bratschitsch, "Active magneto-plasmonics in hybrid metal–ferromagnet structures," Nature Photon. **4**, 107–111 (2010).

14. B. Gjonaj, J. Aulbach, P. M. Johnson, A. P. Mosk, L. Kuipers, and A. Lagendijk, "Active spatial control of plasmonic fields," Nature Photon. **5**, 360–363 (2011).

15. J. Wang, S. Liu, Z. V. Vardeny, and A. Nahata, "Liquid metal-based plasmonics," Opt. Express **20**, 2346–2353 (2012).

16. T. Thio, K. M. Pellerin, R. A. Linke, H. J. Lezec, and T. W. Ebbesen, "Enhanced light transmission through a single subwavelength aperature," Opt. Lett. **26**, 1972–1974 (2001).

17. H. J. Lezec, A. Degiron, E. Devaux, R. A. Linke, L. Martin-Moreno, F. J. Garcia-Vidal, and T. W. Ebbesen, "Beaming light from a subwavelength aperture," Science **297**, 820–822 (2002).

18. A. Agrawal, H. Cao, and A. Nahata, "Time-domain analysis of enhanced transmission through a single subwavelength aperture," Opt. Express **13**, 3535–3542 (2005).

19. A. Agrawal, and A. Nahata, "Time-domain radiative properties of a single subwavelength aperture surrounded by an exit side surface corrugation," Opt. Express **14**, 1973–1981 (2006).

20. H. W. Fox, P. W. Taylor, and W. A. Zisman, "Polyorganosiloxanes…Surface active properties," Ind. Eng. Chem. **39**, 1401–1409 (1947).

21. O. Mitrofanov, M. Lee, J. P. W. Hsu, I. Brener, R. Harel, J. Federici, J. D. Wynn, L. N. Pfeiffer, and K. W. West, "Collection-mode near-field imaging with 0.5-THz pulses," IEEE J. Sel. Top. Quantum Electron. **7**, 600–607 (2001).

22. J. A. Sanchez-Gil, "Surface defect scattering of surface plasmon polaritons: Mirrors and light emitters," Appl. Phys. Lett. **73**, 2509–3511 (1998).

23. A. Nahata, and W. Zhu, "Electric field vector characterization of terahertz surface plasmons," Opt. Express **15**, 5616–5624 (2007).

24. N.-T. Nguyen and S. T. Werely, *Fundamentals and Applications of Microfluidics* (Artech House, 2006).

25. W. Irshad and D. Peroulis, "A silicon-based galinstan magnetohydrodynamic pump" in *Proceedings of the 9th International Workshop on Micro and Nanotechnology for Power Generation and Energy Conversion Applications* (PowerMEMS, 2009), pp. 127–129.

26. M. D. Dickey, R. C. Chiechi, R. J. Larsen, E. A. Weiss, D. A. Weitz, and G. M. Whitesides, "Eutectic gallium-indium (EGaIn): A liquid metal alloy for the formation of stable structures in microchennels at room temperature," Adv. Funct. Mater. **18**, 1097–1104 (2008).

CHAPTER 5

RECONFIGURABLE LIQUID METAL-BASED TERAHERTZ METAMATERIALS VIA SELECTIVE ERASURE AND REFILLING TO THE UNIT CELL LEVEL

5.1 Introduction

The development of metamaterials has attracted significant attention in recent years, because such materials can exhibit unique electromagnetic properties that are not readily available in nature [1]. This capability has been used in a variety of applications that hold great promise for next-generation devices, such as switches [2], efficient absorbers [3], phase modulators [4], and filters [5]. For many applications, the ability to tune the response to different discrete states in a controllable manner is highly desirable. Most existing methods to modify the response rely on changes in the various constituent materials via an external stimulus, often in the form of light [2], voltage [5,6], temperature [7,8], or mechanical flexing [9,10]. While these approaches are interesting, there are capabilities that they cannot address. The individual elements in metamaterials are typically defined lithographically using solid materials. Thus, they cannot easily be removed or reinserted, which would allow for different responses under different conditions. The individual unit cells also cannot easily be controlled individually. Typically, the application of an external stimulus causes all unit cells to react simultaneously and in the same manner. The ability to control individual unit cells independently is of significant potential importance, since it allows for the possibility of achieving a more complex electromagnetic response from a single device.

In this work, we demonstrate that eutectic gallium indium (EGaIn) [11,12], a liquid metal at room temperature, can be used to fabricate terahertz (THz) metamaterials in which individual unit cells or groups of unit cells can be selectively erased and subsequently refilled. With each change in the structure, either erasure or refilling, the corresponding transmission spectrum can be dramatically altered. The devices are formed

using a polydimethylsiloxane (PDMS) mold with embedded closed ring resonator (CRR) shaped channels that are connected via common inlet channels. PDMS is commonly used in a variety of microfluidic applications and has been used for liquid metal-based plasmonics in the THz spectral range [13,14]. Furthermore, it exhibits good gas permeability [15,16], which is important for the present application.

5.2 Results and Discussion

The channels are initially filled with EGaIn, which forms a thin oxide surface layer to provide mechanical stability to the fluid [11]. When the PDMS surface is exposed to hydrochloric acid (HCl, ACS reagent grade) in a localized manner, this oxide layer can be selectively dissolved [11,12] over well-defined cross-sectional areas. In the absence of an oxide surface layer, EGaIn has a viscosity that is twice that of water and a surface tension that is similar to mercury [11]. Thus, when EGaIn is exposed to HCl vapor in a localized manner, the liquid metal will retract to a position where a stable new oxide surface layer can form (i.e., there is no further exposure to HCl), corresponding effectively to erasure of the metal pattern in the exposed area. Complete reconfigurability of the metamaterial structure is accomplished by refilling liquid metals into unfilled microchannels to recover the initial structure.

We fabricated microchannels in PDMS using soft lithography techniques. To do so, we first fabricated the designed structure using SU8-3000 photoresist on a silicon wafer via conventional photolithographic techniques. The PDMS pre-polymer was mixed with a curing agent using a volume ratio of 7:1, degassed, poured onto the SU8 molds, and cured for 2 h at 60 °C. After curing, the inverse PDMS replicas were peeled off the molds

and sealed with another layer of flat PDMS using a high voltage corona. The flat PDMS layer covering the CRR metamaterial structure had a thickness of ~ 40 μm, yielding an overall device thickness of 740 μm. Finally, we injected EGaIn into the air voids of the PDMS structures to obtain the desired CRR metamaterials. Since PDMS is gas permeable, particularly through the thin planar PDMS section, the liquid metal could be injected into the channels without the use of an air outlet and yielded defect-free structures with no air bubbles.

We fabricated a metamaterial device composed of a 4 × 4 array of CRR clusters arranged in an alternating pattern. In Figure 5.1(a), we show a quarter of this overall device (i.e., a 2 × 2 array of the two different CRR clusters). The clusters were composed of either a 5 × 4 array of small CRRs connected to injection channels, where the rings had an inner diameter of d_1 = 136 μm, an outer diameter of d_2 = 172 μm, and a spatial periodicity of T = 230 μm or a 3 × 2 array of large CRRs connected to injection channels, where the rings had an inner diameter D_1 = 260 μm, an outer diameter D_2 =296 μm, and spatial periodicities of P_1 = 460 μm and P_2 = 400 μm. Each cluster, both small CRR and large CRR, covered an area of 1032 μm × 1274 μm. The entire metamaterial device covered an area of 4128 μm × 5096 μm. The thickness of the liquid metal lines was 11 μm, which was determined by the microchannel height.

The localized erasure process was accomplished using HCl acid that was dispensed from a 0.1- 10 μL Ultra G tip connected to a Brand® transfer pipette. A schematic diagram illustrating the basic process is shown in Figure 5.1(b). The pressure on the pipette was adjusted to ensure that the diameter of the HCl drop was no larger than the diameter of the pipette tip. The pipette could then be accurately positioned at any location

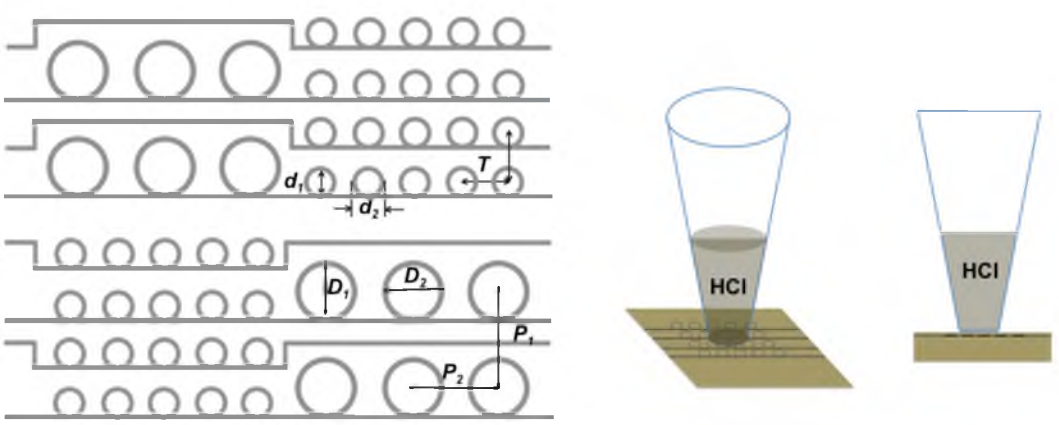

(a) (b)

Figure 5.1. (a) Schematic diagram of a section of the metamaterial device containing two CRR clusters in an alternating pattern: a 5 × 4 array of small CRRs and a 3 × 2 array of large CRRs. All the CRRs are connected to the horizontal injection channels. The smaller rings had an inner diameter of d_1=136 μm, an outer diameter of d_2=172 μm, while the large rings had an inner diameter D_1=260 μm, and outer diameter D_2=296 μm. (b) Schematic diagrams of isometric view (left) and side view (right) show the erasing process using HCl acid from a pipette tip. The tip is brought into soft contact with the surface of 40 μm thick planar PDMS section for 20-30 s.

above the device using a precision xy stage. In order to effect erasure, the pipette tip was placed in soft contact with the PDMS surface for 20 - 30 s, on the planar 40 μm thick elastomer side. Since, PDMS is gas permeable, erasure of the underlying liquid metal CRR structure occurred via HCl vapor penetrating through the 40 μm thick PDMS layer and dissolving the oxide layer covering the EGaIn, at which point the EGaIn would retract until a new configuration with a stable oxide layer could be maintained. We note that during the erasure process, the application of slight pressure on the pipette tip into the PDMS film helped accelerate the erasure. We believe that this faster reaction time arises from the fact that the effective thickness of the PDMS layer was reduced, allowing for faster interaction with the HCl vapor. During this erasure process, the excess EGaIn returned to the reservoir that was connected to the common inlet channels, but did not

refill any of the other unfilled CRR unit cells. The reason for the preferential return to the reservoir was because it presented a significantly larger cross-sectional opening than the CRRs and, thus, required less pressure to refill.

We used THz time-domain spectroscopy (THz-TDS) to measure the optical transmission spectra, t(ν), of the electric field through the CRR metamaterials, where ν is the THz frequency. The experimental setup has previously been described in detail[14]. All measurements were performed at normal incidence, with the THz electric field polarized perpendicular to the injection channels. The metamaterial device was mounted on a metal frame in which the opening size exposed only the CRR portion of the larger PDMS mold. The reference spectra were taken with a planar 740 μm thick PDMS film. It is important to note that since the oxide layer forms very quickly, the effect of that layer is present in all of the measurements. We also numerically simulated the response of the structure. The metal was modeled as a perfect electrical conductor using the device parameters given above, while the dielectric properties of PDMS were taken from THz refractive index measurements [13].

We begin by considering a device in which all of the channels have been fully filled with EGaIn. In Figures 5.2(a) and 5.2(b), we show a micrograph of the filled device as well as the measured transmission spectrum, respectively. The two prominent transmission resonances occur at 0.25 THz and 0.47 THz. The lower frequency resonance at 0.25 THz is associated with the fundamental resonance of the large CRRs, while the higher frequency resonance at 0.47 THz is associated with the fundamental resonance of the small CRRs. Both resonances arise from a coupled electric dipole resonance that is excited by a parallel THz electric field. In addition to the size of the CRRs, it is also well

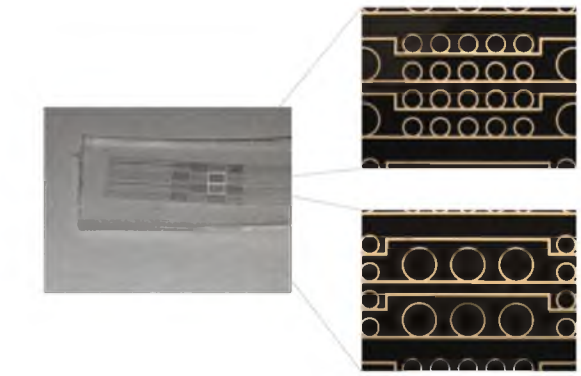

(a)

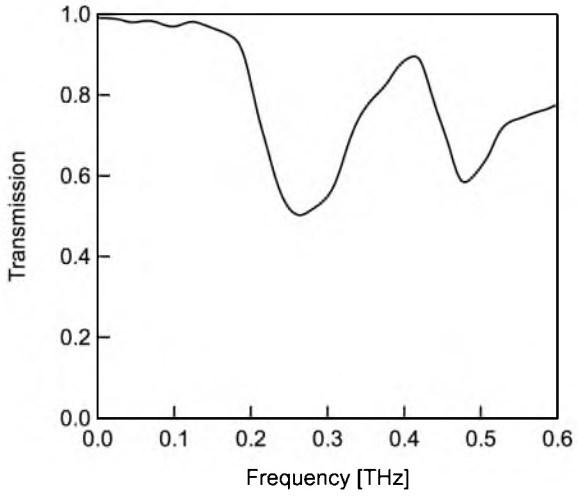

(b)

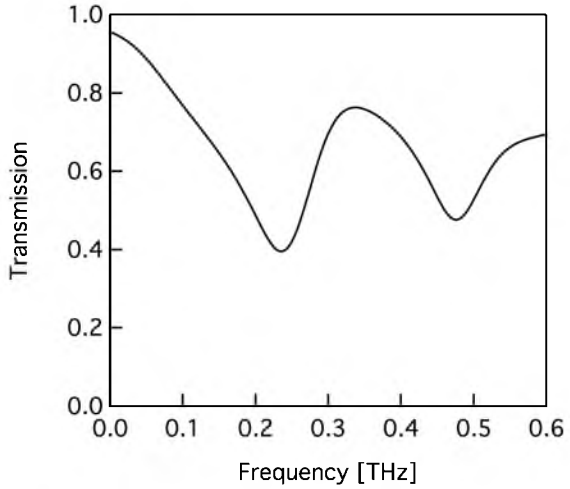

(c)

Figure 5.2. Properties of the EGaIn filled metamaterial device: (a) Image of a portion of the device in which all of the channels have been filled. (b) Measured transmission spectrum. (c) Numerically simulated transmission spectrum using the same geometrical parameters as in the device and measured THz refractive index properties of PDMS.

known that the lattice constant along the axis of the THz electric field polarization (perpendicular to injection channels) can also affect the resonant frequencies [17]. In contrast, the liquid metal present in the main injection channels appears to have little effect on the transmission spectrum. This is expected when the incident polarization is perpendicular to a set of straight metallic lines [6,18]. In addition, there are several smaller metallic lines connecting the injection channels of the different clusters that are parallel to the THz electric field, but the area that they cover is relatively small and appears to have little effect on the transmission spectrum. In Figure 5.2(c), we show the numerically simulated transmission spectrum, assuming the same excitation geometry as in the experiment. The agreement is good, in terms of both the resonant frequencies and resonant linewidths.

In order to demonstrate the reconfigurable nature of the device, we now demonstrate erasure of selected EGaIn structures. Using a HCl filled pipette that had an inner tip diameter of ~ 380 μm and an outer tip diameter of ~ 700 μm, we erased the large CRR clusters (3x2 elements each). Approximately four exposures were applied to erase each cluster. The erasure process was repeated until all 8 large CRR clusters were erased, leaving behind only the 8 small CRR clusters. A micrograph of a two erased clusters are shown in Figure 5.3(a). As is apparent in the image, the small CRRs remained unaffected, while the large CRRs were erased, leaving behind the empty large CRR microchannel structure in the image. The transmission spectrum associated with this structure, shown in Figure 5.3(b), demonstrates that the resonance at 0.25 THz has been eliminated, leaving only the high frequency resonance at 0.47 THz, associated with the small CRRs. The resonance linewidth here appears to be slightly larger than in Figure 5.2(b) and may be

Figure 5.3: Properties of the EGaIn filled metamaterial device with various elements erased and refilled. (a) Image of a portion of the metamaterial device with large CRRs erased. The surrounding small rings remained unaffected. (b) The corresponding transmission spectrum. (c) Image of a portion of the metamaterial device showing the large CRRs refilled with EGaIn. (d) The corresponding transmission spectrum. (e) Image of a portion of the metamaterial device with small CRRs erased. In this case, the surrounding large rings remained unaffected. (f) The corresponding transmission spectrum.

(c)

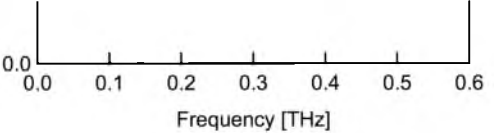
0.0
0.0
0.1
0.2
0.3
0.4
0.5
0.6
Frequency [THz]

(d)

(e)

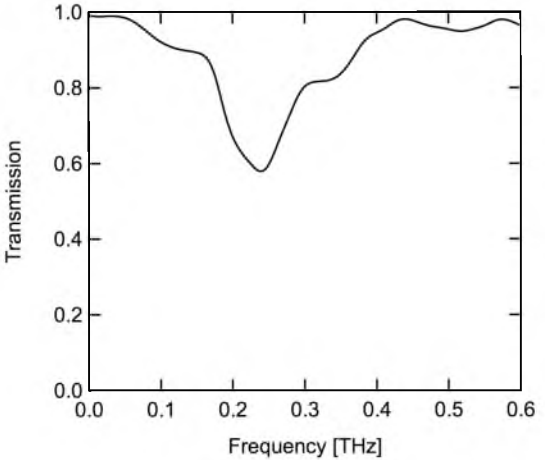
1.0
0.8
0.6
0.4
0.2
0.0
Transmission
0.0
0.1
0.2
0.3
0.4
0.5
0.6
Frequency [THz]

(f)

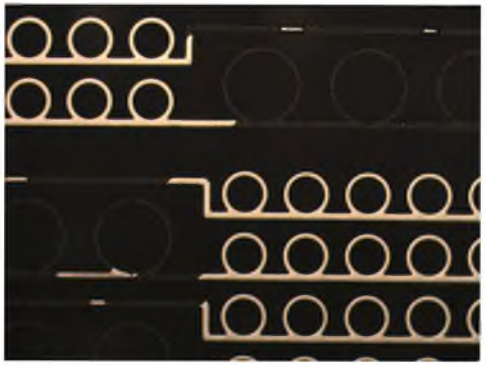

(a)

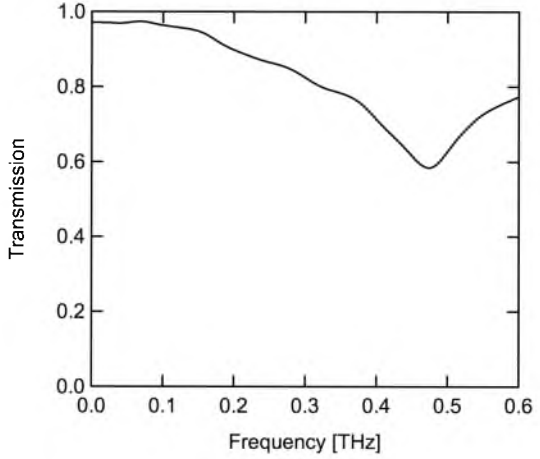
1.0
0.8
0.6
0.4
0.2
0.0
Transmission
0.0
0.1
0.2
0.3
0.4
0.5
0.6
Frequency [THz]

(b)

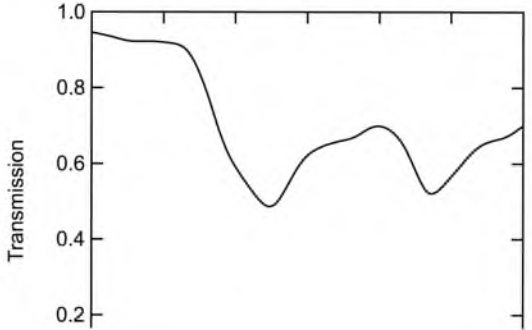
1.0
0.8
0.6
0.4
0.2
Transmission

due to variation in the experimental alignment and measurement.

The thickness of the planar section of PDMS layer that overcoats the EGaIn structures is critically important in determining the success of this process. As might be expected, thicker PDMS layers required longer exposure times and yielded less reproducible results. As an example, when the PDMS thickness was > 250 μm, we found that even when a 1 mm diameter drop of HCl acid was placed on the PDMS surface, the underlying CRRs could not be completely erased. For the small CRR clusters, only a few rings under the center of the drop were erased, even after the entire drop evaporated. Furthermore, the position of the rings that were erased was not predictable. If the acid was in contact with the PDMS surface for long periods of time (e.g. half an hour or longer) so that the underlying structures could be fully erased, the PDMS surface was often badly degraded.

The overall utility of this approach lies in the fact that the original device can be recovered by simply re-injecting EGaIn into the erased channels, as shown in Figure 5.3(c), yielding a structure that is nearly identical to the initial structure shown in Figure 5.2(a). The transmission spectrum for the completely filled metamaterial device after re-injection is shown in Figure 5.3(d). As can be seen, the two resonant frequencies at 0.25 THz and 0.47 THz were fully recovered, with relatively little difference between the spectra in Figures 5.2(b) and 5.3(d).

Once fully refilled, we then selectively erased all 8 small CRR clusters. A micrograph of an erased cluster is shown in Figure 5.3(e), and the corresponding transmission spectrum is shown in Figure 5.3(f). In contrast to what happens when the large CRR clusters were erased, the high frequency resonance at 0.47 THz disappeared. In principle,

this process of filling and erasing the CRR channels can be repeated multiple times. However, PDMS does degrade over time with repeated exposure to HCl. In the specific case of the 40 μm thick planar PDMS layer, we could only perform 2 cycles for the large CRR clusters and 4 cycles for small CRR clusters. Further optimization of the device parameters may allow for greater cycling of the process. We are currently exploring the use of electrochemical reactions that will dissolve the EGaIn, but will have minimal impact on the PDMS.

Finally, we address the issue of the minimum feature size that can be achieved using this process. In general, the smallest erasure area is limited by both the inner diameter of the pipette tip, which can limit the size of the HCl drop, and the thickness of the PDMS layer above the EGaIn structure, since the HCl vapor diffuses through the PDMS. The size of the pipette tip can limit the cross-sectional area of HCl present at the PDMS surface, but cannot easily limit the area in the PDMS that is exposed to the HCl vapor. This issue can be mitigated, to some extent, by using a thin PDMS layer to limit the spread of HCl vapor over the short propagation path. When using a pipette with a 0.1- 10 μL Ultra G tip, a minimum of 4 small CRRs were erased with a single exposure, corresponding to a cross-sectional area of ~400 μm × 400 μm.

It should be possible to obtain smaller erased areas by simply using pipettes with smaller tips. However, it was experimentally challenging to carefully control the HCl when such tips were used, making it difficult to obtain reproducible results. Therefore, we developed an alternate technique to erase individual small CRR elements. We polished the end of a BD® 31 gauge beveled needle, which has an outer diameter of 260 μm, so that the endface was not sharp and would not puncture PDMS. Using mechanical

pressure, we pressed the needle into the PDMS immediately above a CRR element for approximately 0.2 seconds. For the small CRR array with outer diameter of 126 μm and a spatial periodicity of 165 μm, this approach could be used to accurately erase EGaIn elements, as demonstrated in Figure 5.4, where we erased two nearby small CRR elements. Since only two elements were erased, there is relatively little difference in the resulting transmission spectrum. Nevertheless, for more complex geometries, such a technique may be useful for fine-tuning the transmission response.

5.3 Conclusion

In conclusion, we have demonstrated a technique for creating dramatic configuration changes in a device. This was accomplished via erasure and refilling of metamaterial unit cells in a geometry that utilized closed ring resonators of two different sizes. The primary erasure process involved the use of HCl to dissolve the surface oxide layer, causing the EGaIn to retract to a new position where a stable oxide layer can be formed. We also showed that relatively soft mechanical pressure could be used to erase individual unit

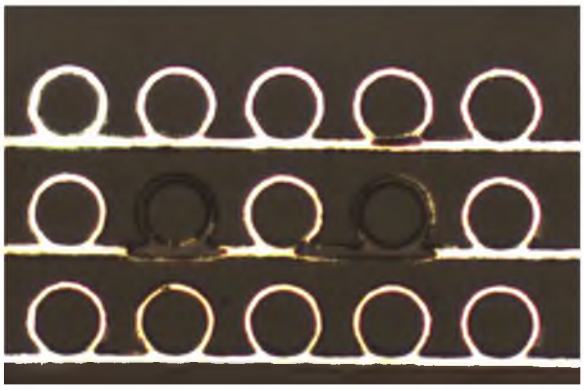

Figure 5.4. Image showing two nearby CRRs erased using mechanical pressure from a syringe needle.

cells. Both techniques could be utilized using the same basic pipette or needle, depending upon the number of unit cells that needed to be erased. In addition, the original device configuration could be recovered by re-injecting the liquid metal into all of the unfilled unit cells. The present approach does not allow for very fast reconfiguration of the device, since it involves large-scale material flow. However, this issue may be mitigated, to some extent, if only partial reversible changes are made to individual elements, allowing for a greater number of discrete configurations.

5.4 References

1. T. J. Yen, W. J. Padilla, N. Fang, D. C. Vier, D. R. Smith, J. B. Pendry, D. N. Basov, and X. Zhang, "Terahertz magnetic response from artificial materials," Science **303**, 1494–1496 (2004).

2. W. J. Padilla, A. J. Taylor, C. Highstrete, M. Lee, and R. D. Averitt, "Dynamical electric and magnetic metamaterial response at terahertz frequencies," Phys. Rev. Lett. **96**, 107401 (2006).

3. N.I. Landy, S. Sajuyigbe, J. J. Mock, D. R. Smith, and W. J. Padilla, "Perfect metamaterial absorber," Phys. Rev. Lett. **100**, 207402 (2008).

4. H.-T. Chen, W. J. Padilla, M. J. Cich, A. K. Azad, R. D. Averitt, and A. J. Taylor, "A metamaterial solid-state terahertz phase modulator," Nature Photon. **3**, 148–151 (2009).

5. Y.-S. Lin, Y. Qian, F. Ma, Z. Liu, P. Kropelnicki and C. Lee, "Development of stress-induced curved actuators for a tunable THZ filter based on double split-ring resonators," Appl. Phys. Lett. **102**, 111908 (2013).

6. H. T. Chen, W. J. Padilla, J. M. O. Zide, A. C. Gossard, A. J. Taylor, and R. D. Averitt, "Active terahertz metamaterial devices," Nature **444**, 597–600 (2006).

7. J. Gu, R. Singh, Z. Tian, W. Cao, Q. Xing, M. He, J. W. Zhang, J. Han, H.-T. Chen, and W. Zhang, "Terahertz superconductor metamaterial," Appl. Phys. Lett. **97**, 071102 (2010).

8. H. Tao, A. C. Strikwerda, K. Fan, W. J. Padilla, X. Zhang and R. D. Averitt, "Reconfigurable terahertz metamaterials," Phys. Rev. Lett. **103**,147401 (2009).

9. S. Aksu, M. Huang, A. Artar, A. A. Yanik, S. Selvarasah, M. R. Dokmeci, and H. Altug, "Flexible plasmonics on unconventional and nonplanar substrates," Adv. Mater. **23**, 4422–4430 (2011).

10. A. Q. Liu, W. M. Zhu, D. P. Tsai and N. I. Zheludev, "Micromachined tunable metamaterials: a review," J. Opt. **14**, 114009 (2012).

11. M. D. Dickey, R. C. Chiechi, R. J. Larsen, E. A. Weiss, D. A. Weitz, and G. M. Whitesides, "Eutectic gallium-indium (EGaIn): a liquid metal alloy for the formation of stable structures in microchannels at room temperature," Adv. Funct. Mater. **18**, 1097–1104 (2008).

12. Q. Xu, N. Oudalov, Q. Guo, H. M. Jaeger, and E. Brown, "Effect of oxidation on the metamaterial properties of liquid gallium and eutectic gallium-indium," Phys. Fluids, **24**, 063101 (2012)

13. J. Wang, S. Liu, Z. V. Vardeny, and A. Nahata, "Liquid metal-based plasmonics," Opt. Express **20**, 2346–2353 (2012).

14. J. Wang, S. Liu, and A. Nahata, "Reconfigurable plasmonic devices using liquid metals," Opt. Express **20**, 12119–12126 (2012).

15. T. C. Merkel, V. I. Bondar, K. Nagai, B. D. Freeman, and I. J. Pinnau, "Gas sorption, diffusion, and permeation in poly(dimethylsiloxane)," Polym. Sci. B Polym. Phys. **38**, 415–434 (2000).

16. A. Singh, B. D. Freeman, and I. Pinnau, "Pure and mixed gas acetone/nitrogen permeation properties of polydimethylsiloxane [PDMS]," J. Polym. Sci. B Polym. Phys. **36**, 289–301 (1998).

17. W. M. Zhu, A. Q. Liu, W. Zhang, J. F. Tao, T. Bourouina, J. H. Teng, X. H. Zhang, Q. Y. Wu, H. Tanoto, H. C. Guo, G. Q. Lo, and D. L. Kwong, "Polarization dependent state to polarization independent state change in THz metamaterials," Appl. Phys. Lett. **99**, 221102 (2011)

18. J. B. Pendry, A. J. Holden, W. J. Stewart, and I. Youngs, "Extremely low frequency plasmons in metallic mesostructures," Phys. Rev. Lett. **76**, 4773 (1996).

CHAPTER 6

ELECTROLYTIC REDUCTION OF LIQUID METAL OXIDES AND ITS APPLICATION TO RECONFIGURABLE STRUCTURED DEVICES

Jinqi Wang, Kanagasundar Appusamy, Sivaraman Guruswamy, and Ajay Nahata, "Electrolytic Reduction of Liquid Metal Oxides and Its Application to Reconfigurable Structured Devices," Scientific Reports **5**, 8637 (2015).

6.1 Introduction

The ability to modify the configuration of a given device geometry is of great importance in a broad range of applications. As an example, in the field of metamaterials, it is the specific geometry that gives rise to the response [1,2]. In order to have in-situ flexibility in determining the device properties, it would be advantageous to be able to make changes to the geometry in a controlled, reversible manner via the application of a simple external stimulus. Typically, devices that incorporate a structured metallic pattern are fabricated by depositing and patterning thin layers of conventional metal films, such as gold, silver or aluminum. However, such an approach does not lend itself easily to enabling large-scale changes in the structure; in the case of metamaterials, structures that incorporate semiconductors [3] or phase-change media [4,5] have been shown to allow for small-scale changes in the geometry when exposed to an external stimulus.

One approach that is amenable to allowing for large-scale changes in the structure geometry involves the use of liquid metals. The most commonly used member of this family of materials, eutectic gallium indium (EGaIn), is composed of 78.6% Ga and 21.4% In by weight and has a melting point of ~15.5 °C, making it liquid at room temperature. EGaIn forms a thin passivating oxide layer that enables the metal to form in non-spherical shapes [6] and is non-toxic [7]. These two properties make the material particularly useful for a variety of stretchable devices, including antennas [8], plasmonic devices [9], fibers [10], solar cells [11] and 2D and 3D self-healing wires [12]. In the absence of this oxide layer, EGaIn behaves like mercury and contracts into a spherical shape, since both materials exhibit high surface tension [7]. In fact, we have recently shown that when metamaterials fabricated using EGaIn inside a polydimethylsiloxane

(PDMS) microfluidic structure are exposed to an acid environment, the oxide layer is dissolved and the resulting bare liquid metal retracts away from the exposed area, effectively erasing the affected area [13]. In that case, we used HCl that was brought into contact with the PDMS surface and the embedded liquid metal oxide was etched away because of the porous nature of the elastomeric mold. While the approach was successful in erasing components of the liquid metal geometry, it suffered from several limitations: (i) the size of the HCl drop on the PDMS surface limited the minimum dimensions of the erased area (ii) the HCl exposure time varied depending upon the thickness and porosity of the PDMS layer (iii) the erased area was dependent on the thickness of the PDMS layer and (iv) repeated exposure to HCl degraded the elastomer, thereby limiting the number of erase/refill cycles that could be performed.

In this submission, we demonstrate that an electrolytic process can be used to change the geometry of a liquid metal-based structured device in a more localized and controlled manner. To accomplish this, we fabricate a device that incorporates lithographically defined electrodes and two different sets of microfluidic channels within an elastomeric PDMS mold fabricated using conventional soft lithography techniques. We fill one set of channels with EGaIn, forming an array of closed rings. The second set of channels is filled with water, either deionized or as a dilute saline solution, and is in contact with both the liquid metal and the electrodes. By applying a voltage between different electrodes, we create a highly localized reducing environment around the EGaIn channel region closest to the positive electrode, which dissolves the oxide layer in a controllable, reproducible manner. This EGaIn region effectively serves as the cathode. When the external voltage is removed, the electrolytic process ends abruptly. This approach can be

used to erase only portions of individual close rings or it can be performed in parallel to simultaneously etch multiple rings, each at a different rate and in a selective manner (i.e., each ring can be individually addressed). After etching, the entire device can be refilled with EGaIn, effectively allowing for a complete reset of the device. Since the localized electrolytic cell volume is small and the voltage applied for only short periods of time, the process can be cycled without any noticeable degradation to the PDMS structure. The approach is sufficiently general that it can be applied to a wide variety of other geometries and applications, including reconfigurable antennas and electrical circuits.

6.2 Results and Discussion

In order to explain how electrolysis can be used to create reconfigurable structured devices, we first discuss how the electrochemical process can be used to dissolve the oxide layer that forms on EGaIn. As noted above, when the oxide is etched, the exposed EGaIn quickly retracts to a position where a stable new oxide layer can form (i.e., a position where the extent of the reducing environment created is insufficient to remove/etch the oxide layer), corresponding effectively to erasure of the metal pattern in the exposed area [13]. In Figure 6.1, we show a schematic diagram of the approach used to measure the erasure rate of the liquid metal. A drop of EGaIn was placed on a clean glass slide and spread using the sharp edge of a second glass slide until a thin shiny film was formed. While the approach yielded a liquid metal film that had non-uniform thickness, the etching process only applied to the oxide layer that was expected to have a uniform thickness [14]. We then covered the metal film and the rest of the glass slide with a layer of water that contained different concentrations of NaCl. Two gold-coated

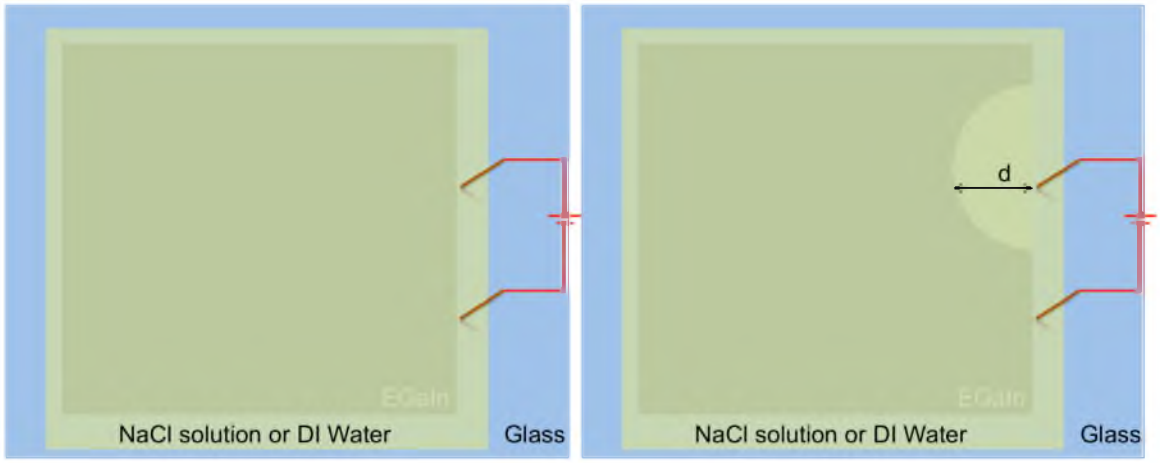

(a) (b)

Figure 6.1. Schematic diagram of the geometry used for measuring the electrolytic process. (a) Geometry before the application of an external voltage. (b) Geometry of the etched liquid metal after application of an external voltage showing the distance d used to measure the erasure rate. The upper electrode serves as the anode.

copper electrodes, separated by 2 cm, were then placed in contact with the water layer and close to one edge of the metal film. With the application of an external voltage, EGaIn was only erased about the anode (i.e., the gold-coated copper electrode to which the positive voltage was applied), with no change in the liquid metal around the other gold-coated copper electrode. Furthermore, the erasure configuration was found to not be symmetric about the anode (i.e., not a semi-circle centered at the anode), but rather somewhat closer to a semi-oval with a center that was offset from the positive electrode, as shown schematically in Figure 6.1.

To quantify the erasure process, we took videos of the erasure process and defined the erasure rate as the distance, d (as shown in Figure 6.1), erased per unit time after application of an external voltage. For each solution and each voltage setting, we performed multiple measurements with fresh samples to ensure reproducibility in the

data. In Figures 6.2(a) – 6.2(c), we show the erasure rate for saline solutions containing three different NaCl concentrations for multiple voltages. In general, a larger applied voltage yielded a faster erasure speed. This is reasonable, since a higher voltage corresponds to higher current, which is expected to accelerate the electrolytic process. For very low NaCl concentrations, ~0.001 g/ml, the erasure rate appeared to vary approximately linearly with the applied voltage. However, for higher NaCl concentrations, the rate became increasingly nonlinear. Once the voltage was removed, the erasure process stopped almost immediately.

Although saline solutions can yield very fast erasure rates, use of the electrolyte also creates several significant challenges. First, as water in the channels evaporates, the salt concentration increases. Thus, the erasure rate changes over time. Furthermore, the channels need to be flushed regularly to prevent crystallization of NaCl on the channel walls as the water evaporates, which severely degrades the device performance. To avoid these issues, we tested the erasure process using only deionized (DI) water, with a resistivity of ~18 MΩ•cm and the same experimental configuration shown in Figure 6.1. The erasure rate, shown in Figure 6.2(d), was significantly lower than for any concentration of saline solution tested. The erasure rate, shown in Figure 6.2(d), was significantly lower than for any concentration of saline solution tested. The test configuration in Figure 6.1, where the electrodes are close to one edge of the EGaIn film, is very close to the one that we adopt for the devices described below. To visually compare the erasure rates using DI water and saline solutions, we show time-stepped snapshots captured from videos taken of the erasure process in Figures 6.3(a) and 6.3(b). In both cases, the anode electrode was placed in the middle of the EGaIn film.

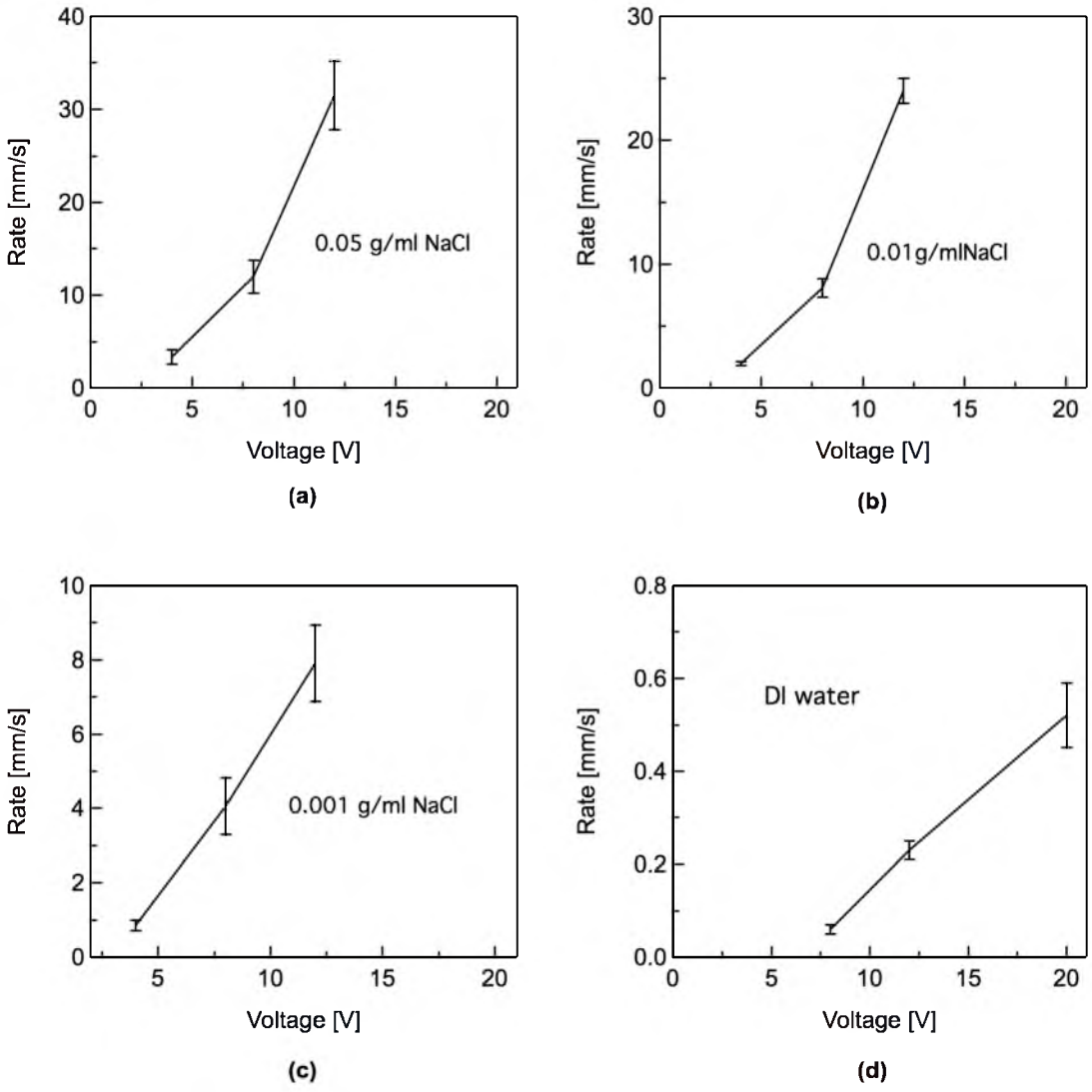

Figure 6.2. Erasure rates of EGaIn film using water with differing concentrations of NaCl. (a) 0.05 g/ml NaCl, (b) 0.01 g/ml NaCl, (b), 0.001 g/ml NaCl, and (d) deionized water.

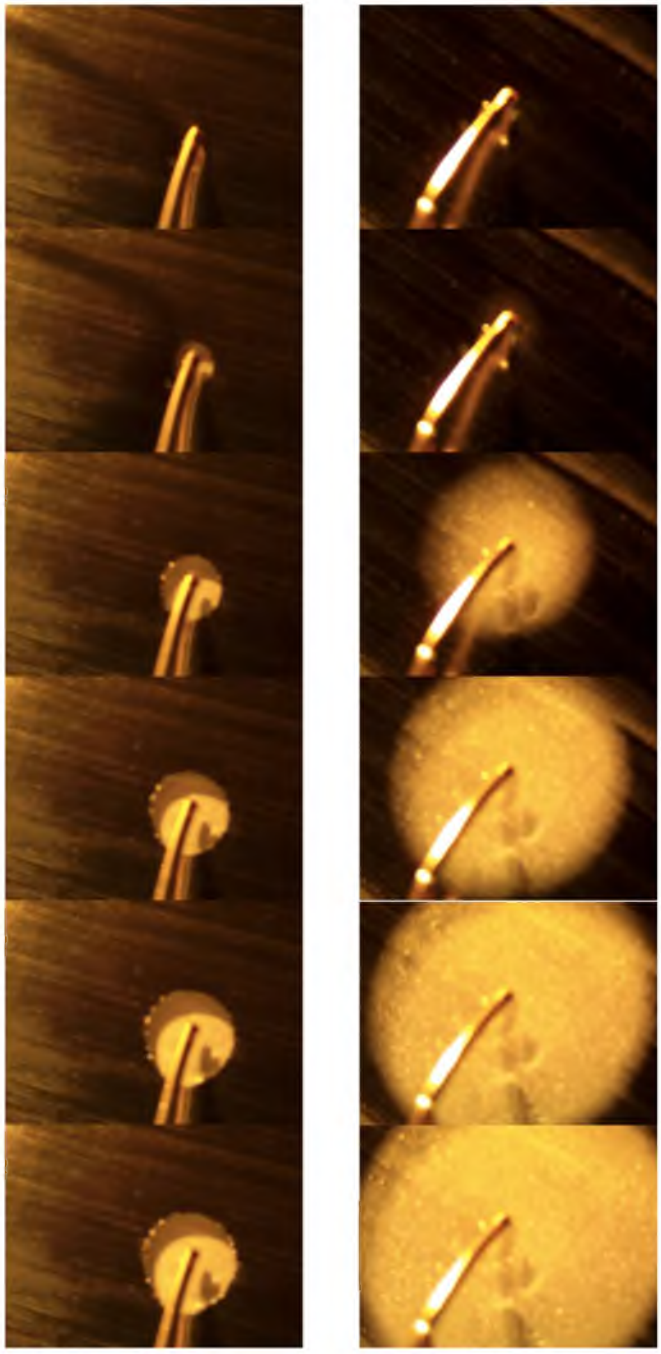

(a) **(b)**

Figure 6.3. Snapshots from videos taken of the EGaIn erasure process using DI water and a saline solution. (a) Snapshots using DI water. The time interval between each snapshot is ~ 3 seconds. (b) Snapshots using a 0.001 g/ml NaCl solution. The time interval between each snapshot is ~ 350 milliseconds. In both cases, the anode was placed in the middle of the liquid metal film and the cathode was placed at the periphery of the film in the aqueous solution.

The time interval between consecutive snapshots is ~ 3 seconds in Figure 6.3(a) and ~ 350 milliseconds in Figure 6.3(b), confirming the dramatic differences in oxide etch rates.

To describe the etching process, we first discuss the properties of the oxide film. Cademartiri and co-workers used x-ray photoelectron spectroscopy (XPS) and its variants to study the composition of this heterogeneous film [14]. Using XPS, they found signatures of three different types of oxide within the thin surface covering of the liquid metal: Ga_2O_3, Ga_2O, and In_2O_3, with Ga_2O_3 forming the dominant component. Using angle resolved XPS, they found that on average, the Ga_2O_3 formed the outer surface of the oxide. In the present work, in the absence of an applied potential, we would expect similar oxide formation when EGaIn comes into contact with either oxygen or water (pH ~7). We note that while the addition of NaCl changes the conductivity of the water, it does not alter the pH, so the following results and discussion apply to all of the experimental implementations discussed here.

When EGaIn or any other metal is immersed in a solution (DI water or a saline solution), an electrified interface is formed due to the electron transfer across the interface associated with the corresponding electrochemical reaction, and the establishment of a electrical double layer [15]. The electron transfer accompanying the reaction at the electrode/solution interface leads to the development of a potential difference between the electrode and solution across the double layer. An equilibrium is established when the net electron transfer is zero or the oxidation and reduction rate at this interface is equal. The potential of the electrode under this equilibrium condition is measured against a non-polarizable reference electrode (a standard hydrogen electrode

whose potential is taken as zero) and this potential is referred to as the equilibrium potential of EGaIn corresponding to this solution [15,16]. When the potential of the electrode deviates from this equilibrium value (due to an externally applied voltage or contact with another metal/material immersed in the same solution), the deviation is referred to as an overvoltage. An oxidation reaction occurs when the overvoltage is positive, in which case the electrode is referred to as the anode. Conversely, a reduction reaction occurs when this potential deviation is negative, in which case the electrode is referred to as a cathode. An electrochemical cell contains two half cells, one containing the anode and the other containing the cathode. The total cell voltage consists of the potential drop from the anode to the solution across the electrified double layer, the potential drop in the electrolyte between the electrodes, and the potential drop from the solution to the cathode across the electrified double layer. With the device configuration described here, the resistivity of the DI water and any of the NaCl solutions are high relative to EGaIn. Thus, the system can be modeled as consisting of two complementary electrochemical cells as shown in Figure 6.4. In cell 1, the Au electrode at positive voltage serves as the anode and the EGaIn in the adjacent channel serves as the cathode. Both DI water and NaCl solutions have a pH value of about 7. Thus, at this pH level, the equilibrium potential E_0 for Ga_2O_3 reduction reaction is = - 0.452 - 0.0591×pH = - 0.865 V. Similarly, the equilibrium potential E_0 for In_2O_3 reduction reaction is = - 0.181 - 0.0591×pH = - 0.594 V, again at a pH of 7. As the applied voltage is increased, the EGaIn electrode overvoltages corresponding to Ga_2O_3 and In_2O_3 reduction reactions in Cell 1 becomes increasingly negative and the reduction rate increases. Considering the presence of both Ga_2O_3 and In_2O_3 phases in the oxide layer on EGaIn, the oxide film

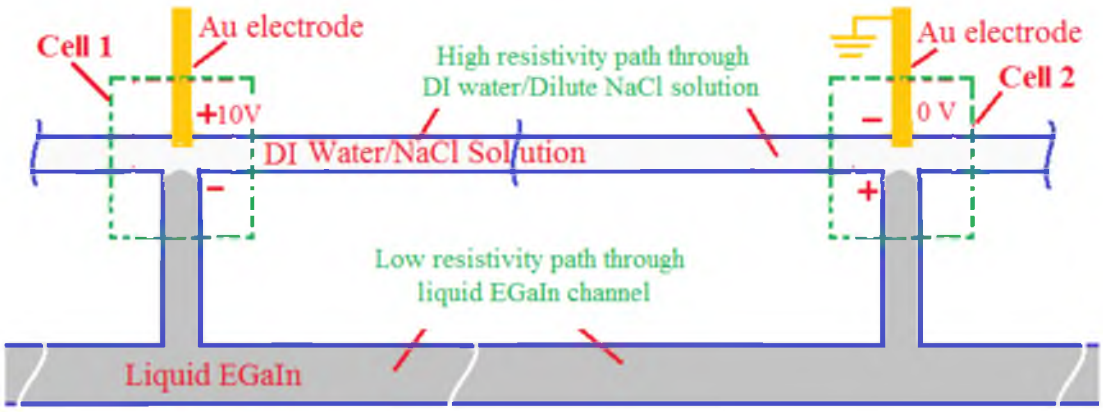

Figure 6.4. Schematic diagram of a representative electrochemical cell configuration for selective oxide removal. This specific geometry shown here has been chosen since it is relevant to the later discussion on a structured device. See the text for details.

reduction reactions at the EGaIn electrode (cathode) can be written as [17]

$$Ga_2O_3 + 6\,H^+ + 6\,e^- \rightarrow 2\,Ga + 3\,H_2O$$

$$In_2O_3 + 6\,H^+ + 6\,e^- \rightarrow 2\,In + 3\,H_2O$$

When the electrode potential is lower than the equilibrium potential, a reduction of the oxide film will occur. In addition, as the NaCl concentration is increased, there is a corresponding increase in the ionic strength and ionic conductivity. Thus, as the concentration increases, the potential drop in the solution across the two electrodes decreases further and is accompanied by corresponding increases in the anodic and cathodic overvoltages. The cell current values will increase exponentially with overvoltage and there will be corresponding increases in the oxide reduction rates. It is important to note that the negative overvoltages required for the reduction to metallic Ga and In are much smaller than the cell voltages applied. The need for such large applied

voltages was necessitated by the large potential drops in the solution due to the relatively high resisivities of DI water and the different dilute NaCl solutions. These various effects are reflected in the observed erasure rates of the Ga oxide shown in Figure 6.2 (a-d).

The highly controllable erasure of EGaIn using electrolysis of water makes this an attractive approach for creating reconfigurable artificially structured devices. While almost any geometry can be used to demonstrate the utility of this approach, we have decided to create two separate arrays of close rings embedded within a PDMS mold. The curved nature of the rings shows clearly that the approach is not limited only to straight channels and can therefore be applied to a broad range of potential applications. The basic fabrication process relied on creating a master with the designed microfluidic channels using SU-8 photoresist, which was then transferred to PDMS using standard soft lithography techniques [18]. A microscopic image of one unit cell of the SU-8 structure is shown in Figure 6.5(a). The lower horizontal channel and the ring structure were designed for the liquid metal. The upper horizontal channel and the short vertical channel above each ring were designed for DI water. With the exception of this short vertical channel above each ring, which had a height of 10 μm, all of the other channels were 32 μm in height. The 10 μm high short vertical channels were designed to have a smaller height because the pressure required to inject EGaIn into a microchannel varies inversely with its dimensions [7,19]. By having a smaller channel, the liquid metal was constrained to only the lower horizontal channel and the rings. On the other hand, since the surface tension of water is ~ 0.07 N/m, which is a much smaller value than for EGaIn, water easily filled the upper horizontal channel and the short vertical channels. The

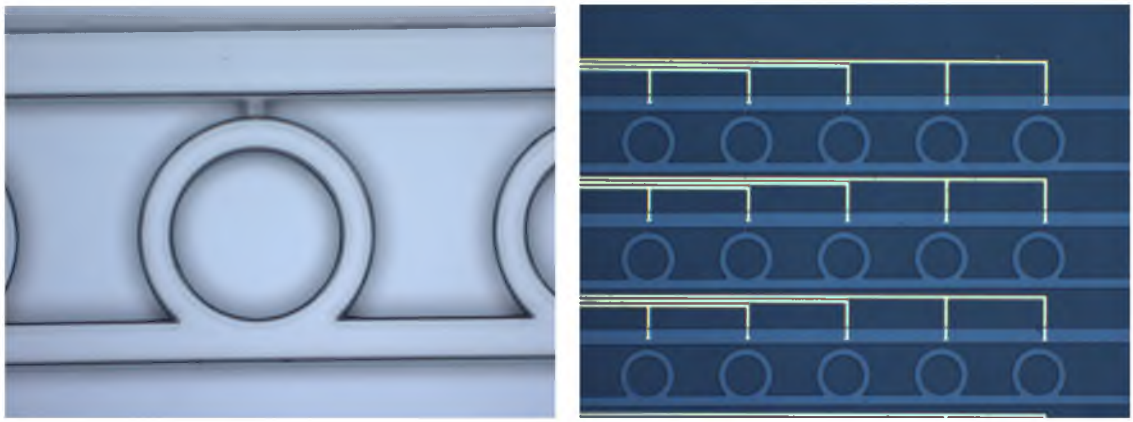

(a) (b)

Figure 6.5. Images of the master and fabricated device. (a) Microscope image of a portion of SU-8 mold. The inner radius of the circular ring is 100 μm. The outer radius of the circular ring is 130 μm. The length of the vertical short channel is 20 μm. The width of upper horizontal channel is 72 μm. The width of the lower straight channel is 44 μm. The vertical periodicity in the unit cells is 450 μm, while the horizontal periodicity is 530 μm. (b) Microscope image of a portion of final device before injecting any liquids. The yellow lines are the Au electrodes.

microscopic image of a portion of the device before injecting EGaIn and solution is shown in Figure 6.5(b).

To demonstrate the erasure process, we first injected EGaIn to fill all of the rings and lower horizontal channels. Then we injected DI water into the top horizontal channels, as well as the upper short vertical channels. In Figures 6.6(a) and 6.6(b), we show snapshots of the erasure process before and after application of an external voltage. To demonstrate this, we applied 10 V to two separated electrodes in the center row. A single protruding electrode (second from the left) within the observation window acted as the anode, while the cathode was outside of this window. The ring adjacent to the anode can be erased quickly. We note that because of the electrode geometry, electrochemical reactions are possible, though strongly suppressed, in adjacent unit cells. Further optimization of the water microchannel and gold electrode geometries is expected to mitigate this issue.

(a)

(b)

(c)

Figure 6.6. Snapshots of the erasure process within the CRR array. (a) A snapshot taken from a video before re-erasure of an EGaIn ring (after cycling between erasure and refilling several times). (b) Snapshot taken after erasure of the middle EGaIn ring. A potential voltage of +10 V was applied to the Au electrode immediately above the CRR. The ground voltage was applied to an electrode well outside of the viewing window. (c) The snapshot after refill EGaIn back to microchannels.

Once the applied voltage is removed, the erasure process stops quickly, providing excellent control over the fraction of each ring that is erased. Since the electrolytic reduction of the oxide is highly localized and operates for only short periods of time, we found that there was no observable damage to the PDMS, even with repeated cycling. After selective erasure, EGaIn can be refilled into microchannels to recover its original structure, as shown in Figure 6.6(c), to achieve full reconfigurability.

Finally, we note that since EGaIn rings can be electrochemically erased via the application of a localized external bias, the erasure process can be performed in either serial or parallel, to a single ring or to a group of rings in a random access manner. In Figure 6.7, we show the result of a multi-step process in which multiple rings in a larger ring array are erased. In each step, we selectively erased one or several rings, although this could all be done in a single step. The erased fraction of each ring that is erased is determined by the both the applied voltage and the application time in each step. In contrast to earlier work, where large-scale structural changes lead dramatic spectral changes, each individual erasure step here corresponded only to small geometry changes with correspondingly small changes in the transmission spectrum. The specific geometry enables a specific electromagnetic capability. Since the transmission properties of similar change induced here is designed to show the extent of the changes possible and not to geometries using liquid metals have been shown in earlier work [13,19], we have not shown spectral properties of these structures here. However, we expect them to be similar in nature.

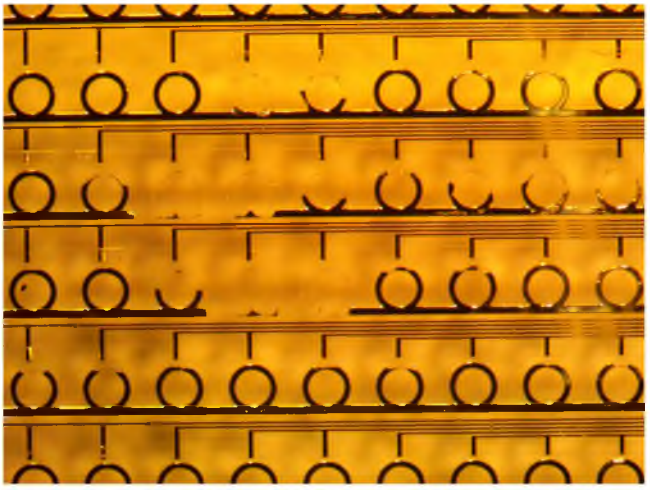

(a)

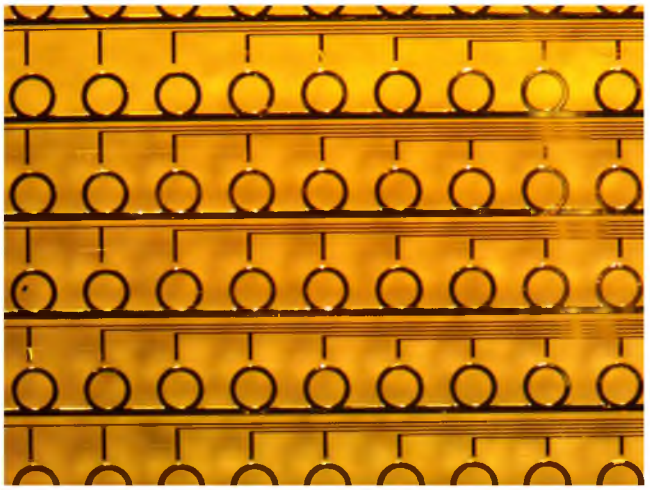

(b)

Figure 6.7. Snapshots of a video recording erasure of an array with random access. By controlling which electrodes have an applied voltage, the magnitude of that voltage, and the application time, we can selectively erase one ring or a group of rings simultaneously, with the possibility of each ring being etched to a different extent. (a) Starting with a completely filled array, a voltage of +10 V was applied to the gold electrodes adjacent to the different rings for different amounts of time. If we consider the third complete row of rings, the voltage was applied to the third ring from the left for only half the time that it was applied to the fourth and fifth rings (corresponding to a half etched ring and two fully etched rings, respectively). Etching of the other rings can be explained in a similar manner. (b) The device after refilling EGaIn into microchannels to recover the original array.

6.3 Conclusion

In summary, we have demonstrated that an aqueous electrochemical process involving the use of DI water with or without the addition of NaCl can be used as an effective means of erasing liquid metals via etching of the oxide layer that stabilizes the shape of the material. To demonstrate this, we initially measured the erasure rate using water with varying concentrations of NaCl. We found that the erasure rate could be effectively controlled by both the applied voltage and the NaCl concentration. In general, higher voltages or higher concentrations of NaCl contributed to a faster erasure rate. Using this information, we fabricated a microfluidic device with embedded microchannels in the form of a closed ring array, as well as an adjacent geometry for various aqueous solutions. Using embedded gold electrodes, we demonstrated the ability to selectively erase one or a group of unit cells in a random access manner. This approach provides the capability to create large-scale geometry changes within a device that can be fully reconfigured. Although we used a specific device geometry, the approach can be extended to other geometries and other domains, such as reconfigurable antennas and circuits. Within the field of plasmonics and metamaterials, we expect this to create greater flexibility in designing a broader range of devices.

6.4 Methods

For the fabrication of SU-8 template, we coated a silicon wafer with SU-8 3010 photoresist and spun it at 5000 rpm for 30 seconds. This film was exposed to UV light using a blank mask to form a flat layer, which was used to improve the adhesion between the silicon wafer and the upper SU-8 patterned layer. A second layer of SU-8 3010

photoresist was then spun cast at 3000 rpm. UV lithography using a mask with the structured pattern yielded a thin 10 μm photoresist layer with the designed pattern. A third layer of SU-8 3025 photoresist was spun at 4000 rpm above the second layer of SU-8 3010 photoresist. After baking, it was aligned and exposed to UV light using a mask with the CRR and two straight-line patterns. The third layer had a thickness of 22 μm. Both photoresist layers were then simultaneously developed to obtain the final two-layer pattern.

For soft lithography, a PDMS pre-polymer was mixed with a curing agent using a volume ratio of 7:1, degassed, poured onto the SU-8 template, and cured for 2 hours at 60 °C. After curing, the inverse PDMS replicas were peeled off and reversibly bonded with a glass substrate having patterned electrodes through van der Waals forces, yielding the desired microfluidic channel-based device.

For embedded electrodes for electrolysis, we deposited a 10 nm layer of Cr and a 180 nm layer of Au on a clean glass slide. Using standard wet etch techniques, we patterned the metal to define electrodes. The patterned PDMS mold was aligned with Au electrodes and reversibly bonded with the glass substrate to form the final device.

6.5 References

1. J. B. Pendry, A. J. Holden, W. J. Stewart, and I. Youngs, “Extremely low frequency plasmons in metallic mesostructures,” Phys. Rev. Lett. **76**, 4773–4776 (1996).

2. D. R. Smith, W. J. Padilla, D. C. Vier, S. C. Nemat-Nasser, and S. Schultz, “Composite medium with simultaneously negative permeability and permittivity,” Phys. Rev. Lett. **84**, 4184–4187 (2000).

3. H.-T. Chen, J. F. O’Hara, A. K. Azad, A. J. Taylor, R. D. Averitt, D. B. Shrekenhamer, and W. J. Padilla, "Experimental demonstration of frequency-agile terahertz metamaterials," Nature Photon. **2**, 295–298 (2008).

4. M. J. Dicken, K. Aydin, I. M. Pryce, L. A. Sweatlock, E. M. Boyd, S. Walavalkar, J. Ma, and H. A. Atwater, "Frequency tunable near-infrared metamaterials based on VO2 phase transition," Opt. Express **17,** 18330–18339 (2009).

5. T. Driscoll, H.-T. Kim, B.-G. Chae, B.-J. Kim, Y.-W. Lee, N. M. Jokerst, S. Palit, D. R. Smith, M. D. Ventra, D. N. Basov, "Memory metamaterials," Science **325,** 1518–1521 (2009).

6. R. C. Chiechi, E. A. Weiss, M. D. Dickey, and G. M. Whitesides, "Eutectic gallium–indium (EGaIn): a moldable liquid metal for electrical characterization of self-assembled monolayers," Angew. Chem. **120,** 148–150 (2008).

7. M. D. Dickey, R. C. Chiechi, R. J. Larsen, E. A. Weiss, D. A. Weitz, and G. M. Whitesides, "Eutectic gallium-indium (EGaIn): a liquid metal alloy for the formation of stable structures in microchannels at room temperature," Adv. Funct. Mater. **18**, 1097–1104 (2008).

8. J.-H. So, J. Thelen, A. Qusba, G. J. Hayes, G. Lazzi, and M. D. Dickey, "Reversibly deformable and mechanically tunable fluidic antennas," Adv. Funct. Mater. **19**, 3632–3637 (2009).

9. J. Wang, S. Liu, Z. V. Vardeny, and A. Nahata, "Liquid metal-based plasmonics," Opt. Express **20**, 2346–2353 (2012).

10. S. Zhu, J.-H. So, R. Mays, S. Desai, W. R. Barnes, B. Pourdeyhimi, and M. D. Dickey, "Ultrastretchable fibers with metallic conductivity using a liquid metal alloy core," Adv. Funct. Mater. **23**, 2308–2314 (2013).

11. D. J. Lipomi, B. C.-K. Tee, M. Vosgueritchian, and Z. Bao, "Stretchable organic solar cells," Adv. Mater. **23,** 1771–1775 (2011).

12. E. Palleau, S. Reece, S. C. Desai, M. E. Smith, and M. D. Dickey, "Self-healing stretchable wires for reconfigurable circuit wiring and 3D microfluidics," Adv. Mater. **25,** 1589–1592 (2013).

13. J. Wang, S. Liu, S. Guruswamy, and A. Nahata, "Reconfigurable liquid metal based terahertz metamaterials via selective erasure and refilling to the unit cell level," Appl. Phys. Lett. **103,** 221116 (2013).

14. L. Cademartiri, M. M. Thuo, C. A. Nijhuis, W. F. Reus, S. Tricard, J. R. Barber, R. N. S. Sodhi, P. Brodersen, C. Kim and R. C. Chiechi, and G. M. Whitesides, "Electrical Resistance of Ag^{TS}–$S(CH_2)_{n-1}CH_3$/Ga_2O_3 /EGaIn Tunneling Junctions," J. Phys. Chem. C **116,** 10848–10860 (2012).

15. J. O. Bockris, and A. K. N. Reddy, *Modern Electrochemistry: An Introduction to an Interdisciplinary Area* (Springer Science & Business Media, 1973).

16. M. G. Fontana, *Corrosion Engineering* (McGraw-Hill Book Company, 1985).

17. M. Pourbaix, *Atlas of Electrochemical Equilibria in Aqueous Solutions* (National Association of Corrosion Engineers, 1974).

18. J. C. MacDonald, D. C. Duffy, J. R. Anderson, D. T. Chiu, H. Wu, O. J. A. Schueller, and G. M. Whitesides, "Fabrication of microfluidic systems in poly (dimethylsiloxane)," Electrophoresis **21,** 27–40 (2000).

19. J. Wang, S. Liu, S. Guruswamy, and A. Nahata, "Reconfigurable terahertz metamaterial device with pressure memory," Opt. Express **22,** 4065–4074 (2014).

CHAPTER 7

RECONFIGURABLE TERAHERTZ METAMATERIAL DEVICE WITH PRESSURE MEMORY

7.1 Introduction

Metamaterials have gained significant attention over the last decade because they can exhibit electromagnetic properties that are not readily available in naturally occurring materials [1]. In the terahertz (THz) spectral range, which has traditionally been referred to as the gap in the electromagnetic spectrum, the need for useful device technologies is particularly acute. Nevertheless, a number of device capabilities, including frequency-agile filters [2], switches [3], absorbers [4] and phase modulators [5] have been demonstrated recently. Of particular interest is the ability to tune the resonant response of THz metamaterials, since this can provide for more flexible functionalities. As an example, tuning of the spectral response can be accomplished through the application of optical radiation [3] or an external voltage [6], which can change the carrier density of a semiconductor material that lies within the gap of a split ring resonator. Such changes can also be accomplished through temperature or magnetic control [7,8], which has been used to switch a superconductor between its normal and superconducting states. However, since all of these implementations are based on the use of solid-state materials, once the devices are fabricated, their basic geometry is fixed. Thus, the basic transmission spectrum is largely unchanged and only the magnitudes of the individual resonances are varied, depending upon the strength of the external excitation.

Since the transmission properties of metamaterials are determined primarily by the geometric parameters of the metallic elements, the functional flexibility of metamaterial devices can improve dramatically if the shape of the metallic element itself can be altered. Liquid metals, such as EGaIn, offer significant benefits for the development of devices in which large-scale reconfigurability is desirable. EGaIn (78.6% Ga and 21.4%

In by weight) has many advantageous properties in this regard: i) It exhibits low viscosity in the absence of an oxidized surface. The bulk viscosity is approximately twice that of water [9], ii) it has low toxicity [10], iii) the melting point is ~15.5 °C and is therefore liquid at room temperature, and iv) the EGaIn surface forms a thin passivating oxide layer of gallium, which allows it to support non-spherical shapes [11]. The last two properties make the metal particularly useful for a variety of stretchable devices, including antennas [12,13], plasmonic devices [14,15], fibers [16], solar cells [17] and 2D and 3D self-healing wires [18]. Furthermore, within the microchannels, the liquid metal only flows when the applied pressure exceeds the critical pressure for that dimension and maintains its structural stability when the applied pressure is relieved [10]. Based on this property, EGaIn has been used to demonstrate pressure-responsive frequency shifting antennas [19] and reconfigurable circuits [20].

In this submission, we demonstrate the utility of EGaIn for metamaterial applications as a pressure driven, pressure memory device. In contrast to earlier demonstrations, the approach described here allows for switching between multiple device configurations, as well as the ability to reset the device. Using well-developed microfluidics technology [21], we use soft lithography techniques to fabricate microfluidic channels that are embedded within a PDMS film. EGaIn is injected into the air voids through injection channels that are common to the individual metamaterial structures. Since the metal elements are based on liquid metals, the device geometry can be easily switched based on the geometry of the microchannels. By reducing the cross-sectional area of specific microchannels, the critical pressure needed to inject EGaIn increases. Thus, by controlling the injection pressure, we can directly control the device geometry and, thus,

the spectral properties of the device. This is accomplished by using a device geometry that incorporates three different microchannel cross-sectional areas, which correspond to three different critical pressures. When the applied pressure exceeds each critical pressure, we obtain different device geometries: split ring resonators (SRRs), closed ring resonators (CRRs) and irregular closed rings. The approach is sufficiently general that it can be applied to a wide variety of other geometries and applications.

7.2 Experimental Details

We fabricated a device composed of a 7 × 9 array of rings. In the schematic diagram of a unit cell, shown in Figure 7.1(a), the lower horizontal channel acted as the common injection channel for all 9 elements in each row, with all 7 injection channels connected via a common inlet reservoir. The outer radius of the rings was R_2 = 86 μm and the inner radius of the rings was R_1 = 68.5 μm, corresponding to the first critical channel width of W_1 = 17.5 μm. The length of the gap in the ring was g = 15.5 μm, corresponding to the second critical channel width of W_2 = 6.2 μm. Finally, the third critical channel width, W_3 = 4.0 μm, was associated with the narrow horizontal section leading to the upper(wider) horizontal channel. Since all of the microchannels were 10 μm in height, only the three critical channel widths determined the operation of the device. The other device parameters included the width of the lower injection channel, D_1 =25.5 μm, the width of the upper (diagonal) connection channel, D_2 =18.5 μm, the width of top horizontal channel, D_3 =20 μm, and the periodicity of rings, P = 315 μm, along both the x- and y- axes. In Figure 7.1(b), we show an optical microscope image of a portion of the ring array, in which EGaIn filled all of the microchannels through the common lower

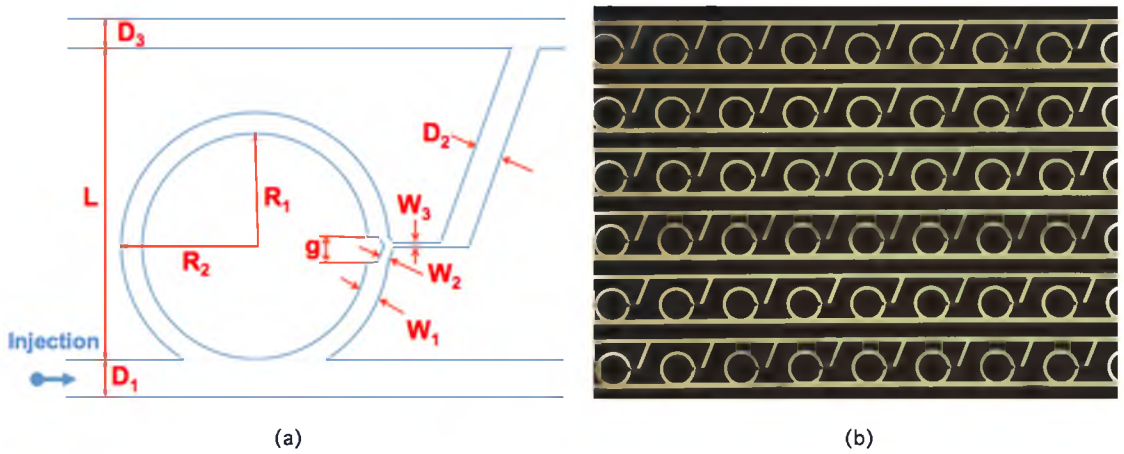

Figure 7.1. Schematic diagram of the unit cell. (a) A unit cell from the 7 × 9 array of rings. The device is composed of microfluidic channels fabricated within a PDMS mold. The lower horizontal channel in the figure (width D_1) serves as the injection channel for all nine rings in the row. The seven injection channels, one per row, are connected to a common inlet. The periodicity of the rings is P = 315 μm in both dimensions and the distance between the upper and lower horizontal channels is L = 199.5 μm. All of the other dimensions are described in the main text. (b) Photograph of the metamaterial device in which all of the microchannels are filled with EGaIn.

injection channels.

In order to fabricate the device, we first created a template using conventional photolithographic techniques and then transferred the pattern to a PDMS mold. To accomplish this, we coated a silicon wafer with SU-8 3010 photoresist that was spun cast at 5000 rpm for 30 seconds. After soft baking the photoresist at 95° for 2.5 minutes, the wafer was exposed to UV light using a blank mask and then post baked at 65° for 1 minute and then 95° for 1.5 minutes. The resulting 6 μm thick planar layer was used to improve the adhesion between the silicon wafer and an upper SU-8 patterned layer. This intermediate layer removed the need for additional surface modifications (e.g., through the use of silanes). A second (upper) layer of SU-8 3010 photoresist was then spun cast at 3000 rpm for 30 seconds. After UV exposure of the photoresist using a mask with the

appropriate pattern, the wafer was first baked and then developed, yielding a thin 10 μm upper photoresist layer with the designed pattern. This upper layer served as the template for the PDMS structure that was fabricated via soft lithography. A PDMS pre-polymer was mixed with a curing agent using a weight ratio of 7:1, degassed, poured onto the SU-8 template and cured for 2 hours at 60° C. After curing, the inverse PDMS replica was peeled off and sealed with a 120 μm thick planar section of PDMS using a high voltage corona, yielding a 690 μm thick final structure. Finally, the device reservoir was connected to a syringe, which was controlled by a syringe pump through a NanoPort assembly. We also fabricated a flat unstructured 690 μm thick PDMS film to act as a reference in the THz transmission measurements.

We used THz time-domain spectroscopy (THz TDS) to measure the normalized transmission spectra, $t(\nu)$, of the electric field through the device, where ν is the THz frequency [22]. The sample was mounted on a metal frame in which the opening size exposed only the metamaterial array. Photoconductive devices were used for both emission and coherent detection. An off-axis paraboloidal mirror was used to collect and collimate the THz radiation from the emitter to the device. The THz beam was normally incident on the surface of the metamaterial sample. In contrast to conventional optical measurements, THz TDS allows for direct measurement of the THz electric field, yielding both amplitude and phase information. By transforming the time-domain data to the frequency domain, we are able to determine independently both the magnitude and phase of the amplitude transmission coefficient, $t(\nu)$, using the relation

$$t(\nu) = |t(\nu)| \exp[i\varphi(\nu)] = \frac{E_{sample}(\nu)}{E_{reference}(\nu)} \quad (7.1)$$

In this expression, E_{sample} and $E_{reference}$ are the measured THz electric fields with either the sample or reference in the beam path, respectively, and $|t(\nu)|$ and $\varphi(\nu)$ are the magnitude and phase of the amplitude transmission coefficient, respectively. While the phase properties of the device are important, we only discuss the amplitude spectra in this work. We measured the injection pressure within the device using a pressure gauge that was connected between the syringe and the inlet through a Y connector. We also numerically simulated the response of the structure. The metal was modeled as a perfect electrical conductor using the device parameters given above, while the dielectric properties of PDMS were taken from THz refractive index measurements [14].

7.3 Results and Discussion

In order to demonstrate how the injection pressure can be used to control the transmission properties of this metamaterial device, we slowly ramped the injection pressure applied by the syringe to a value of ~255 kPa. Until that pressure value was reached, there was no EGaIn flow into the main injection channels (width D_1). However, when the pressure was further increased above ~255 kPa, the main injection channels and split ring channels easily filled with EGaIn. In Figure 7.2(a), we show an optical microscope image of a portion of the partially filled array. It is important to note that in all of the unit cells, only the injection channels and SRRs were filled with the liquid metal and there was no leakage into the channels forming the SRR gaps. Importantly, because of the formation of a surface oxide layer that stabilizes the shape of EGaIn, when

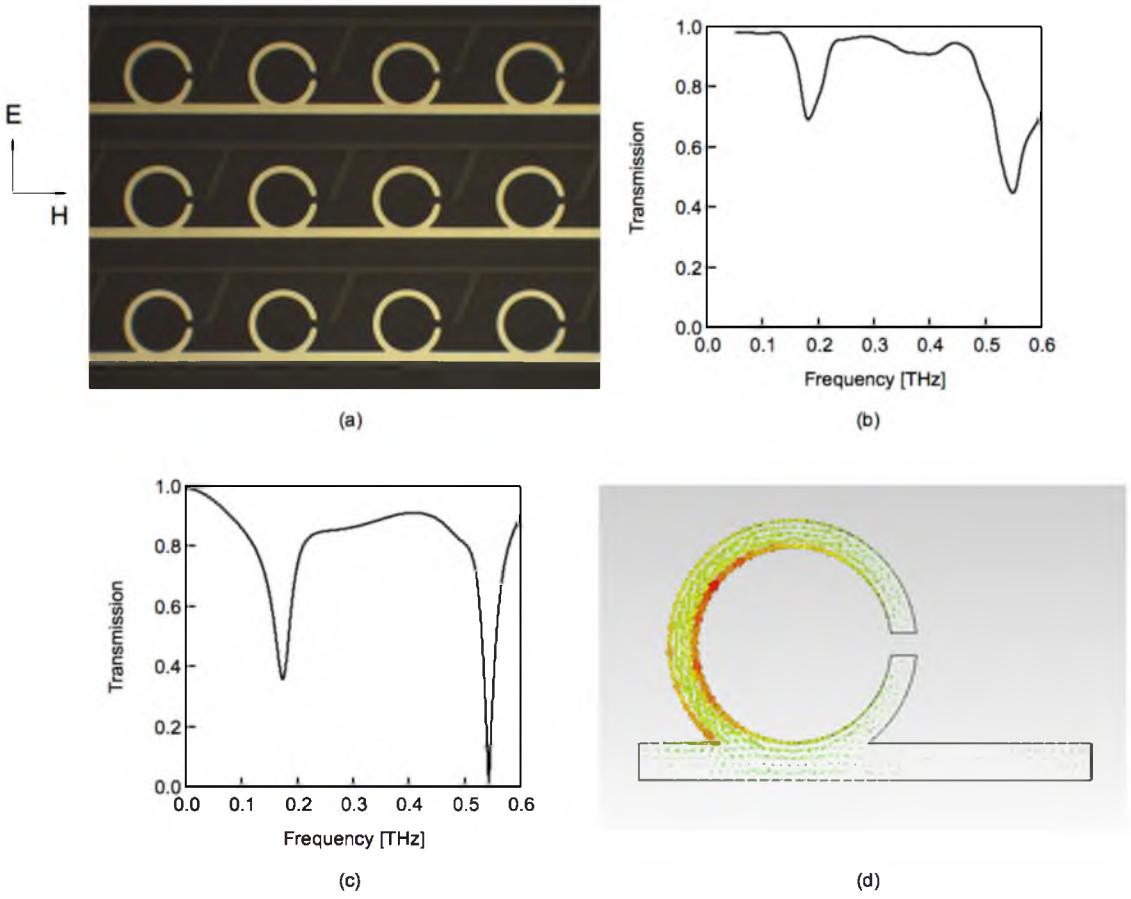

Figure 7.2. Split ring resonators. (a) Photograph of a portion of the split ring resonator array. The background structures in the image are unfilled microchannels. Once the split ring resonators are formed and the pressure is released, this configuration is stable for any applied pressure between 0 and ~ 255 kPa. (b) Measured transmission spectrum with the THz electric field polarized perpendicular to the horizontal injection lines. (c) Numerically simulated transmission spectrum under the same excitation scheme. d) Snapshot of the numerically simulated current distribution using an excitation frequency of 0.17 THz.

the injection pressure was released, the device geometry remained unperturbed. This behavior is fundamentally different from that of Hg, which does not form an oxide surface and can retract from the channel when pressure is released because of its high surface energy and lack of a stabilizing mechanism [10].

In Figure 7.2(b), we show the measured transmission spectrum with the THz electric field normally incident on the device and polarized perpendicular to the injection lines and the gap in the SRRs. In this orientation, the straight injection lines have little effect on the transmitted spectrum. We observe two absorption resonances located at 0.17 THz and 0.54 THz. The center frequencies of these resonances are associated with the orientation of the SRR, its geometrical parameters and the dielectric properties of the surrounding dielectric [3.6]. In Figure 7.2(c), we show the numerically simulated transmission spectrum using the same parameters as in the experiments. The resonant frequencies found here are the same as in the experimental results, although the latter resonances are shallower. We attribute the difference between these spectra primarily to the fact that periodic boundary conditions were used in the numerical simulations, while a finite array was used in the experiments. Furthermore, the metal was modeled as a perfect electrical conductor in the simulations, while EGaIn has a DC conductivity that is more than an order of magnitude smaller than that of Au [23]. Finally, although soft lithography techniques allow for the fabrication of relatively high precision samples, the application of an injection pressure may lead to small differences between individual unit cells, especially in the length of the SRR gaps.

The origin of the resonances in SRRs is well known at this point. The absorption resonance at 0.17 THz arises from an LC response of the SRR, in which circulating

currents produced from the incident time varying electric field generates a magnetic field polarized perpendicular to the plane of device. In Figure 7.2(d), we show a snapshot of the current distribution using an excitation frequency of 0.17 THz, which clearly shows the circulating current. The resonance at 0.54 THz is associated with a higher order dipole resonance, which arises from currents induced by the electric field of the incident radiation on opposite sides of the SRRs. This resonance is related to the plasmon resonance of cut wires and is associated with the finite side length of the SRRs [24].

As we slowly increased the applied injection pressure, but kept it below ~296 kPa, there were no changes in the device geometry. However, when the pressure exceeded ~296 kPa, EGaIn flowed into the SRR gap channels. The resulting device structure, in which the SRRs switched over to being closed ring resonators, is shown in Figure 7.3(a). The measured transmission spectrum, again with the incident THz radiation polarized perpendicular to the injection lines, is shown in Figure 7.3(b). The double resonance associated with the SRRs has now abruptly changed to a single resonance within the spectral window. To validate this result, we also numerically simulated the transmission spectrum, shown in Figure 7.3(c). Both spectra have a single resonance dip centered at 0.40 THz, although the experimentally measured resonance is shallower and broader. We attribute these differences to the same causes discussed above. In the case of CRRs, the LC response disappears and there is no coupled magnetic field. This explains the disappearance of the resonance centered at 0.17 THz. Similarly, the current distribution associated with the higher order resonance at 0.54 THz changes, causing it to disappear. In place of these two spectral features, there is now a resonance centered at 0.40 THz, which is the fundamental resonance mode of CRRs. As shown by the snapshot of the

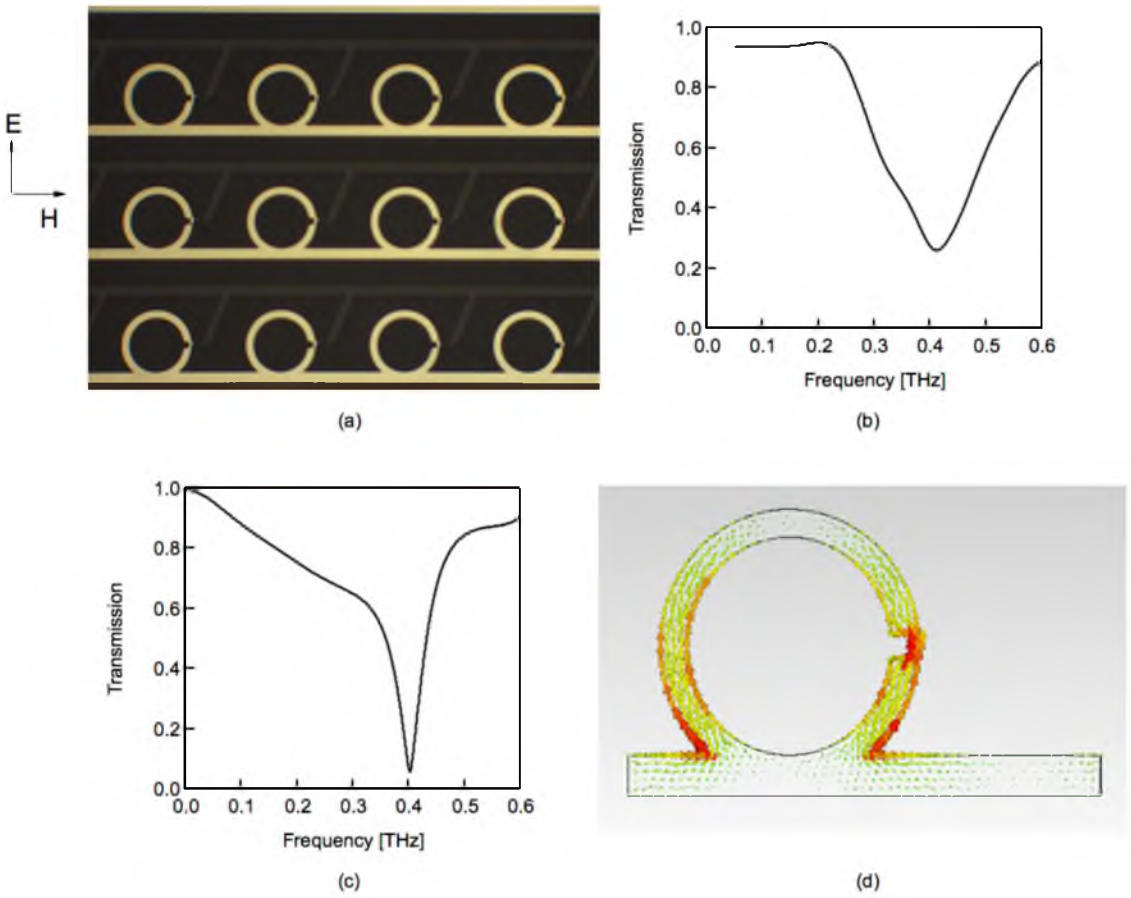

Figure 7.3. Close ring resonators. (a) Photograph of a portion of the closed ring resonator array. The background structures in the image are unfilled microchannels. Once the CRRs are formed and the pressure is released, this configuration is stable for any applied pressure between 0 and ~296 kPa. (b) Measured transmission spectrum with the THz electric field polarized perpendicular to the horizontal injection lines. (c) Numerically simulated transmission spectrum under the same excitation scheme. (d) Snapshot of the numerically simulated current distribution using an excitation frequency of 0.40 THz.

current distribution in Figure 7.3(d), the current is distributed nearly evenly between the two side segments of equal length, parallel to the THz electric field and oscillating in-phase [25]. The resonance associated with CRRs is much broader than those for SRRs, which arises from the asymmetry of the ring shape along the electric field axis.

Up to this point, we have shown that the metamaterial can switch from SRRs to CRRs. While such switching has been demonstrated using a variety of techniques, the

method used here can allow for further changes in the configuration, making this a potentially more flexible approach. To demonstrate this, we further increased the applied injection pressure. When the applied pressure was kept below ~386 kPa, we found that there were no changes in the device geometry. However, when the pressure increased beyond ~386 kPa, the narrow horizontal channel of width W_3, as well as the channels of width D_2 and D_3 filled with EGaIn (i.e., all channels in the device were filled). It should be noted that the latter two channels (of widths D_2 and D_3) were also filled because the critical pressure required to fill them was lower than ~386 kPa. The resulting device configuration, which we refer to as an irregular CRR, is shown in Figure 7.4(a).

In Figure 7.4(b), we show the experimental transmission spectra, again with the THz electric field polarized perpendicular to the horizontal injection lines. The spectrum is characterized by a low frequency narrow linewidth resonance centered at 0.13 THz and a much broader linewidth resonance centered at 0.4 THz. In the numerically simulated response of this geometry, shown in Figure 7.4(c), there is a low frequency narrow linewidth resonance centered at 0.13 THz. However, the higher frequency resonance is actually composed on two resonances: a resonance at 0.39 THz and a shallower resonance centered at 0.44 THz. The former resonance is similar to that shown in Figure 7.3(c), though red-shifted by ~10 GHz. In the experimental measurements, the linewidth of the resonance is sufficiently broad that the two separate resonances cannot be resolved.

The frequencies of each of these resonances can be understood by considering the relevant current distributions. In Figure 7.4(d), we show a snapshot of the current distribution for an excitation frequency of 0.13 THz. The resonance is associated with the

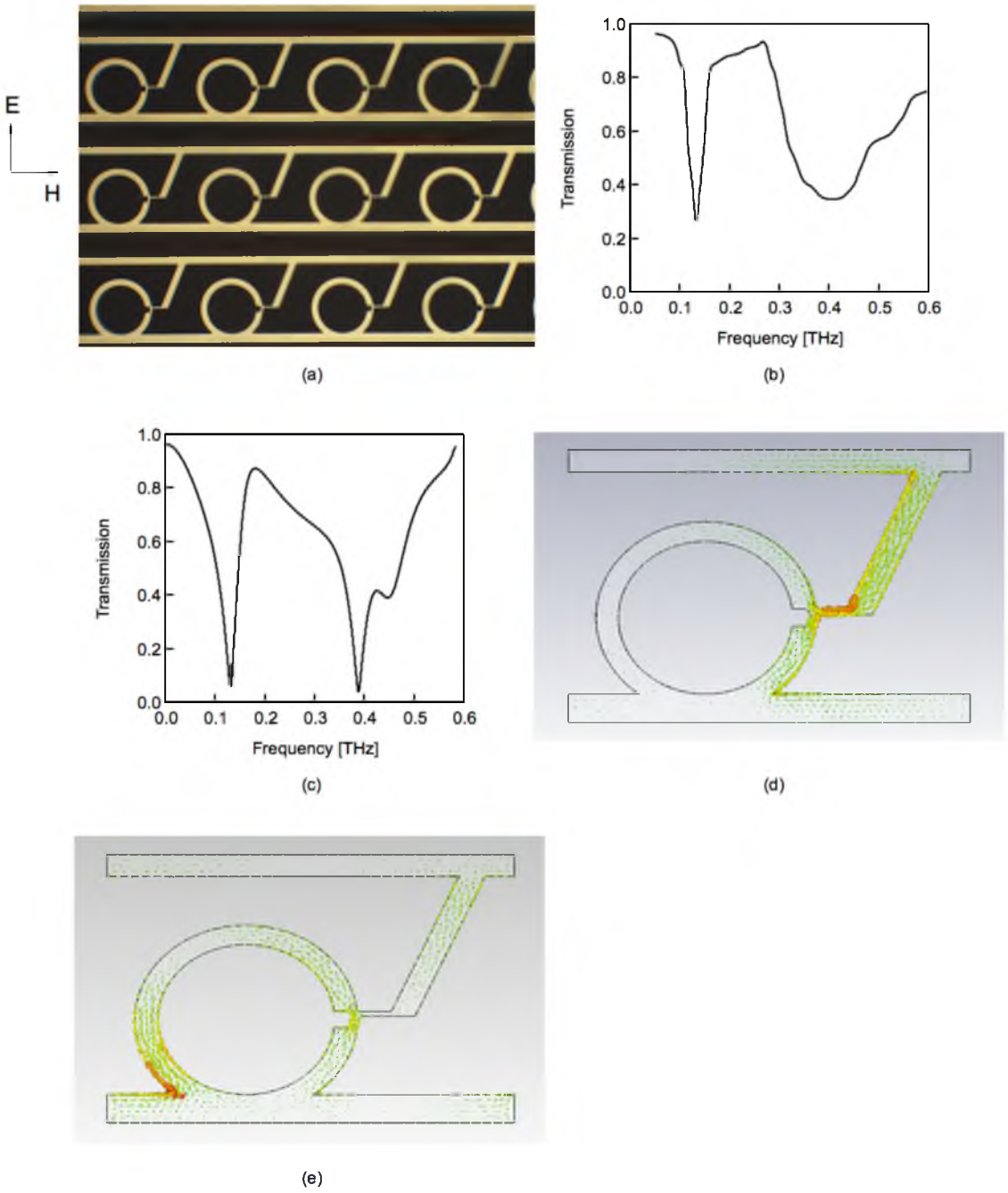

Figure 7.4. Irregular ring resonators. (a) Photograph of a portion of the irregular ring array. (b) Measured transmission spectrum with the THz electric field polarized perpendicular to the horizontal injection lines. (c) Numerically simulated transmission spectrum under the same excitation scheme. (d) Snapshot of the numerically simulated current distribution using an excitation frequency of 0.13 THz. (e) Snapshot of the numerically simulated current distribution using an excitation frequency of 0.44 THz.

large rectangle-like closed rings that are formed by the right edge of adjacent unit cells and the upper and lower horizontal lines and is analogous to the response of CRRs. However, since the area of this composite structure is larger than the CRRs, the resonance is red-shifted. The resonance at 0.39 THz arises from the CRRs and is the same as seen in Figure 7.3(d). In Figure 7.4(e), we show a snapshot of the current distribution for an excitation frequency of 0.44 THz, which suggests that the resonance is associated with coupling between the CRR and the diagonal metallic line. In comparing Figure 7.4(e) with Figure 7.3(d), we find that the diagonal metallic line reduces the resonant dipole length to only the left half of the CRR. This reduced length increases the resonance frequency from 0.4 THz to 0.44 THz. This dipole resonance is the dominant part in Figure 7.4(e). Because the dipole occurs only on one side of the structure (i.e., half of the left side of the CRR), the 0.44 THz resonance is shallower than the 0.4 THz resonance. In fact, for numerical simulations in which the diagonal line is removed, this high frequency contribution to the spectrum disappears.

Filling the device required that the applied pressure exceed three different values for the critical pressure for three different geometries. In order to understand this behavior, we consider the relationship between the applied pressure and the channel dimensions. In a channel, the pressure, P, required to initiate flow is associated for a channel of width (W) and height (H) is given by

$$P = 2\gamma\cos(\theta)\left(\frac{1}{W}+\frac{1}{H}\right). \tag{7.2}$$

Here, γ is a parameter that is related to the interfacial force per unit length required for

EGaIn to flow and θ is the contact angle between EGaIn and PDMS (=150°) [10]. Dickey et al. have previously found that $\gamma = 0.63$ N/m in the microchannels that they used [10]. In Figure 7.5, we plot the critical pressure as a function of the channel dimensions. In the case of the lower horizontal injection channel and the SRR, both filled simultaneously when the pressure exceeded ~255 kPa, even though the two have slightly different dimension. Using Equation (7.2), we fit a line to only the two higher pressure data points and find that the best fit value for γ is 0.58, in reasonable agreement to the value mentioned above. One possible reason for the slight difference in best-fit values for γ might arise from the actual dimensions for the SRR gap channel and the short horizontal channel of width W_2. In both cases, the channels lengths are only slightly larger than the corresponding channel widths. In earlier work, the channel length was more than ten

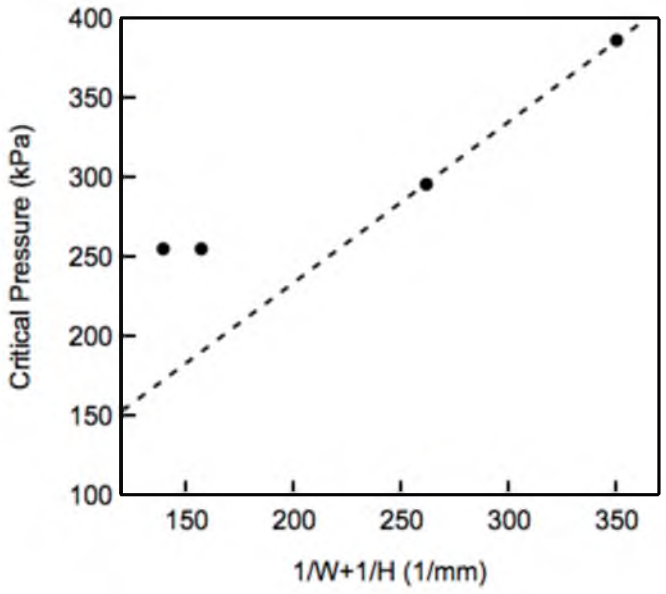

Figure 7.5. The critical applied pressure required for filling EGaIn for each channel segment as a function of the sum of the inverse height (H) and width (W). The dashed line is a best-fit to only the two higher pressure data points. The slope of the best-fit line to the data for EGaIn is 1.01 N/m.

times its width, which may affect the required pressure [10]. In addition, the rectangular cross-section channels may deform slightly under pressure and, thus, correspond to different dimensions than used in Equation (7.2). Finally, it should be noted that Equation (7.2) is only an approximation, since it is very difficult to analyze the interfacial curvature in a rectangular shaped channel.

Based on the dimensions of the channels and the best fit value for γ, we would expect that the critical pressure required for EGaIn to flow into the lower injection channels of width D_1 to be ~140 kPa and the critical pressure required to fill the SRR channels of width W_1 to be ~159 kPa. The need for a much larger applied pressure to fill these two channels can be attributed to several issues. First, the large difference between the dimensions of the inlet reservoir and the injection channels may cause the required injection pressure to deviate from Equation (7.2). Second, the thickness of the PDMS layer in the device described here was much thinner than was used in [10]. The increased gas permeability would lead to a significant increase in the required critical pressure. Third, the distance between the rings and the outlet affects the required pressure. If the rings were too close to the outlet, EGaIn would simply flow out of the injection channel without ever entering the rings. Given that the critical pressures for filling the injection channels and the SRR channels are very close, it is difficult to fill only the injection channels, without having any leakage into the SRRs. In fact, we did not observe two separate critical pressures for the two different channels.

In order to demonstrate full reconfigurability, there needs to be a final step that allows the device to be reset to its original configuration. As noted earlier, an oxide surface layer forms on the liquid metal stabilizing its configuration. In the absence of this oxide, EGaIn

has a viscosity that is twice that of water and a surface tension that is similar to that of Hg. Since PDMS is gas permeable, the oxide layer can be dissolved using acids. Therefore, when the entire device is exposed to hydrochloric acid (HCl), in the presence of light mechanical pressure, the oxide layer surrounding the EGaIn metal within the device can be quickly dissolved, at which point the EGaIn retracts out of the microchannels and returns to either the inlet or the outlet. In Figure 7.6(a), we show an image of the device after it has been exposed to HCl for 1 minute. In Figure 7.6(b), we show the corresponding transmission spectrum. It is clear that although several small remnants of liquid metal remain in some of the channels, they have no impact on the transmission properties of the reset device.

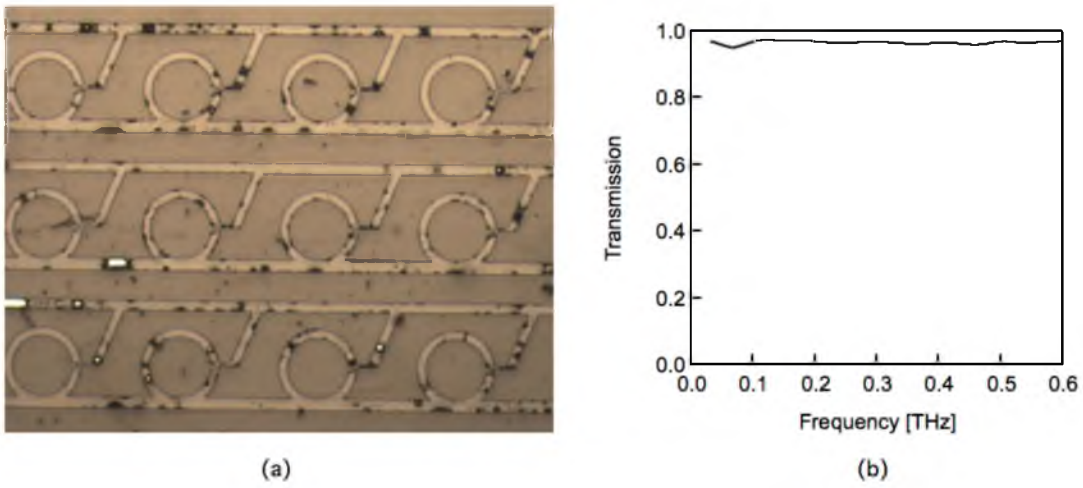

Figure 7.6. Properties of the reset device. (a) Photograph of a portion of the reset device (all of the EGaIn was returned to either the inlet or the outlet). The two short white line segments correspond to EGaIn that remained in the upper and lower horizontal channels. The different contrast in the image, as compared the earlier figures, was used to more clearly show the channel properties after resetting the device. (b) The corresponding transmission spectrum.

7.4 Conclusion

In summary, we have demonstrated a reconfigurable metamaterial device that utilizes liquid metal, EGaIn, as its metallic element. The device utilizes conventional microfluidic technology, where microchannels in the form of ring resonators are created in a PDMS mold. By carefully designing the dimensions of the microchannels, we can require different critical pressures for different segments of the device. Therefore, only specific sections of the device are filled with EGaIn when the corresponding critical pressure is exceeded. This allows for a device geometry that can change abruptly from one configuration to another, enabling dramatic changes in the corresponding transmission properties. Since it is the metallic elements that are changed, the number of possible configuration changes is limited only by the available pressure differences that can be set. Thus, such a device is not limited to the conventional two state configurations. In addition, because the liquid metal flow conditions are irreversible, in a general sense, the transmission spectra records the pressure applied to the liquid metals, providing a means for sensing and recording the external pressure through THz electromagnetic fields. Such a capability may be useful in structures that incorporate not only liquid metals, but also other liquids to create devices that combine plasmonics with more conventional microfluidic capabilities. Finally, although we only describe only one specific metamaterial geometry, the approach can be applied to a broad range of THz device technologies.

7.5 References

1. T. J. Yen, W. J. Padilla, N. Fang, D. C. Vier, D. R. Smith, J. B. Pendry, D. N. Basov, and X. Zhang, "Terahertz magnetic response from artificial materials," Science **303**,

1494–1496 (2004).

2. H.-T. Chen, J. F. O'Hara, A. K. Azad, A. J. Taylor, R. D. Averitt, D. B. Shrekenhamer, and W. J. Padilla, "Experimental demonstration of frequency-agile terahertz metamaterials," Nature Photon. **2**, 295–298 (2008).

3. W. J. Padilla, A. J. Taylor, C. Highstrete, M. Lee, and R. D. Averitt, "Dynamical electric and magnetic metamaterial response at terahertz frequencies," Phys. Rev. Lett. **96**, 107401 (2006).

4. N. I. Landy, S. Sajuyigbe, J. J. Mock, D. R. Smith, and W. J. Padilla, "Perfect metamaterial absorber," Phys. Rev. Lett. **100**, 207402 (2008).

5. H.-T. Chen, W. J. Padilla, M. J. Cich, A. K. Azad, R. D. Averitt, and A. J. Taylor, "A metamaterial solid-state terahertz phase modulator," Nature Photon. **3**, 148–151 (2009).

6. H.-T. Chen, W. J. Padilla, J. M. O. Zide, A. C. Gossard, A. J. Taylor, and R. D. Averitt, "Active terahertz metamaterial devices," Nature **444**, 597–600 (2006).

7. J. Gu, R. Singh, Z. Tian, W. Cao, Q. Xing, M. He, J. W. Zhang, J. Han, H.-T. Chen, and W. Zhang, "Terahertz superconductor metamaterial," Appl. Phys. Lett. **97**, 071102 (2010).

8. B. Jin, C. Zhang, S. Engelbrecht, A. Pimenov, J. Wu, Q. Xu, C. Cao, J. Chen, W. Xu, L. Kang, and P. Wu, "Low loss and magnetic field-tunable superconducting terahertz metamaterial," Opt. Express **18**, 17504–17509 (2010).

9. J. N. Koster, "Directional solidification and melting of eutectic GaIn," Cryst. Res. Technol. **34**, 1129–1140 (1999).

10. M. D. Dickey, R. C. Chiechi, R. J. Larsen, E. A. Weiss, D. A. Weitz, and G. M. Whitesides, "Eutectic gallium-indium (EGaIn): A liquid metal alloy for the formation of stable structures in microchannels at room temperature," Adv. Funct. Mater. **18**, 1097–1104 (2008).

11. R. C. Chiechi, E. A. Weiss, M. D. Dickey, and G. M. Whitesides, "Eutectic gallium–indium (EGaIn): A moldable liquid metal for electrical characterization of self-assembled monolayers," Angew. Chem. **120**, 148–150 (2008).

12. J.-H. So, J. Thelen, A. Qusba, G. J. Hayes, G. Lazzi, and M. D. Dickey, "Reversibly deformable and mechanically tunable fluidic antennas," Adv. Funct. Mater. **19**, 3632–3637 (2009).

13. M. Kubo, X. Li, C. Kim, M. Hashimoto, B. J. Wiley, D. Ham, and G. M. Whitesides, "Stretchable microfluidic radiofrequency antennas," Adv. Mater. **22**, 2749–2752 (2010).

14. J. Wang, S. Liu, Z. V. Vardeny, and A. Nahata, "Liquid metal-based plasmonics," Optics Express **20**, 2346–2353 (2012).

15. J. Wang, S. Liu, and A. Nahata, "Reconfigurable plasmonic devices using liquid metals," Opt. Express **20**, 12119–12126 (2012).

16. S. Zhu, J.-H. So, R. Mays, S. Desai, W. R. Barnes, B. Pourdeyhimi, and M. D. Dickey, "Ultrastretchable fibers with metallic conductivity using a liquid metal alloy core," Adv. Funct. Mater. **23**, 2308–2314 (2013).

17. D. J. Lipomi, B. C.-K. Tee, M. Vosgueritchian, and Z. Bao, "Stretchable organic solar cells," Adv. Mater. **23**, 1771–1775 (2011).

18. E. Palleau, S. Reece, S. C. Desai, M. E. Smith, and M. D. Dickey, "Self-healing stretchable wires for reconfigurable circuit wiring and 3D microfluidics," Adv. Mater. **25**, 1589–1592 (2013).

19. M. Rashed Khan, G. J. Hayes, J.-H. So, G. Lazzi, and M. D. Dickey, "A frequency shifting liquid metal antenna with pressure responsiveness," Appl. Phys. Lett. **99**, 013501 (2011).

20. B. L. Cumby, G. J. Hayes, M. D. Dickey, R. S. Justice, C. E. Tabor, and J. C. Heikenfeld, "Reconfigurable liquid metal circuits by Laplace pressure shaping," Appl. Phys. Lett. **101**, 174102–174102 (2012).

21. J. C. MacDonald, D. C. Duffy, J. R. Anderson, D. T. Chiu, H. Wu, O. J. A. Schueller, and G. M. Whitesides, "Fabrication of microfluidic systems in poly (dimethylsiloxane)," Electrophoresis **21**, 27–40 (2000).

22. D. Grischkowsky, S. Keiding, M. Van Exter, and C. Fattinger, "Far-infrared time-domain spectroscopy with terahertz beams of dielectrics and semiconductors," J. Opt. Soc. Am. B **7**, 2006–2015 (1990).

23. D. Zrnic and D. S. Swatik, "On the resistivity and surface tension of the eutectic alloy of gallium and indium," J. Less-Common Met. **18**, 67–68 (1969).

24. S. Linden, C. Enkrich, M. Wegener, J. Zhou, T. Koschny, and C. M. Soukoulis, "Magnetic response of metamaterials at 100 terahertz," Science **306**, 1351–1353 (2004).

25. D. Roy Chowdhury, R. Singh, J. F. O'Hara, H.-T. Chen, A. J. Taylor, and A. K. Azad, "Dynamically reconfigurable terahertz metamaterial through photo-doped semiconductor," Appl. Phys. Lett. **99**, 231101 (2011).

CHAPTER 8

INJECTION MOLDING OF FREE-STANDING THREE-DIMENSIONAL ALL-METAL TERAHERTZ METAMATERIALS

8.1 Introduction

In recent years, there has been great interest in developing metamaterials that exhibit electromagnetic properties not readily available in nature [1]. The artificial structure in these materials allows one to engineer the response through design of the geometrical layout of the metallic features and the surrounding dielectric media [2,3]. Much of the work in developing these structures has relied on creating 2D geometries on flat substrates using well-developed microfabrication techniques. While the approach has proven very successful, it also creates some issues and limitations. As an example, the introduction of a substrate breaks the symmetry of the metamaterial structure at the interface, which can induce bianisotropy [4,5]. Furthermore, in order to properly determine the electromagnetic properties of the structure, such as the effective dielectric constant, for many metamaterial geometries, it is preferable to use bulk (3D) materials [6,7]. The simplest approach for accomplishing this is to create a stack of 2D layers [6,8–11]. In the microwave and optical spectral regions, this is not a significant issue, since there are numerous low loss substrate materials. In the THz spectral range, however, there are relatively few good options, since most dielectric materials are lossy [12,13]. Thus, the complex refractive index properties of the substrate have to be considered and both the absorption loss and multiple reflections between the different substrate layers need to be taken into account.

This ability to engineer the response based on the geometry also suggests that more complex 3D geometries can yield unique capabilities. Indeed, such structures have been fabricated for applications at microwave frequencies by assembling appropriately patterned circuit boards [14]. Similarly, though the length scales at optical frequencies are

dramatically smaller, a variety of advanced fabrication techniques have been developed over the years that allow for similar device definition [11]. However, in the THz spectral range, while the relevant dimensions lie between those in the microwave and visible, far fewer well developed fabrication capabilities exist. In fact, there have only been a few reports of non-planar THz metamaterials, which in some cases have relied on UV and/or X-ray photolithography combined with repeated electroplating processes [15–17]. While these THz structures are unique and interesting, in some cases, they require advanced fabrication facilities that are not widely available. In light of these various considerations, it would be advantageous to develop a fabrication technique that is not only substrate-free and amenable to construction of complex 3D geometries, but also comparatively simple in terms of facilities requirements.

In this submission, we demonstrate that injection molding is an extremely versatile and comparatively easy technique for fabricating free-standing all-metal 2D and 3D THz metamaterials. We use gallium as the metal of choice, because of its advantageous physical properties: (i) it has a relatively low melting temperature (~ 30 °C) and, thus, forms a liquid with only mild heating (ii) it can be solidified at room temperature using an external control that does not rely on simply cooling the metal to room temperature and (iii) its shape can be more easily manipulated than other conventional metals at room temperature, allowing for the construction of complex 3D structures. We use soft lithography techniques to fabricate a peelable injection mold using microfluidic channels inscribed into polydimethylsiloxane (PDMS) films. Specifically, we create the requisite patterns within two PDMS films, which are then reversibly bonded through van der Waals forces. Since the geometry of the metallic structure is determined only by mold,

once the master template is fabricated, all further device fabrication can take place without the need for sophisticated microfabrication facilities.

8.2 Results and Discussion

We fabricated all of the samples using the basic procedure shown in Figure 8.1. Using an SU-8 photoresist coated silicon wafer, we used conventional UV photolithography to create the desired template pattern. We then used PDMS and soft lithography techniques to obtain the inverse replica of the SU-8 template. This patterned PDMS film was reversibly bonded to a second PDMS film that was either unpatterned or had its own separate embedded microchannel geometry. The reversible bonding process of two PDMS films occurs because PDMS is flexible and can conform to a flat surface through van der Waals forces [18]. After the films were bonded, pre-heated liquid gallium was injected into the microchannels. The metal was then solidified at room temperature, as discussed below. Finally, the two PDMS films were peeled apart leaving a free-standing metal device. We used THz time-domain spectroscopy to measure the absolute transmission properties of all of the devices.

Before discussing the device geometries that can be fabricated using this approach, we briefly describe the properties of gallium metal and the approach used to solidify the liquid metal in the PDMS mold. Gallium is a silvery, glass-like metal that has a DC conductivity of 3.7×10^6 S/m [19], which is only slightly smaller than that of lead [20]. While there are no published data reporting the THz dielectric properties of Ga, there is data for eutectic Ga-In, which is composed primarily of Ga and clearly shows metallic behavior in the THz spectral range [21].

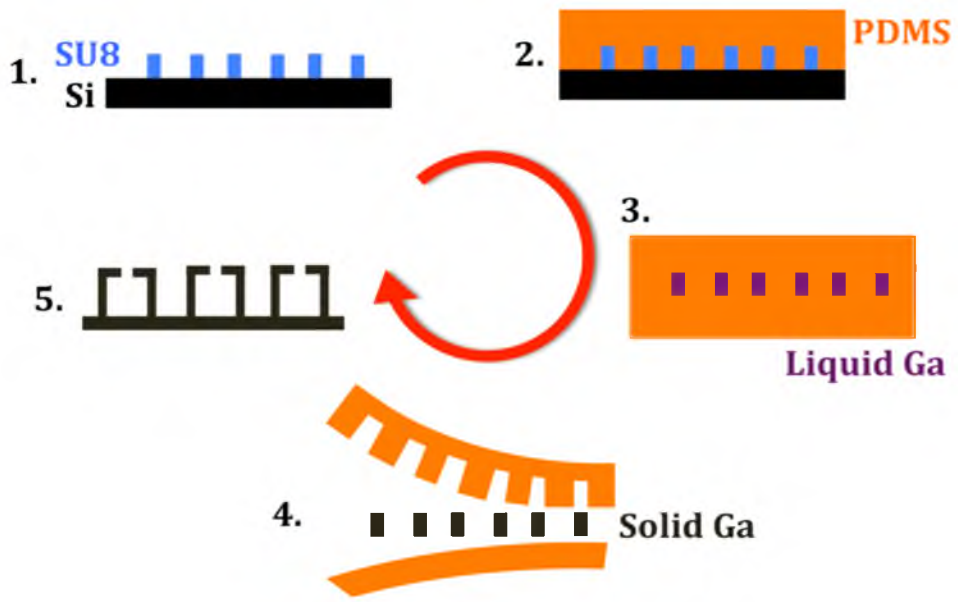

Figure 8.1. Steps in the fabrication process for injection molding of free-standing all-metal THz metamaterials.

Although liquid Ga normally solidifies at 30°C, it can be cooled and remain in a metastable liquid state below its freezing point, a process that is referred to as undercooling or supercooling [22]. In such cases, the magnitude of supercooling (i.e., the difference between the actual freezing point and the bulk material freezing point) increases as the liquid volume decreases. For the devices described here, the entire filled molds were placed in a freezer at -16 °C for 24 h. Surprisingly, even under these conditions, the injected Ga remained at least partially in its liquid state even after being kept at 46 °C below the bulk melting temperature. This ensured that no issues associated with solidification arose during the injection process, even with changes in the room temperature. Interestingly, we found that the liquid metal solidified quickly at room

temperature when a piece of solid Ga came into contact with it.

In order to explain this behavior, it should be noted that the melting temperature of various metals and materials is well known to decrease when the dimensions are reduced to the order of less than a few tens of nm, where quantum confinement effects become relevant. In the case of liquid Ga confined within random pore networks of different porous glasses with pore sizes of 16 and 2 nm, the corresponding freezing point was found to be suppressed to less than 265 K and 185 K, respectively [23]. Since the PDMS channels described here are significantly larger than those dimensions, we believe that the observed presence of liquid Ga in the channels at such low temperatures is due to the large nucleation barrier for both homogeneous (within the uniform metal) and heterogeneous (at the gallium-PDMS interface) nucleation of the solid Ga phase from liquid.

In general, the temperature dependence of homogeneous nucleation rate is very steep, especially for metals. As such, homogeneous crystallization in bulk metals can occur at temperatures well below the equilibrium bulk melting point by as much as ~220K, as has been shown for Cu [24]. The temperature dependence of the heterogeneous crystallization rate is also very steep, but freezing is expected to require lower supercooling than in the homogeneous nucleation case. The fact that the Ga remains in a partial liquid state even with significant supercooling (46° below the freezing temperature) is indicative of a large interfacial energy requirement during the nucleation process. However, when a solid Ga seed is brought into contact with the liquid, there is no nucleation barrier and the freezing proceeds without much supercooling.

We now discuss the fabrication of 2D free-standing Ga-based metamaterials

composed of split ring resonators (SRRs). While such structures can be created using a variety of techniques, we will use them as the basis for more complex 3D geometries described below. A schematic diagram of the resonator unit cell is shown in Figure 8.2(a). We designed and fabricated five separate 9 mm x 9 mm SRR geometries of different dimensions, as shown Table 8.1. A photograph of the SRR1 metamaterial is shown in Figure 8.2(b) and the corresponding transmission spectrum, with the normally incident THz radiation polarized perpendicular to the horizontal injection lines, is shown in Figure 8.2(c). In this orientation, the horizontal injection lines do not interact with the incident radiation and, thus, have little effect on the transmission spectrum. The single broad resonance centered at 0.32 THz arises from the coupled dipole resonance between the two arms of the SRR [25]. In Figure 8.2(d), we show the transmission spectrum with the normally incident THz radiation polarized parallel to the horizontal injection lines. In this case, there are three separate factors that contribute to the measured spectrum: a Drude-like response related to interaction with the long horizontal injection lines for frequencies below ~0.3 THz [26], an LC resonance in the SRR at 0.14 THz and a higher order dipole resonance at 0.5 THz associated with currents produced by the THz electric field on the opposite sides of the gap. As would be expected for these structures, the off resonance transmission is near unity and substantially higher than for equivalent devices fabricated on substrates, where the reported transmission spectra is often higher than expected because the measurements were referenced relative to the substrate.

Using this 2D structure as a building block, we now describe three separate approaches to creating 3D free-standing metamaterials. In the first approach, we create a stack using the five different SRR metamaterial layers, described in Table 8.1, with each

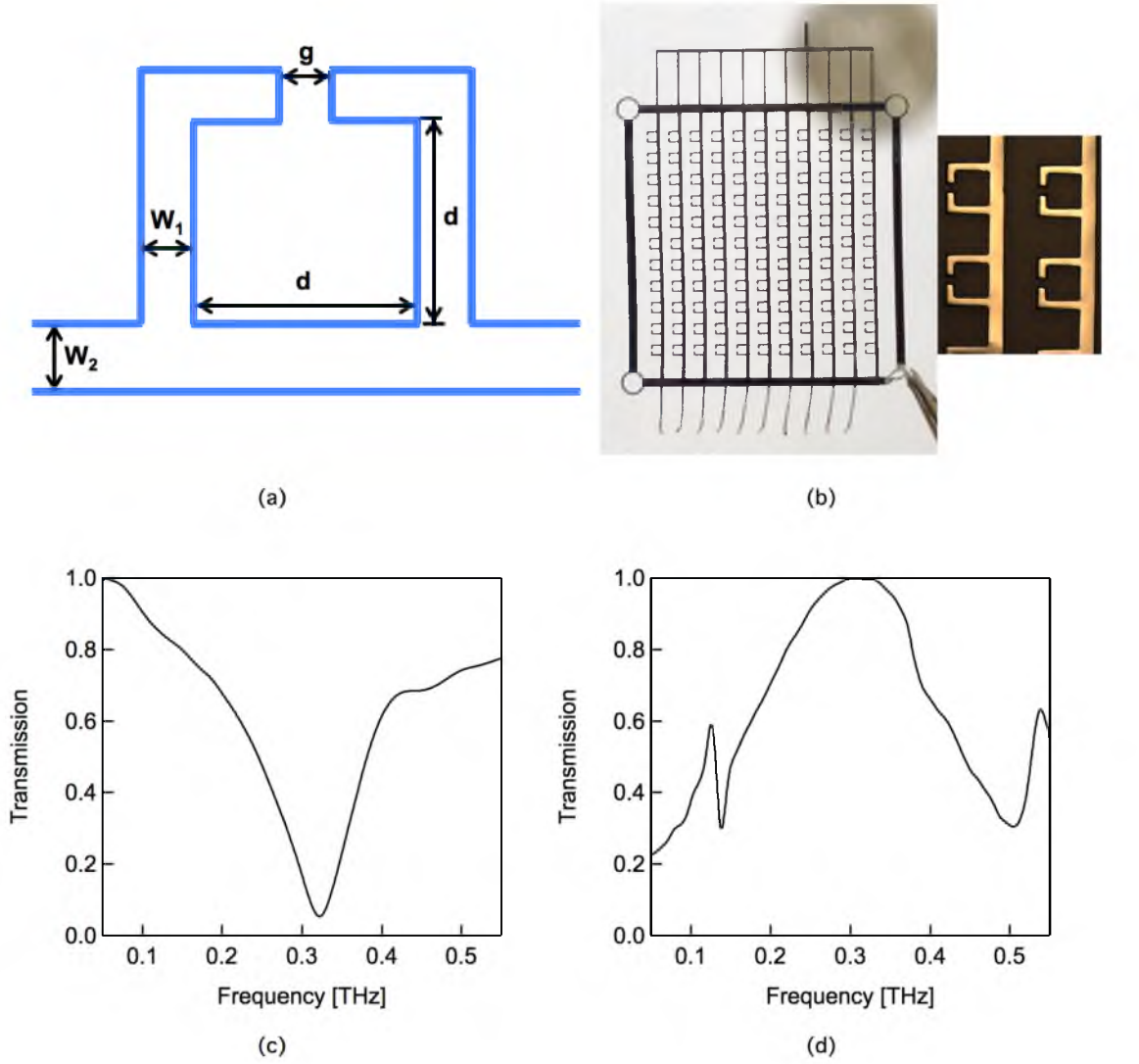

Figure 8.2. 2D free-standing metamaterials. (a) Schematic diagram of one unit cell of SRR metamaterial. The parameter values are given in Table 8.1. The lower horizontal connection line of width W_2 is used for injection and acts to connect the different unit cells. (b) Photograph of free-standing 2D SRR1 metamaterial with an enlarged image of a portion of the device to the right. (c) Transmission spectrum for SRR1 for normally incident THz radiation polarized perpendicular to the connection lines. (d) Transmission spectrum for SRR1 for normally incident THz radiation polarized parallel to the connection lines.

Table 8.1. Parameters for the split ring resonators.

	g (μm)	W_1 (μm)	d (μm)	W_2 (μm)	Periodicity (μm)	Thickness (μm)
SRR 1	70	72	274	120	740	80
SRR 2	66	56	250	115	740	80
SRR 3	70	66	260	120	740	80
SRR 4	85	69	304	110	740	80
SRR 5	90	72	343	110	740	80

layer separated by 160 μm using gallium spacers. In Figure 8.3(a), we show a photograph of the resulting ~1.13 mm thick free-standing metamaterial. The circular elements at the four corners of the device were used to align the layers. An expanded view of a portion of portion of the device is shown in Figure 8.3(b). For the wire dimensions shown in Table 8.1, we observed almost no sag in the individual layers, although this could become a concern with larger arrays. In that case, increasing the cross-section of the main horizontal injection lines can be used to minimize the issue.

In Figure 8.3(c), we show the transmission spectrum for normally incident THz radiation polarized perpendicular to the horizontal injection lines. The spectrum features a fast rising and falling edge and exhibits strong broadband transmission suppression between 0.2 THz and 0.36 THz. Because the interlayer interaction length is much smaller than the 160 μm layer spacing, we expect that the minor misalignment between layers will have little impact on the transmission spectrum [27,28]. We also expect minimal coupling between layers, corresponding to a simple superposition of the spectra

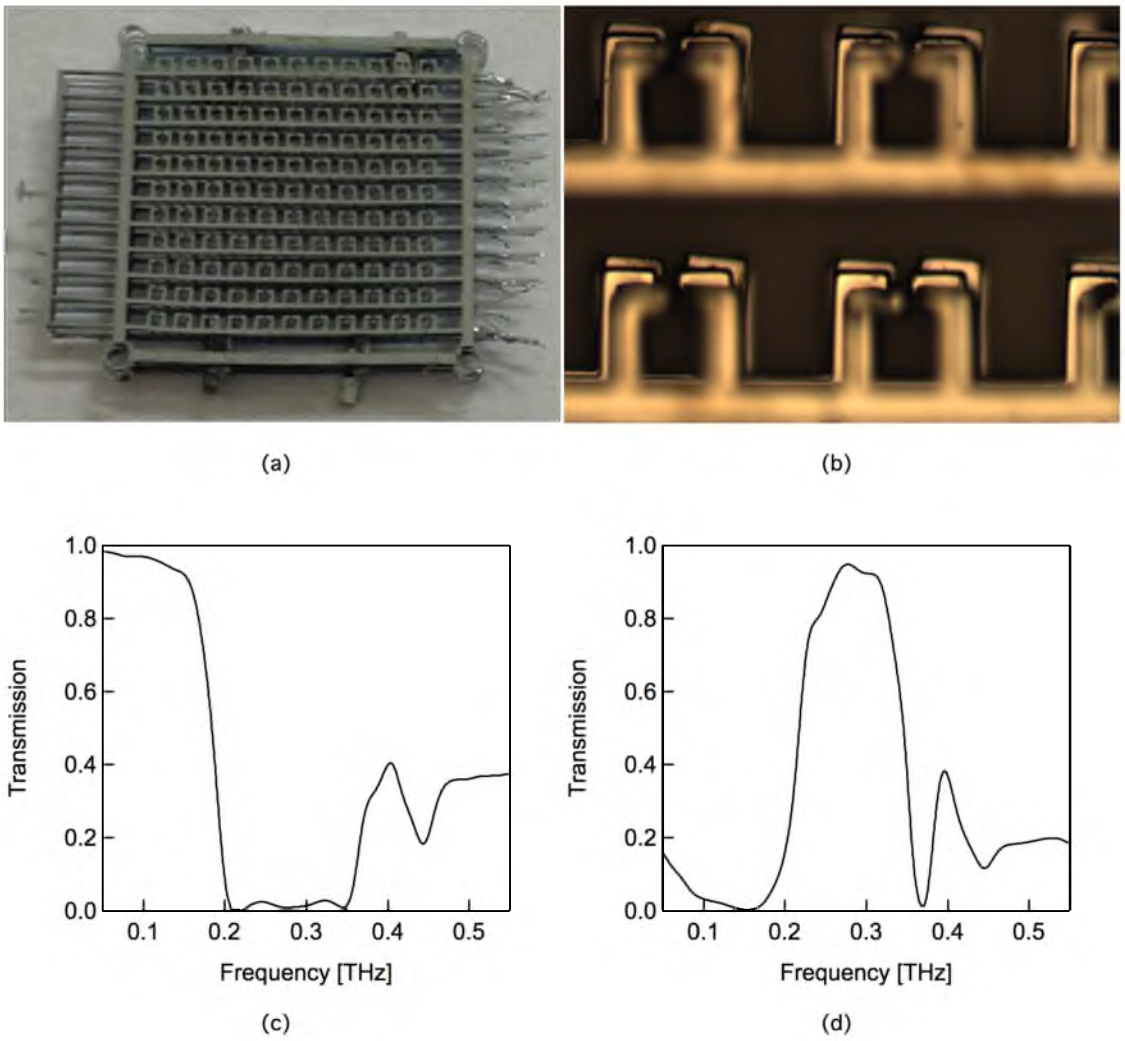

Figure 8.3. A multilayer stack of free-standing metamaterials. (a) Photograph of a stacked five-layer SRR metamaterial structure composed of SRR1 through SRR5. (b) Microscope image of a portion of the device. (c) Transmission spectrum for normally incident THz radiation polarized perpendicular to the connection lines. (d) Transmission spectrum for normally incident THz radiation polarized parallel to the connection lines.

associated with each layer. This is consistent with observations obtained from other metamaterial stacks [28]. In Figure 8.3(d), we show the transmission spectrum for normally incident THz radiation polarized parallel to the horizontal injection lines. In this case, the device response leads to a pass band with near unity transmission from ~ 0.2 – 0.36 THz.

In comparing the response of this structure to other multilayer metamaterials [8,28], it is clear that while the transmission suppression characteristics are approximately similar, the pass band transmission amplitudes are significantly higher here because there are no issues with absorption by the substrate. There are also no issues with Fabry-Perot resonances. The high transmission contrast for the two different excitation polarizations in the frequency range between 0.2 and 0.36 THz suggests the possibility of creating a THz modulator by dynamically changing the device orientation or device configuration [29,30]. Finally, we note that while this structure contains only five layers, the approach can be easily extended to incorporate a much larger number of layers.

A commonly used approach to creating an effective 3D metamaterial relies on the use of very thin flexible substrates, which allow for some level of bending and flexing [15,28,31]. However, the extent to which such deformations can be made are typically somewhat limited and maintaining the shape change usually requires continued application of an external force. In the absence of a substrate, a free-standing metamaterial could be folded into the appropriate geometry after fabrication of a planar structure. Gallium is well suited for such applications, because it exhibits greater flexibility than other conventional metals. At room temperature, Ga has a homologous temperature [operating temperature (298 K) / melting temperature (303 K)] of 0.98 [32].

At such high values for the homologous temperature, Ga is very soft and the stress level required for deformation at a given strain rate is extremely small. One approach to quantifying this is to consider the hardness of a metal at room temperature. The hardness value is a measure of the yield or flow strength of the material, where the former parameter is approximately 3 times larger than the latter [33,34]. Thus, the hardness of solid Ga at room temperature is 0.085 GPa [35]. For the purposes of comparison, the homologous temperature of Au at room temperature is 0.22 and the corresponding hardness value at room temperature is in the range of 1.07 – 2.8 GPa [36].

With this in mind, we demonstrate a second technique for creating 3D metamaterials. In Figure 8.4(a), we show a free-standing Ga-based metamaterial that has been folded into the form of a "square wave." To fabricate this structure, we first created a planar SRR1 metamaterial, as shown in Figure 8.2(b), and then mechanically folded each row of array, such that it was perpendicular to the adjacent row. This approach can be extended to create a wide variety of folded geometries that maintain their shape. We show the excitation geometry in Figure 8.4(b) and corresponding transmission spectrum in Figures 8.4(c) and 8.4(d). The transmission properties of this structure can be understood by considering the two different SRR orientations separately: vertical SRRs parallel to the beam propagation direction and horizontal SRRs perpendicular to that axis. In the former configuration, adjacent vertical SRRs were alternately oriented towards and away from the incident THz radiation. Although the effective impedance is different for these two orientations, associated with the difference phase properties of the reflected field, they exhibit the same transmission resonance because the eigenmode excitation is the same [37]. For the horizontal SRRs, alternate horizontal rows are oriented in the same direction

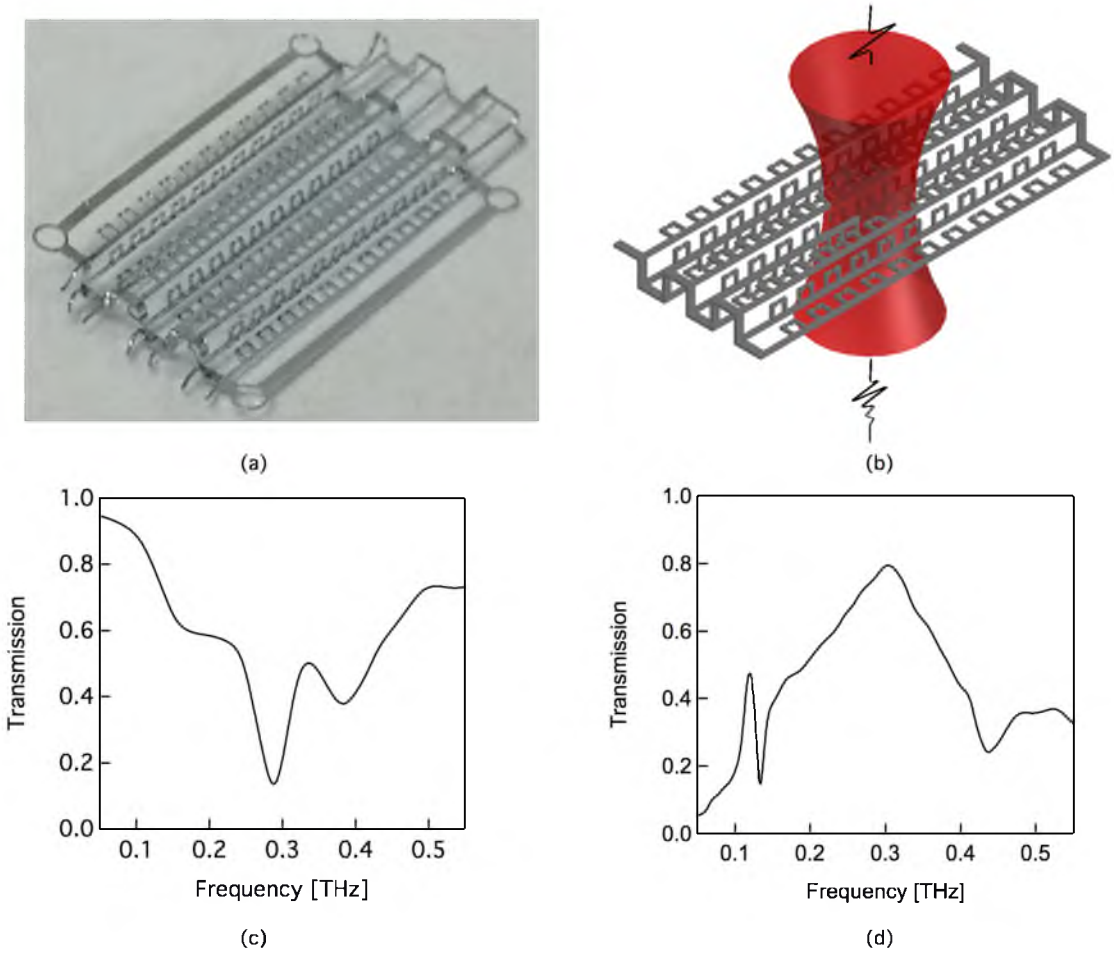

Figure 8.4. A mechanically folded 3D structure. (a) A photograph of "square-wave" 3D metamaterial with each row of SRR perpendicular to the adjacent rows. (b) Schematic diagram of square 3D metamaterial and the excitation geometry. (c) Transmission spectrum for normally incident THz radiation polarized perpendicular to the connection lines. (d) Transmission spectrum for normally incident THz radiation polarized parallel to the connection lines.

but spatially shifted relative to one another by ~740 μm. The superposition of these contributions agrees well with the observed spectra. Finally, we note that while the individual elements in SRR1 were all oriented in the same direction, we expect that a more complex resonance response can be achieved in the folded 3D structure by rotating individual elements in the planar array [37].

In the third approach, we show that 3D metamaterials can be fabricated directly via a single injection molding process with no post-processing steps. As an example of this, we show a schematic diagram of a more complex 3D structure in Figure 8.5(a). The device consists of two main pieces: two orthogonally oriented layers of a square closed ring resonator (CRR) with a bisecting line and two outwardly facing posts extending out from each surface. The square CRR had an inner width of 320 μm, outer width of 460 μm, and thickness of 50 μm, the bisecting lines were 120 μm wide and 50 μm thick, and the protruding posts were 70 μm wide on each side and extended out of the plane of the device by 50 μm. Fabrication of this device required that the SU-8 master template comprised square CRRs, bisecting lines and protruding posts (at the intersections of CRRs and bisecting lines). Each PDMS layer in the peelable mold had the same microchannel geometry, with one rotated by 90° relative to the other. Peeling away the PDMS films yielded a free-standing structure that has the appearance of having four layers, though a single injection injection/solidification step was used. This approach can be extended to create a wide variety of other 3D architectures. In Figure 8.5(b), we show a photograph of the overall device, with an expanded view in Figure 8.5(c).

In Figure 8.5(d), we show the transmission spectrum for normally incident THz wave polarized parallel to one of the bisecting lines. Over the measured frequency range,

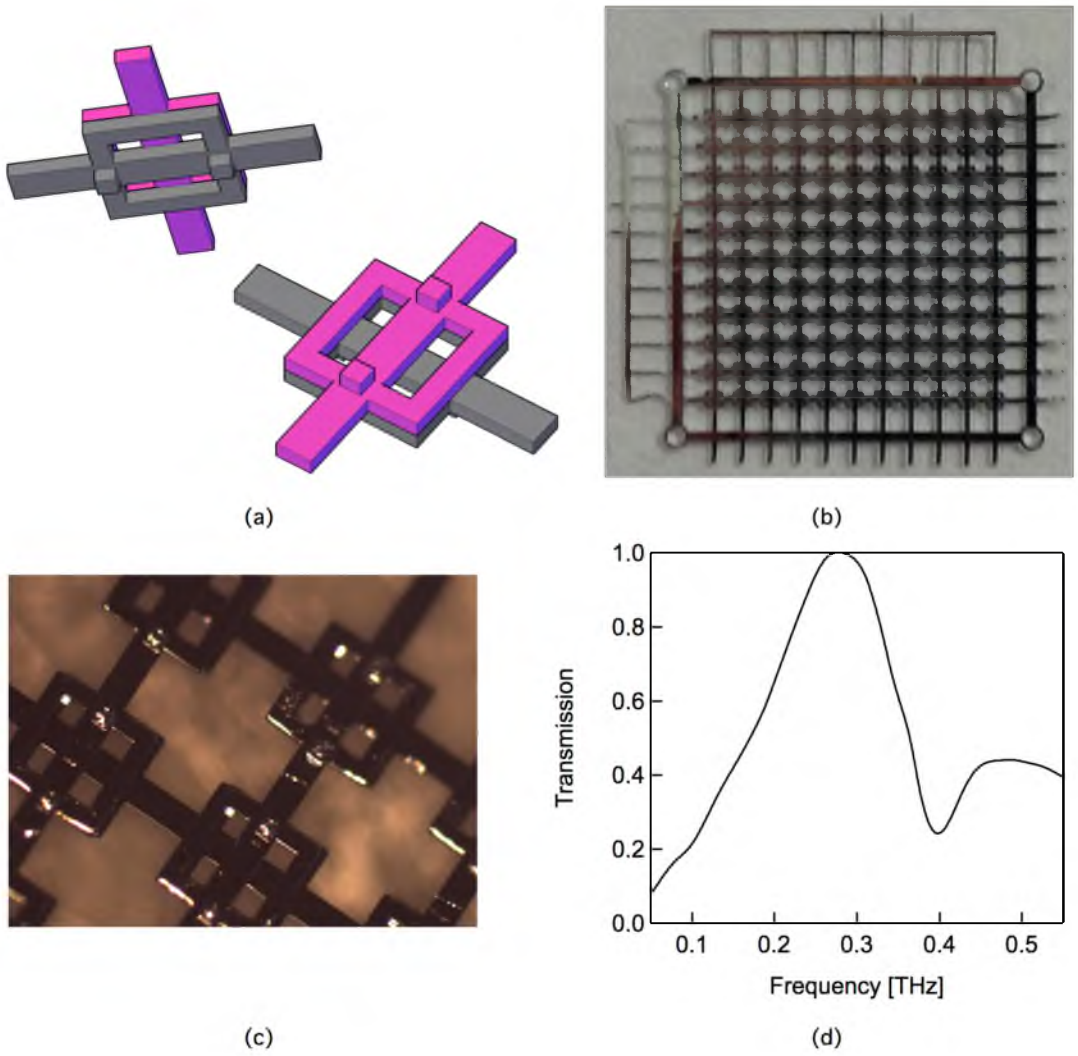

Figure 8.5. 3D structure fabricated without post-processing steps. (a) Schematic diagram of one unit of the complex 3D metamaterial for two different viewing angles. (b) Photograph of corresponding all-metal free-standing 3D metamaterial. (c) Microscope image of a portion of the device. (d) THz transmission spectrum with normally incident THz radiation polarized parallel to one of the bisecting lines.

we only observed monotonically increasing transmission below 0.28 THz and resonance transmission resonance centered at 0.4 THz. The former feature arises from a Drude-like response associated with the long bisecting line, while the latter feature arises from a dipole resonance. The height of square pillars in this sample is limited by available thickness of SU-8 photoresist. Thus, in this polarization configuration, it does not significantly affect the measured transmission spectrum. However, it is possible to obtain structures with out-of-plane dimensions that are comparable to that of the in-plane dimensions by using other photoresist materials or methods for defining the template. Such structures would be expected to exhibit unique responses as a function of the azimuthal and polar incidence angles.

8.3 Conclusion

We have demonstrated an approach for fabricating a variety of all-metal free-standing 2D and 3D THz. The structures were constructed using a variation of injection molding, where Ga was heated above its melting temperature and injected into a peelable elastomeric molded that had embedded microchannels of the desired geometry. The liquid metal inside the mold did not solidify when cooled to room temperature or even - 16°C. However, we could rapidly solidify it at room temperature by contacting it with solid gallium. This solidification mechanism suggests that it may be possible to control physical state of individual sections, by creating appropriate gaps in the liquid metal lines. Using this approach, we demonstrated the ability to easily create a variety of 2D and 3D metamaterials. Importantly, the range of potential geometries is not limited to conventional single layer or stacked multilayer devices. Thus, in addition to these two

embodiments, we also demonstrated folded geometries and arrays of complex 3D elements. Given the flexible nature of the fabrication approach, there is a broad range of architectures for both the individual unit cell and the overall structure that can be realized and that cannot be easily made using other techniques. Since there is no substrate, metal lines are needed to connect individual elements. Careful design of the geometry of these connection lines may be needed to minimize the impact on the resulting spectrum.

8.4 Experimental Section

For fabrication of template, we coated a silicon wafer with SU-8 3010 photoresist and spun it at 5000 rpm for 30 seconds. This film was exposed to UV light using a blank mask to form a flat layer, which was used to improve the adhesion between the silicon wafer and the upper SU-8 patterned layer. For the planar 2D SRR metamaterial template, a second layer of SU-8 2025 photoresist was then spun cast at 1000 rpm. UV lithography using a mask with the appropriate metamaterial pattern yielded a thin 80 μm upper photoresist layer with the designed pattern. This served as the template for the PDMS structure that was fabricated via soft lithography. For the non-planar 3D metamaterial template, discussed in Figure 8.5, a second layer of SU-8 2025 photoresist was spun at 1700 rpm above the first layer of SU-8 3010 photoresist. After baking, it was exposed to UV light using a mask with the CRR and bisecting line pattern. Then a third layer of SU-8 2025 photoresist was spun at 1700 rpm. After baking, it was exposed to UV light using an aligned mask with the post pattern to form a third layer. Both the second layer and third layers had a thickness of 50 μm. Both photoresist layers were then simultaneously developed to obtain the final two-layer pattern on a single

PDMS film.

For soft lithography, a PDMS pre-polymer was mixed with a curing agent using a volume ratio of 7:1, degassed, poured onto the SU-8 template and cured for 2 hours at 60 °C. After curing, the inverse PDMS replicas were peeled off and reversibly bonded with another layer of PDMS through van der Waals forces, yielding the desired microfluidic channel-based device.

For characterization of transmission properties, we used THz time-domain spectroscopy to measure the absolute transmission spectra, $t(\nu)$, of the electric field through the device, where ν is the THz frequency [38]. The sample was mounted on a metal frame in which the opening size exposed only the metamaterial array. Photoconductive devices were used for both emission and coherent detection. An off-axis paraboloidal mirror was used to collect and collimate the THz radiation from the emitter to the device. The THz beam was normally incident on the surface of metamaterial sample. The magnitude of the amplitude transmission coefficient, $t(\nu)$, is determined by

$$t(\nu) = |t(\nu)| \exp[i\varphi(\nu)] = \frac{E_{sample}(\nu)}{E_{reference}(\nu)}. \tag{8.1}$$

In this expression, E_{sample} and $E_{reference}$ are the measured THz electric fields with either the sample or reference (no sample) in the beam path, respectively, and $|t(\nu)|$ and $\varphi(\nu)$ are the magnitude and phase of the amplitude transmission coefficient, respectively. The reference spectrum was taken with no sample in the beam path, allowing for measurement of the absolute transmission spectrum.

8.5 References

1. R. A. Shelby, D. R. Smith, S. C. Nemat-Nasser, and S. Schultz, "Microwave transmission through a two-dimensional, isotropic, left-handed metamaterial," Appl. Phys. Lett. **78**, 489 (2001).

2. W. J. Padilla, "Group theoretical description of artificial electromagnetic metamaterials," Opt. Express, **15**, 1639–1646 (2007).

3. H. T. Chen, J. F. O'Hara, A. J. Taylor, R. D. Averitt, C. Highstrete, M. Lee, and W. J. Padilla, "Complementary planar terahertz metamaterials," Opt. Express **15**, 1084–1095 (2007).

4. D. A. Powell, and Y. S. Kivshar, "Substrate-induced bianisotropy in metamaterials," Appl. Phys. Lett. **97**, 091106 (2010).

5. K. Fan, A. C. Strikwerda, H. Tao, X. Zhang, and R. D. Averitt, "Stand-up magnetic metamaterials at terahertz frequencies," Opt. Express **19**, 12619–12627 (2011).

6. C. M. Soukoulis, and M. Wegener, "Past achievements and future challenges in the development of three-dimensional photonic metamaterials," Nature Photon. **5**, 523–530 (2011).

7. W.-C. Chen, A. Totachawattana, K. Fan, J. L. Ponsetto, A. C. Strikwerda, X. Zhang, R. D. Averitt, and W. J. Padilla, "Single-layer terahertz metamaterials with bulk optical constants," Phys. Rev. B **85**, 035112 (2012).

8. N. Katsarakis, G. Konstantinidis, A. Kostopoulos, R. S. Penciu, T. F. Gundogdu, M. Kafesaki, E. N. Economou, Th. Koschny, and C. M. Soukoulis, "Magnetic response of split-ring resonators in the far-infrared frequency regime," Opt. Lett. **30**, 1348–1350 (2005).

9. N. R. Han, Z. C. Chen, C. S. Lim, B. Ng, and M. H. Hong, "Broadband multi-layer terahertz metamaterials fabrication and characterization on flexible substrates," Opt. Express **19**, 6990–6998 (2011).

10. F. Miyamaru, S. Kuboda, K. Taima, K. Takano, M. Hangyo, and M. W. Takeda, "Three-dimensional bulk metamaterials operating in the terahertz range," Appl. Phys. Lett. **96**, 081105 (2010).

11. H. O. Moser, and C. Rockstuhl, "3D THz metamaterials from micro/nanomanufacturing," Laser & Photon. Rev. **6**, 219–244 (2012).

12. D. Grischkowsky, S. Keiding, M. Van Exter, and C. Fattinger, "Far-infrared time-domain spectroscopy with terahertz beams of dielectrics and semiconductors," J. Opt. Soc. Am. B **7**, 2006–2015 (1990).

13. Y.-S. Jin, G.-J. Kim, and S.-G. Jeon, "Terahertz dielectric properties of polymers," J. Kor. Phys. Soc. **49**, 513–517 (2006).

14. R. A. Shelby, D. R. Smith, and S. Schultz, "Experimental verification of a negative index of refraction," Science **292**, 77–79 (2001).

15. H. O. Moser, J. A. Kong, L. K. Jian, H. S. Chen, G. Liu, M. Bahou, S. M. P. Kalaiselvi, S. M. Maniam, X. X. Cheng, B. I. Wu, P. D. Gu, A. Chen, S. P. Heussler, S. bin Mahmood, and L. Wen, "Free-standing THz electromagnetic metamaterials," Opt. Express **16**, 13773–13780 (2008).

16. H. O. Moser, L. K. Jian, H. S. Chen, M. Bahou, S. M. P. Kalaiselvi, S. Virasawmy, S. M. Maniam, X. X. Cheng, S. P. Heussler, S. bin Mahmood, and B.-I. Wu, "All-metal self-supported THz metamaterial – the meta-foil," Opt. Express **17**, 23914–23919 (2009).

17. K. Fan, A. C. Strikwerda, H. Tao, X. Zhang, and R. D. Averitt, "Stand-up magnetic metamaterials at terahertz frequencies," Opt. Express **19**, 12619–12627 (2011).

18. J. C. MacDonald, D. C. Duffy, J. R. Anderson, D. T. Chiu, H. Wu, O. J. A. Schueller, and G. M. Whitesides, "Fabrication of microfluidic systems in poly (dimethylsiloxane)," Electrophoresis **21,** 27–40 (2000).

19. R. W. Powell, "The electrical resistivity of gallium and some other anisotropic properties of this metal," Roc. R. Soc. London, Ser. A **209**, 525–541 (1951).

20. J. R. Gordon, and R. A. Serway, *Principles of Physics* (Saunders College Pub., 1993).

21. J. Wang, S. Liu, Z. V. Vardeny, and A. Nahata, "Liquid metal-based plasmonics," Opt. Express **20**, 2346–2353 (2012).

22. V. P. Skripov, *Metastable Liquids: Transl. from Russ. by R. Kondor. Transl. Ed. by D. Slutzkin* (Wiley, 1974).

23. E. V. Charnaya, C. Tien, W. Wang, M. K. Lee, D. Michel, D. Yaskov, S. Y. Sun, and Y. A. Kumzerov, "Atomic mobility in liquid gallium under nanoconfinement," Phys. Rev. B **72**, 035406 (2005).

24. D. A. Porter, K. E. Easterling, and M.Y. Sherif, *Phase Transformations in Metals and Alloys* (CRC Press, 2009).

25. W. J. Padilla, A. J. Taylor, C. Highstrete, M. Lee, and R. D. Averitt, "Dynamical electric and magnetic metamaterial response at terahertz frequencies," Phys. Rev. Lett. **96**, 107401 (2006).

26. H. T. Chen, W. J. Padilla, J. M. O. Zide, A. C. Gossard, A. J. Taylor, and R. D. Averitt, "Active terahertz metamaterial devices," Nature **444**, 597–600 (2006).

27. K. Aydin, K. Guven, N. Katsarakis, C. Soukoulis, and E. Ozbay, "Effect of disorder on magnetic resonance band gap of split-ring resonator structures," Opt. Express **12**, 5896–5901 (2004).

28. N. R. Han, Z. C. Chen, C. S. Lim, B. Ng, and M. H. Hong, "Broadband multi-layer terahertz metamaterials fabrication and characterization on flexible substrates," Opt. Express **19**, 6990–6998 (2011).

29. J. Wang, S. Liu, S. Guruswamy, and A. Nahata, "Reconfigurable liquid metal based terahertz metamaterials via selective erasure and refilling to the unit cell level," Appl. Phys. Lett. **103**, 221116 (2013).

30. J. Wang, S. Liu, S. Guruswamy, and A. Nahata, "Reconfigurable terahertz metamaterial device with pressure memory," Opt. Express **22**, 4065–4074 (2014).

31. H. Tao, A. C. Strikwerda, K. Fan, C. M. Bingham, W. J. Padilla, X. Zhang, and R. D. Averitt, "Terahertz metamaterials on free-standing highly-flexible polyimide substrates," J. Phys. D: Appl. Phys. **41**, 232004 (2008).

32. H.J. Frost, and M.F. Ashby, *Deformation-Mechanism Maps: The Plasticity and Creep of Metals and Ceramics* (Pergamon Press, 1982).

33. F. A. McClintock, and A. S. Argon, *Mechanical Behavior of Materials* (Addison-Wesley, 1966).

34. K. Herrmann, *Hardness Testing: Principles and Applications* (ASM International, 2011).

35. D. S. Lin, and H. Wilman, "The surface structure of gallium after plastic deformation by unidirectional abrasion and by rolling," J. Phys. D: Appl. Phys. **5**, 2068 (1972).

36. M. Dietiker, R. D. Nyilas, C. Solenthaler, and R. Spolenak, "Nanoindentation of single-crystalline gold thin films: Correlating hardness and the onset of plasticity," Acta Mater. **56**, 3887–3899 (2008).

37. C. Rockstuhl, T. Zentgraf, E. Pshenay-Severin, J. Petschulat, A. Chipouline, J. Kuhl, T. Pertsch, H. Giessen, and F. Lederer, "The origin of magnetic polarizability in metamaterials at optical frequencies – an electrodynamic approach," Opt. Express **15**, 8871–8883 (2007).

38. D. Grischkowsky, S. Keiding, M. v. Exter, and C. Fattinger, "Far-infrared time-domain spectroscopy with terahertz beams of dielectrics and semiconductors," J. Opt. Soc. Am. B **7**, 2006 (1990).

CHAPTER 9

3D PRINTING OF RECYCLABLE SOLID METAL STRUCTURES

9.1 Introduction

The ability to fabricate three-dimensional (3D) structures is a topic of great interest in a broad range of areas, including metamaterials [1-3], microvascular networks [4-6], tissue engineering [7] and electronics [8,9]. Among the various fabrication methods that have been developed for such applications, 3D printing has been shown to be a very attractive approach, since it allows for the creation of complex geometries that may be difficult to fabricate using other means [10]. The most commonly used materials for this approach includes thermoplastic polymers, metals and ceramics [11], where the deposition often occurs via an additive manufacturing method. While such techniques reduce waste in the printing process compared to top-down fabrication methods, the print materials typically have relatively high melting temperatures or become crosslinked and, therefore, are not easily recyclable. Here, we demonstrate that gallium metal is a good candidate for 3D printing. The process operates at temperatures that are relatively close to room temperature and relies on pull of a continuous filament of liquid gallium that quickly solidifies when it comes in contact with solid gallium, creating structures that can be handled in the same manner as other 3D printed objects. In the absence of this contact

with solid gallium, the extruded liquid gallium often does not solidify, even when cooled well below the freezing temperature of the metal [3]. The diameter of the extruded component can be carefully controlled by varying the print speed and can have a minimum diameter that is smaller than the print nozzle opening. Since gallium has a melting temperature of ~30 °C, the printed structures can be easily recycled (i.e., returned to the liquid metal state) with only modest heating. This may prove useful for applications where multiple variations of a design need to be characterized experimentally before settling on a final design. In such cases, the amount of waste material can be minimized significantly or eliminated altogether.

9.2 Results and Discussion

We constructed a homemade 3D printing system, shown in Figure 9.1, that consists of three main components: a syringe fitted with a metal printing nozzle (commercially available metal needles attached to the syringe tip), a sample platform that is cooled using a Peltier cooler, and a 3-axis translation stage that can move the sample up to 15 mm along each axis. For the majority of the structures fabricated, we used either 20 gauge or 27 gauge needles with flat end faces. The inner diameters of these needles were ~600 μm and 210 μm, respectively. Since gallium has a melting temperature that is above room temperature, the syringe was surrounded by a heating pad that was set to 38°C to ensure that the metal within the syringe and the printing nozzle was completely melted. The substrate sat on a flat aluminum platform that was in good thermal contact with a Peltier cooler. The cooled platform ensured that once the metal was in contact with the substrate, its temperature fell below the melting temperature, so that it could solidify

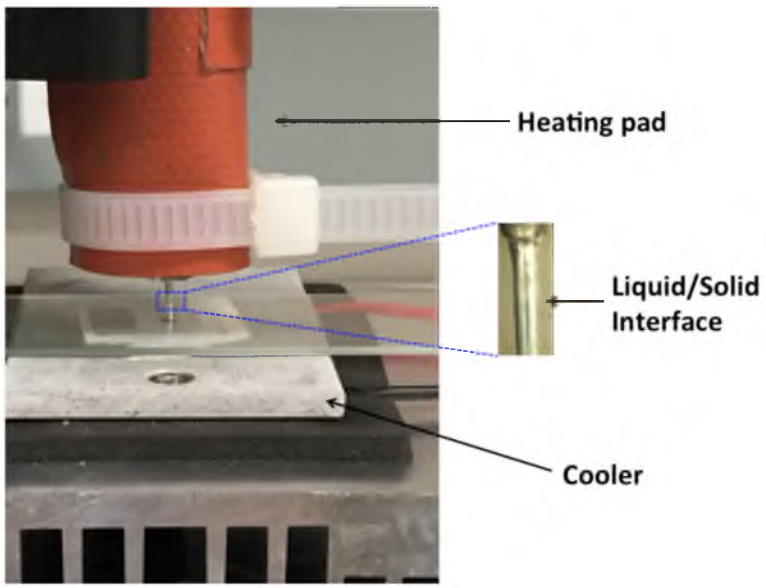

Figure 9.1. Photograph of the experimental setup for 3D printing gallium with an expanded microscope view of the liquid/solid interface. The syringe body is surrounded by a heating pad with a temperature sensor and mounted in a syringe pump. The glass substrate is placed on the top of an aluminum platform that is cooled using a Peltier cooler. This assembly is mounted on a 3-axis stage. The expanded view of the liquid/solid interface of the drawn gallium is shown to the right of the main figure.

quickly.

In preparation for printing, we found that it was difficult to make liquid gallium adhere to a clean microscope glass slide, if the liquid gallium from the syringe was brought in direct contact with the substrate and subsequently cooled. This occurred despite the fact that liquid gallium is known to wet a variety of materials, including glass substrates. To circumvent this issue, we needed to first deposit a small drop of liquid gallium on the glass slide, spread it using a pair of tweezers and then solidify the resulting thin film by bringing it into contact it with a piece of solid gallium. The reason why this spreading approach works is that when the liquid metal is spread across the glass surface, the unoxidized liquid metal that breaks through the initial oxide layer of the gallium drop quickly re-oxidizes, which in turn allows the liquid metal to wet it [12]. To

ensure that this thin film is solidified, we bring it into contact with a piece of solid gallium, which then can act as a seed layer for any subsequently deposited liquid metal. It is worth noting that if the thin film (seed layer) is not solidified, the succeeding liquid gallium that is printed will not necessarily solidify, even when cooled well below its freezing point [3].

The basic steps in the printing process are illustrated in Figure 9.2. In order to begin the process for the first time, liquid gallium needs to be extruded first through the print nozzle. However, when sufficient pressure is applied to the syringe, a pendant drop of gallium forms just outside the nozzle. To remove this drop, it is brought into contact with a glass slide that has a solid gallium thin film. Once contact is made, the substrate is pulled away from the syringe, causing a break that takes away the excess pendant gallium and leaves behind a protruding cone shaped structure on the print nozzle. The shape of this protrusion arises from the fast oxidation of gallium at the break point [13]. This glass

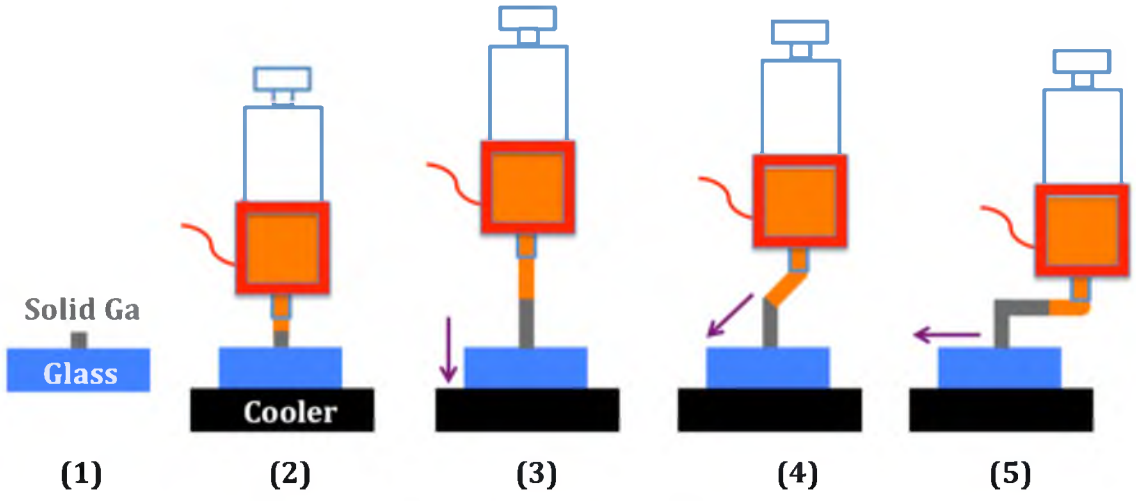

Figure 9.2. Schematic diagram of the process flow for 3D printing gallium structures. The orange extruded section corresponds to liquid gallium that quickly solidifies (change in color to gray). The dark orange box corresponds to a heater pad that surrounds the liquid metal filled syringe. See text for details regarding the setup and printing process.

slide can be discarded.

In order to print a structure, we bring the gallium protruding from the print nozzle into contact with a new substrate. Here the contact can be with a thin solid gallium (seed) film or with gallium that has already been printed and solidified. It is worth noting that the metal on the substrate and at the print nozzle are oxidized, which can hamper adhesion between the two when the temperature of substrate is too low. Too low temperature makes the metal on the substrate not melted but the metal at the print nozzle solidified quickly so that they are solid-solid contact. To make a firm contact, the protruding gallium needs to melt the solid gallium partially and then re-solidify.

In contrast to conventional 3D printing, where the melted filament is pushed through the printer nozzle, the solid gallium at the solid/liquid interface pulls the liquid gallium out of the needle, so it is typically not necessary to apply any pressure on the syringe. As with many other liquid metals [14], it is possible to create a uniform column of (liquid) gallium because the outer surface quickly oxidizes, thereby stabilizing the shape. However, in contrast to other work in this area, the metal solidifies quickly creating a solid metal structure. By controlling the position and speed with which the solid/liquid interface moves, we are able to obtain a variety of different 3D structures. After the fabrication of each segment is completed, the stage is very rapidly moved, causing a break at the solid/liquid gallium interface, so that printing can be continued at another position.

We now describe a number of different example geometries that show the potential of this approach. As noted above, the diameter of the printed metal is dependent on the stage moving speed, where the maximum diameter is limited by the output diameter of the

print nozzle. In Figure 9.3(a), we show a straight extruded metal segment that has a constant diameter. Using a 27-gauge needle with an inner diameter of 210 μm as the print nozzle, straight segments that were pulled at a uniform rate had a constant diameter of ~200 μm. By varying the pull speed, it is possible to continuously vary the extruded wire diameter, as shown in Figure 9.3(b). In situations where a varying diameter is desirable, there are restrictions on the rate at which liquid gallium can be pulled out of the syringe associated with the rate at which the metal solidifies (i.e., the rate at which the solid/liquid interface moves).

The rate at which a structure can be printed is ultimately related to the speed with which the print medium can be solidified in the appropriate position. In the present approach, this is determined by the rate at which the solid-liquid interface moves. In general, this is a complex process that is related to undercooling, nucleation, and heat transfer. While these microscopic processes are important to understand, from the point of view of developing a printing process, we measured the rate at which a uniform extruded metal segment could be pulled from the syringe and solidified. To accomplish this, we used three different print nozzles (20, 23 and 27 gauge needles) and made measurements of solidification speeds for 10 independent 1.6 mm long metal segments to determine the print speed, as shown in Figure 9.4. As might be expected, the solidification speed is greater for narrower diameter metal segments, which can be attributed to the faster cooling rate. The relatively large error bars are likely the result of open loop heating on the syringe and open loop cooling on the sample platform, which can result in fluctuations in the respective temperatures. We expect that feedback in both systems will reduce the variability in the print speeds.

(a) (b)

Figure 9.3. Straight lines. (a) Microscopic image of a straight solid metal segment with constant diameter. (b) Microscopic image of a straight solid gallium segment with a controllable varying diameter. In both cases, a 27-gauge needle was used as the print nozzle.

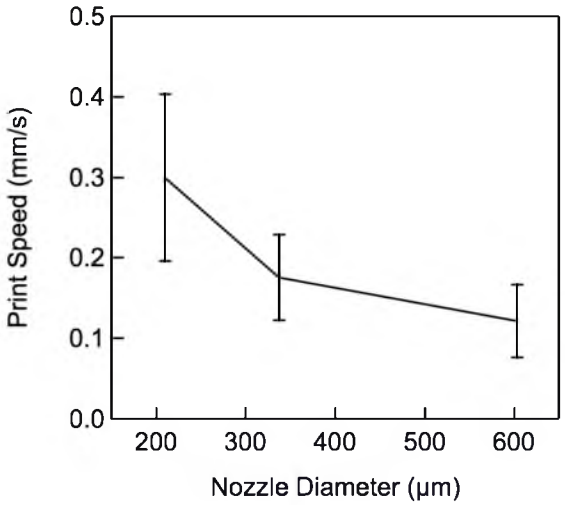

Figure 9.4. Measurement of the rate that a continuous gallium filament can be solidified as a function of the print nozzle diameter. Ten segments were printed with each needle.

We can also create sharp bends in the printed structure, as illustrated in Figure 9.5, without requiring any discontinuity in the extrusion process. In Figure 9.5(a), we show two structures that include 90° right angle bends. In order to create such bends, as shown in Figure 9.2, the sample stage cannot immediately move horizontally, but rather requires that the pull direction rotate quickly from vertical to horizontal. As the liquid gallium is pulled along the horizontal direction, the metal surface oxidizes quickly and solidifies allowing it to maintain its shape. It is worth noting that as the sample platform moves horizontally, there is a possibility for breaks to occur in the filament near the needle. The situation arises because the liquid gallium exits the print nozzle vertically, while the stage is moving horizontally. This is particularly an issue when long horizontal sections are printed. To eliminate such occurrences, we apply mild pressure to the syringe to force liquid metal move out of the needle. By monitoring the movement of the solid/liquid interface, we are able fabricate a solid line of any desired length.

In conventional 3D printing, parts are built layer-by-layer using plastics, such as ABS (acrylonitrile butadiene styrene), and each layer of a horizontal section usually requires

(a) (b)

Figure 9.5. Bending structures. (a) Photograph of two extruded solid gallium metal lines with a 90° bend fabricated on a glass slide following the procedure shown in Figure 9.2. (b) The same structures in (a) trimmed using mildly heated tweezers. A 20-gauge needle was used as the print nozzle.

some underlying support. Without this, the maximum length of an unsupported horizontal section is rather limited and can begin to droop. In contrast, the printing approach described here allows for continuous extrusion of gallium. For the geometry shown in Figure 9.5, the horizontal line can be modeled as a cantilever with uniform applied pressure. If we assume that the vertical section is fixed, the maximum length of the horizontal (cantilever) section is given by [15]

$$L = \left(\frac{2Er^2y}{\rho g} \right)^{1/4} \tag{9.1}$$

where L and r are the length and radius of the horizontal (cantilever) section, respectively, y is the deflection of the cantilever, E is Young's modulus for gallium (9.81 GPa), ρ is the density of solid gallium (5.91 g/cm^3) and g is the acceleration due to gravity. If we assume a deflection of 1 mm with an extruded segment radius of 300 μm (20 gauge print nozzle), the maximum cantilever length is 7.4 cm. Thus, this approach can be used to create geometries that incorporate unsupported segments that are not possible using other 3D printing techniques.

Another significant advantage of using gallium as the 3D printing medium is that the structure can be trimmed after printing without using chemicals or high energy heating. To demonstrate this, we heated the tip of a pair of tweezers to 60 °C and brought them into contact with the relevant portion of the gallium structure. This immediately melts the affected gallium metal, shortening the horizontal lines, as shown in Figure 9.5(b). This process can be used to make both minor and major changes in the printed structure

geometry.

More complex structures involving multiple bends or curves can also be fabricated easily, as shown in Figure 9.6. For metal sections that are printed relatively close to the glass substrate, the solidification rate is relatively constant. However, as the liquid-solid interface moves away from the substrate, the solidification rate slows down. Thus, changes in the operating temperature are needed to keep the solidification rate constant. In our case, this was accomplished by reducing the syringe heating pad temperature as the substrate moved away from the print nozzle.

In Figure 9.6(a), we show a multilevel structure that incorporates a number of right angle bends. Based on the calculation associated with Equation 9.1, such structures can extend for quite some distance above the substrate. In Figure 9.6(b), we show fabricated a similar structure; here it incorporates both right angle and curved bends. In Figure 9.6(c), we show a curved structure that was printed in one continuous process and contacted the

(a) (b) (c)

Figure 9.6. Three-dimensional structures that include right angle and curved bends. (a) A multilevel structure that includes seven right angle bends. (b) A square spiral structure. (c) A curved structure that contacts the substrate at six different points.

substrate at six different points. In order to print this structure, we needed to first deposit six gallium seed layers on the glass substrate. As with conventional 3D printing, rather complex geometries can be created through appropriate computer control of the translation stages.

In all of the structures discussed until now, the printed structures were fabricated in a continuous process. In Figure 9.7, we describe several structures in which intentional breaks in the structure were created to allow for the fabrication of multiple segments to be drawn out of a single point. As an example, in Figure 9.7(a), we print a variety of y-structures, by first creating a single filament that is bent and then returning to the joint and drawing an additional filament at a different angle. In order to ensure that the second arm of the y-structure was firmly connected to the existing structure, the point where the joint occurred was partially re-melted with the liquid gallium from the print nozzle by

(a) (b) (c)

Figure 9.7. Structures made with multiple segments. (a) An array of y-structures surrounding a four-prong fork structure. (b) A structure that has two patterns, which are orthogonally oriented with respect to one another. (c) Schematic drawing of the structure in (b) that is color coded by print order (red first, yellow second, cyan third, dark blue fourth, and magenta last).

turning off the cooler. The entire structure solidified as an integrated structure once the substrate was cooled. Using this process, we printed a structure that contained four branches (center of Figure 9.7(a)). More complex geometries, such as that shown in the image in Figure 9.7(b) and schematically in Figure 9.7(c), can be printed straightforwardly.

9.3 Conclusion

In summary, we have demonstrated an approach for 3D printing solid of metal structures using gallium metal. The printing process operates at temperatures close to room temperature, since the melting temperature of gallium is 30°C. Solidification of the metal once it has been extruded relies on cooling it below the melting temperature of gallium and having it be in contact with solid gallium. The latter requirement corresponds to a moving liquid-solid interface. It is this interface that draws the liquid metal out of the syringe and through the print nozzle. We use commercially available needles as the print nozzles, which extrude the metal in a cylindrical shape. Print nozzles with other geometries should work equally well. An attractive feature of the process lies in the fact that the printed structures can be easily melted and reused almost indefinitely, which severely reduces the amount of waste material. Finally, the diameter of the extruded filaments was typically on the order of the print nozzle diameter. We expect that with further refinement, much thinner diameter segments can be extruded, allowing for the fabrication of smaller structures, such as devices relevant for electromagnetic studies, including terahertz plasmonics and metamaterials.

9.4 References

1. C. M. Soukoulis, and M. Wegener, "Past achievements and future challenges in the development of three-dimensional photonic metamaterials," Nature Photon. **5**, 523–530 (2011).

2. K. Fan, A. C. Strikwerda, H. Tao, X. Zhang, and R. D. Averitt, "Stand-up magnetic metamaterials at terahertz frequencies," Opt. Express **19**, 12619–12627 (2011).

3. J. Wang, S. Liu, S. Guruswamy, and A. Nahata, "Injection molding of free-standing, three-dimensional, all-metal terahertz metamaterials," Adv. Opt. Mater. **2**, 663–669 (2014).

4. D. Therriault, S. R. White, and J. A. Lewis, "Chaotic mixing in three-dimensional microvascular networks fabricated by direct-write assembly," Nature Mater. **2**, 265–271 (2003).

5. A. P. Esser-Kahn , P. R. Thakre, H. Dong, J. F. Patrick, V. K. Vlasko-Vlasov, N. R. Sottos, J. S. Moore, and S. R. White, "Three-dimensional microvascular fiber-reinforced composites," Adv. Mater. **23**, 3654–3658 (2011).

6. W. Wu, A. DeConinck, and J. A. Lewis, "Omnidirectional printing of 3D microvascular," Adv. Mater. **23**, H178–H183 (2011).

7. J. N. H. Shepherd , S. T. Parker, R. F. Shepherd, M. U. Gillette, J. A. Lewis, and R. G. Nuzzo, "3D microperiodic hydrogel scaffolds for robust neuronal cultures," Adv. Funct. Mater. **21**, 47–54 (2011).

8. J. Hu, and M.-F. Yu, "Meniscus-confined three-dimensional electrodeposition for direct writing of wire bonds," Science **329**, 313–316 (2010).

9. B. Y. Ahn, E. B. Duoss, M. J. Motala, X. Guo, S.-I. Park, Y. Xiong, J. Yoon, R. G. Nuzzo, J. A. Rogers, and J. A. Lewis, "Omnidirectional printing of flexible, stretchable, and spanning silver microelectrodes," Science **323**, 1590–1593 (2009).

10. J. A. Lewis, "Direct ink writing of 3D functional materrials," Adv. Funct. Mater. **16**, 2193–2204 (2006).

11. B. Utela, D. Storti, R. Anderson, and M. Ganter, "A review of process development steps for new material systems in three dimensional printing (3DP)," J. Manufact. Processes **10**, 96–104 (2008).

12. T. Liu, P. Sen, and C.-J. Kim, "Characterization of nontoxic liquid-metal alloy galinstan for applications in microdevices," J. Microelectromech. Syst. **21**, 443–450 (2012).

13. R. C. Chiechi, E. A. Weiss, M. D. Dickey, and G. M. Whitesides, "Eutectic gallium–indium (EGaIn): a moldable liquid metal for electrical characterization of self-assembled monolayers," Angew. Chem. **120,** 148–150 (2008).

14. C. Ladd, J.-H. So, J. Muth, and M. D. Dickey, "3D printing of free standing liquid metal microstructures," Adv. Mater. **25**, 5081–5085 (2013).

15. J. M. Gere, and B. J. Goodno, *Mechanics of Materials* (Cengage Learning, 2012**)**.

CHAPTER 10

FUTURE WORK AND CONCLUSION

10.1 Future Work

Based on results shown in previous chapters, there are some possible extensions for future work to make liquid metal-based metamaterial devices more flexible and interesting.

10.1.1 Integration of Split Ring Resonator and Hole Arrays Structure

In previous chapters, we demonstrated active control of plasmonic and metamaterial devices. For plasmonic hole arrays structures, we can tune the extraordinary transmission resonance, which is a resonant peak on near-to-zero transmission background. For metamaterial devices, we can tune the absorption resonance, which is a resonant dip on near-to-one transmission background. These two different resonance properties can be combined together through a two-layer structure. By designing proper dimensions of unit cells, we can make the resonance peak from hole arrays structure and the resonance dip from split ring resonators close or overlap with each other. This will make the total transmission be zero when THz radiation is incident normally to the surface of the device, and can be potentially used as a THz absorber. The properties of two layers can be controlled separately or simultaneously to change the transmission properties of the

device. For example, since the resonance frequency of plasmonic hole arrays structure can be shifted using external stretching, we can make this resonance frequency separate from absorption resonance of SRR so that new resonance can show up from the zero transmission spectrum background. This study will contribute a device with more flexible transmission properties.

10.1.2 Integration of MEMS and Liquid Metal Metamaterials

We demonstrated that liquid metal alloy could be used for reconfigurable terahertz plasmonic and metamaterial devices. The liquid phase of eutectic gallium-indium (EGaIn) at room temperature makes it micromoldable under different conditions. Properties of metamaterials are mainly determined by the geometry of metallic structures. The spectral response changes according to its configuration. Meanwhile, micro machining is a well-developed technology for fabricating devices with the feature size from 10 micrometers to a millimeter, which matches well with THz wavelength. By now, we have remained on concept-level demonstration for most liquid metal-based devices and operated them manually. This severely limited reconfigurable speed. In the future work, we will integrate Micro-Electro-Mechanical-Systems (MEMS) technique and non-toxic liquid metals into metamaterial devices. A micro actuator is usually controlled by external stimulus such as electric voltage, pressure or thermal energy, and can easily work at frequency larger than 1000 Hz. The movement of actuators' film can change the shapes of underlying liquid metals and the devices' configuration parameters. As a configuration changes, the spectral response will change correspondingly. By use of MEMS technology, it will be possible to largely improve the operation speed of liquid

metal-based metamaterial devices.

10.1.3 Photo-chemically Controlled Reconfigurable Metamaterials

We demonstrated reconfigurable THz metamaterials using chemical acid vapor or electrolysis. We were able to erase several rings simultaneously via localized HCl acid vapor. By using electrochemical process, we opened metamaterial ring structures to some extent by controlling applied voltage. All of these changes could lead to active control of metamaterial properties. However, for a single ring configuration, all of the opening split gaps started from a top central point and then spread from there. This limited available split ring geometries. In the future, we will develop some photochemical methods to induce local acid environment via an incident light. The purpose of this study is to open gaps of close rings at random locations. The induced acid will dissolve surface oxide layer of liquid metal to make it retract to the place where there is no acid. Because the incident light can be focused into several micrometers and directed to any location around the whole ring, we will be able to erase the liquid metal rings at arbitrary spots to make random opening for the split ring structures. This will provide us more flexible metamaterial structures, not just periodic split rings.

10.1.4 Advanced Manufacturing Methods for 3D Metamaterials

We demonstrated a technique of fabricating free-standing all-metal 3D terahertz metamaterials through injection molding of gallium. This technique can provide some 3D structures, but available structures are still limited by molds. Then we demonstrated a technique of 3D printing of gallium. Fabricated 3D structures were not restricted by any

mold. However, the dimension of 3D printing of gallium was at the several-millimeters level. In the future work, we will develop this technique to reduce the dimension of minimum feature size to hundreds of micrometers, which lies at THz spectral range. This will provide us capability of creating more flexible and complex 3D structures to manipulate and control THz electromagnetic radiation. We will also study other alternative methods to fabricate flexible 3D structures. Top-down processing and additive manufacturing will be the two main research paths for this work. For example, we can locally heat a bulk gallium to make it be melted shortly at a small size. Then we can use a needle or other small tube to suck melted gallium out to leave an empty hole inside. It is possible to make a 3D lattice via a multi-axis operation by using this method.

10.2 Conclusion

In this dissertation, we presented our work on design, fabrication and characterization of liquid metal-based metamaterial devices. We briefly summarize the results from previous chapters.

In Chapter 2, we presented the general device fabrication processes for liquid metal-based structures. It mainly used soft lithography technique after fabricating appropriate solid templates. Usually, PDMS elastomer was chosen to replica a template and worked as supporting mold for liquid metals. Liquid metals filled into PDMS microchannels and provided various structures. For 3D printing structure, we used syringe and Peltier cooler to draw various free-standing structures. We found this method can provide very flexible structures. For the optical transmission measurement, we used THz time-domain spectroscopy to measure time-domain signal. Fourier transform of time-domain signal

provided frequency-domain data, in which we can obtain both magnitude and phase information.

In Chapter 3, we demonstrated enhanced THz transmission property of a liquid metal hole arrays. The device is a periodic array of subwavelength apertures with EGaIn injected into PDMS mold. We observed two resonances in the detection window and demonstrated the tuning capability by stretching the PDMS mold.

In Chapter 4, we demonstrated a method to create reconfigurable plasmonic devices using liquid metals. We utilized a bullseye structure with various annular PDMS channels. By injecting and withdrawing liquid metals from individual channels, we were able to change the geometry dramatically. As the geometry changes, the transmission properties of time-delayed oscillation also change. We provided a simple model to explain the transmission results for different geometries.

In Chapter 5, we demonstrated a technique to change configuration of a metamaterial device. The metamaterial device was an alternative array of close ring resonators with two sizes. The erasure was accomplished using HCl to dissolve the surface oxide layer to make EGaIn retract to a position where there was no acid exposure. The refilling of EGaIn back to microchannels recovered its initial configuration. The erasure could also be done by using a small needle to press liquid metal outside of specific area. As the geometry changed, especially when one kind of close rings were erased or refilled, the transmission resonance could be removed or recovered to achieve active control of metamaterials.

In Chapter 6, we demonstrated a means of erasing liquid metal through reducing the oxide layer by an electrochemical process involving DI water with or without the

addition of NaCl. We measured the erasure rate as a function of applied voltage and NaCl concentration. Higher voltage or higher concentration of NaCl contributed to a faster erasure rate. Then we fabricated an array of close rings with embedded gold electrodes on a glass substrate. By controlling the applied voltage, we could selectively erase one or several unit cells in a random access manner. This method can control erasure at the partial unit cell level to provide more flexibility.

In Chapter 7, we demonstrated a THz metamaterial device that was not only pressure driven, but also exhibited pressure memory. Because liquid metal flowed only when a critical pressure was exceeded, the geometrical structure changed corresponding to different pressures. As the geometry changed, transmission properties of metamaterials changed abruptly. Because the liquid metal flow conditions were not reversible, the transmission spectra recorded previous applied pressure, this could be considered as a memory. To reset liquid metal structures to initial configuration, we applied acid vapor and slight pressure to remove liquid metal from microchannels.

In Chapter 8, we demonstrated an approach for fabricating all-metal free-standing 2D and 3D THz metamaterials. The structures were obtained using injection molding of gallium into reversibly bonded PDMS microchannel films. After solidification of gallium, PDMS films were separated to yield a free-standing structure. There were three means to creating 3D structure: multilayer stacking, mechanical folding and direction injection molding. We also demonstrated a simple method to solidify super cooled gallium by contacting a solid piece of gallium into liquid gallium at room temperature.

In Chapter 9, we demonstrated a method to print 3D free-standing gallium structure by controlling the solidification process. The method involved a Peltier cooler and 3D

axis stage. Due to mechanical force from the surface oxide layer of liquid gallium, solid gallium could pull liquid gallium outside of the needle so that no pressure was required to push liquid metal outside of a syringe reservoir. This was different from common 3D printing where filament is pushed out of the nozzle. We also demonstrated that 3D printing of gallium structure could also provide smaller structure than the diameter of needle.

In Chapter 10, we discussed possible study direction for future work. Various efforts can be done to make liquid metal metamaterial more flexible to satisfy different requirements. Also, advanced manufacturing method can be combined with low melting-point gallium to obtain different 3D structures.